To the University of Wyoming:

The members of the Committee approve the dissertation of Enrico Fabiano presented on April 7, 2017.

Dr. Dimitri J. Mavriplis, Chairperson

Dr. Craig C. Douglas, External Department Member

Dr. Jonathan Naughton

Dr. Jayanarayanan Sitaraman

Dr. Giuseppe Quaranta, External Examiner, Politecnico Di Milano, Italy

APPROVED:

Dr. Carl Frick, Head, Department of Mechanical Engineering

Robert Ettema, Dean, College of Engineering and Applied Science

Fabiano, Enrico, Multidisciplinary Adjoint-based Design Optimization Techniques for Helicopter Rotors, Ph.D., Department of Mechanical Engineering, May, 2017.

Helicopter rotor design optimization is a challenging task due to the multidisciplinary nature of rotorcraft design: the helicopter operates in a highly unsteady aerodynamic environment, highly flexible, slender rotor blades highlight the importance of blade aeroelasticity, while the ever more stringent noise requirements that the helicopter must satisfy underlines the need to include aeroacoustic considerations early in the design process.

Such a large scale problem can be efficiently solved with the use of gradient-based optimization methods. In gradient based optimization, the gradient of the objective function with respect to the design variables is needed to determine a search direction. The objective function's gradient can be computed either with the finite difference approach, the tangent or forward linearization approach and the adjoint or reverse approach. The finite difference approach is easy to implement but its cost scales with the number of design variables and can be affected by the choice of the step size used in the differentiation. The tangent or forward approach computes the exact gradient vector of the objective function by exact differentiation of the computational code, however its cost still scales linearly with the number of design variables. On the other hand, the adjoint or reverse approach computes the sensitivity vector with respect to a potentially infinite number of design variables at a cost essentially independent of the design variables, making the adjoint technique the only viable approach when the number of design variables is large. Hence, it is the adjoint approach that makes gradient based optimization techniques competitive for large scale problems characterized by a large number of design parameters, such as the current helicopter design problem.

The focus of this work is the development of a high-fidelity multidisciplinary adjoint technique that encompasses the three disciplines of aerodynamics, structural mechanics and aeroacoustics for rotorcraft problems. Upon successful implementation and verification, the multidisciplinary adjoint method is applied to the problem of noise minimization of a flexible rotor in trimmed forward flight with no performance penalty. Optimization results highlight the potential of high-fidelity multidisciplinary design optimization for helicopter rotors.

MULTIDISCIPLINARY ADJOINT-BASED DESIGN OPTIMIZATION TECHNIQUES FOR HELICOPTER ROTORS

by

Enrico Fabiano

A dissertation submitted to the
University of Wyoming
in partial fulfillment of the requirements
for the degree of

DOCTOR OF PHILOSOPHY
in
MECHANICAL ENGINEERING

Laramie, Wyoming
May 2017

Faster and Higher

Contents

List of Figures

List of Tables

Acknowledgments

The list of persons that I feel I should thank is way too long to be contained in one page. I am thankful to all of you and I apologize to those that I won’t be able to mention here.

I want to dedicate this work to my parents for their constant and unconditional love: this would have never been possible without you.

I am extremely grateful to my advisor, Dimitri Mavriplis, for teaching me the fundamentals of CFD and guiding me during the past few years: he will always remain my ”boss”. I would also like to thank the other members of my committee for their support during my time at the University of Wyoming and for reading this dissertation.

All the persons that I have met in Laramie and at the ”lab” should also be mentioned here. I will single out Karthik, Asitav, Lina, Renee, Ana and Bruce, but this list is far from being complete.

Mr. Giorgio Travostino deserves special mention: he introduced me to the world of aerodynamics and CFD. Here is to many more dinners together.

Finally, I would like to acknowledge the Alfred Gessow Vertical Lift Research Center of Excellence at the University of Maryland for funding this research.

Enrico Fabiano

University of Wyoming
May 2017

Chapter 1

Introduction

Helicopter rotor optimization is a challenging task due to the multidisciplinary nature of rotorcraft design, the complex and intrinsically unsteady operating environment of the rotor and the potentially large number of design variables. Such a large-scale problem can be efficiently solved with the use of gradient-based optimization methods when the gradient of the optimization objective function is computed with the adjoint approach. Hence, the goal of the work presented in this thesis is the development of a high-fidelity multidisciplinary adjoint-based design optimization capability for helicopter rotors that encompasses the three disciplines of aerodynamics, structural mechanics and aeroacoustics.

1.1 Helicopter Design: a Multidisciplinary Design Optimization Problem

The helicopter is an aircraft that uses two or more rotating wings to generate aerodynamic forces in order to sustain controlled flight [1]. The rotors operate in a complex unsteady aerodynamic environment characterized by vortical flow structures, wakes and, possibly, shock waves, and they provide lift, propulsion and control forces to the aircraft. The aerodynamic forces are generated by the relative motion between the rotors and the surrounding air even when the translational velocity of the aircraft is zero. This provides the helicopter its most distinguished feature: the ability to perform efficient hovering and vertical flights. However, large rotor diameters are needed to achieve efficient vertical flight while high-aspect ratio blades guarantee the desired aerodynamic efficiency. Hence, the structural design requirements that the rotor must satisfy to guarantee the proper aerodynamic performance yield highly flexible blades whose aerostructural response needs to be taken into account in the rotor design process. Furthermore, the propulsive forces necessary for the helicopter to sustain translational flight are achieved by tilting the main rotor, resulting in a lift imbalance between the advancing and retreating side of the blade: the advancing side is subject to higher velocity than the retreating side as a consequence of the combined translational and rotational velocity of the rotor. This, however, generates pitching and rolling moments on the rotor that need to be counteracted with a blade cyclic pitching motion to sustain trimmed level flight [1], effectively coupling the aerodynamics and flight mechanics problem.

Finally, the ability to take off and land vertically (VTOL), and to maneuver in tightly confined spaces makes the helicopter the perfect air vehicle to operate in urban environments leading to very strict noise requirements. Hence, the aeroacoustic problem needs to be addressed early in the design process and typically requires the detailed knowledge of the flowfield surrounding the rotor and its aeroelastically deformed shape.

The tight interaction between all the disciplines involved in helicopter operations makes the helicopter design an intrinsically multidisciplinary design problem: the accurate computation of the aerodynamic loads that the rotor must sustain is necessary to determine the correct structural deformation of the blades and the blade pitch controls necessary to sustain trimmed forward flight. Once the blade shape, pitch controls and aerodynamic loads are computed, the correct acoustic signature and aerodynamic performance can finally be determined.

Furthermore, the number of parameters that the designer can change to improve the rotorcraft performance is potentially high, making the multidisciplinary design problem a large-scale design optimization problem. To solve this multidisciplinary design problem the helicopter designer can change a large number of design variables, typically consisting of airfoil shapes, structural properties and pitch control parameters, making the multidisciplinary design problem a large scale design optimization problem. This large-scale multidisciplinary problem has traditionally been tackled using lower fidelity models for each discipline involved, particularly aerodynamics and structural mechanics, linked together in so-called comprehensive analysis codes, of which CAMRAD is the perfect example [2]. Despite sacrificing accuracy, low fidelity models have seen widespread use in the past because of the limited computational power available and the quick turnaround time they offered in evaluating a significant number of design configurations. More recently, efforts have been aimed at introducing higher-fidelity models earlier in the design process, particularly for the aerodynamics. Notable examples of these efforts are the U.S. Army HELIOS computer code [3] and its french counterpart [4]. A new high-fidelity multidisciplinary design analysis and optimization tool for the design of helicopter rotors in trimmed forward flight is presented in this work. This new tool encompasses the three disciplines of aerodynamics, structural mechanics and aeroacoustics and it is applied to the redesign of the flexible HART-II rotor [5] to improve its aeroacoustic and aerodynamic performance.

1.2 Helicopter Aeroacoustics

As the importance of reducing detection distance and helicopter noise signature increases for both commercial and military applications [1, 6], rotorcraft aeroacoustics takes on a leading role in the helicopter design process. Hence, a significant portion of this work will focus on including a noise prediction capability in the multidisciplinary design optimization process. Rotorcraft aeroacoustics have been widely studied in the past [7] and are now fairly well understood. Both discrete frequencies and broadband aerodynamic noise is generated through different noise mechanisms. Discrete frequency noise is deterministic in nature and divided into different components such as thickness and loading noise, blade vortex interaction noise and high speed impulsive noise. Broadband noise is typically non-deterministic and associated with the turbulent flowfield surrounding the rotor. In this work only deterministic noise is considered.

To minimize the rotor noise signature, both passive and active noise minimiztion techniques have been investigated in the past. Common passive noise minimization techniques consist of a judicious selection of rotor blade configurations, airfoils, planform and tip shapes [6]. Active control techniques such as Higher Harmonic Control (HHC), Individual Blade Control (IBC) and active flap configurations have also been investigated [6–8]. While these methods mainly rely on expensive wind tunnel experiments and on the experience of the aircraft designer, few attempts have been made at exploiting numerical shape optimization techniques in the context of noise reduction for rotating aerodynamic surfaces: Chae et al. [9] optimized the acoustic signature of a hovering rotor targeting mainly high speed impulsive (HSI) noise, while Marinus et al. [10] performed a multiobjective, multidisciplinary optimization of transonic propeller blades targeting aerodynamic, aeroelastic and aeroacoustic performance.

From a computational point of view the acoustic problem corresponds to propagating the acoustic waves generated by the moving rotor to an observer possibly far away from the rotor itself. One obvious approach to the solution of the acoustic problem is to resolve the acoustic waves to the observer. Despite reasonable success for near and mid-field observers [11, 12], the computational cost of this approach for far-field acoustic problems is still too high even for the current generation of supercomputers. A more viable and widely employed solution to the aeroacoustic problem is the use of Lightill's acoustic analogy. This is a hybrid approach in which a nearbody aerodynamic solver provides the flow information to an integral acoustic formulation that propagates the acoustic waves to the far-field observer. In this work the acoustic analogy approach has been followed by implementing a Ffowcs-Williams Hawkings (FWH) acoustic integration procedure [13, 14] to determine the rotor's noise signature. After validation of the new FWH implementation, an adjoint sensitivity approach has been developed to perform the noise minimization of the flexible HART-II rotor in trimmed forward flight.

1.3 Optimization Techniques and Their Application to Rotorcraft Design

Numerical shape optimization techniques in conjunction with Computational Fluid Dynamics (CFD) have become a common tool in the aircraft design industry [15], and numerical shape optimization for aeroacoustic and aerodynamic performance is the focus of this work.

Numerical optimization algorithms are divided in two broad categories: global or evolutionary methods and local or gradient based methods. Evolutionary methods are easy to apply to rotorcraft design problem as they only require the value of the objective function at the design point currently evaluated and, in case of a multimodal design space, they converge to the global optimum.

However, they require a significant number of function evaluations rendering their applications to design problems involving high-fidelity, computationally-intensive models impractical. The cost of evolutionary algorithms can be reduced when these are used in conjunction with metamodeling techniques [16], e.g. response surfaces, kriging methods and neural networks. However, metamodeling techniques are not well suited for optimization problems characterized by a large number of design variables [16]. Despite these limitations, evolutionary algorithms augmented with metamodeling techniques have been used in the context of airfoil optimization [17], propeller blade optimization [10, 18] and rotorcraft design [9]. Jones et al. [17] used a genetic algorithm in conjunction with an aerodynamic low-fidelity model to perform the multidisciplinary optimization of rotor blade shapes with up to 20 design parameters. Despite the quick turn-around time of the low-fidelity aerodynamic model, the authors had to reduce the computational burden by using a Message-Passing Interface to distribute the numerous function evaluations over multiple cores. Marinus et al. [10, 18] performed high-fidelity design optimization of a propeller blade for aerodynamic, aeroelastic and aeroacoustic performance with up to 30 design variables. Finally, Chae et al. [9] performed a high-fidelity design optimization of a hovering helicopter rotor to improve its high speed impulsive noise with up to 19 design variables. Despite their success, these applications reveal the high computaional cost of evolutionary algorithm even when they are applied to small-scale design optimization problems.

While a judicious selection of the design space parameterization is fundametnal for a successful optimization [19], limiting the number of design variable can have a detrimental effect on the overall optimization process and on the success of the rotorcraft design program. Furthermore, as more and more disciplines are included in the design optimization process, the number of design variables is expected to increase, exacerbating the issues associated with evolutionary algorithms. Hence, evolutionary methods are not well suited for large-scale multidisciplinary rotorcraft design problems. Contrary to evolutionary algorithms, gradient-based optimization methods require vastly fewer function evaluations provided that an efficient method for the computation of the gradient of the optimization objective function exists. This makes gradient-based optimization algorithms the only feasible alternative for the solution of large-scale, high-fidelity multidisciplinary design optimization problems.

Gradient-based methods have been the first methods to be applied to rotorcraft problems [20, 21]. Whether in their unconstrained or constrained form, they use the gradient of the objective and of the constraints of the design problem to find a direction to the nearest saddle point of the Lagrangian function associated with the optimization problem [22]. If the cost of computing the objective function's gradient is independent of the number of design variables, the performance of gradient-based methods is relatively independent of the number of design parameters.

Different methods exist for computing the gradient of an objective function [22]. Traditionally the finite-difference method has been used as it is extremely easy to implement. It is also an expensive method as, in the best case, it requires $N+1$ function evaluations, N being the number of design parameters. Furthermore, the accuracy of the method depends on the step size used for differentiation. Exact hand-differentiation of the computer code in forward or tangent mode removes the accuracy issue associated with the step size, but its cost still scales linearly with the number of design variables. However, exact hand-differentiation in reverse or adjoint mode removes the cost issue as its computational cost is independent of the number of design variables. Adjoint sensitivity formulations are a common tool in the context of CFD-based shape optimization since they allow the computation of the sensitivities of an objective function with respect to a large number of design parameters at a cost essentially independent of the number of design variables [23–29]. Made popular by Jameson [23, 30, 31], the use of adjoint equations is now well established in the context of fixed-wing, steady-state aerodynamic shape optimization [24, 27, 28]. Mavriplis [32] demonstrated the method's feasibility for time-dependent three-dimensional problems, while implementation and application to large scale rotorcraft problems has been carried out by Nielsen et al. in the NASA FUN3D code [33,34], by Mani et al. using the current flow solver framework [35] and by Lee at al. using an unstructured Euler flow solver [36]. Extension of the adjoint method to multidisciplinary design optimization problems focused mainly on fluid-structure interaction applications in the context of both fixed and rotary wing aircrafts [37, 38]. In this work a three-dimensional unsteady adjoint optimization technique for the acoustic analogy based on the FW-H equation is developed to perform the shape optimization of a rigid and flexible helicopter rotor in forward flight.

1.4 Unique Aspects of the Current Work

The current work focuses on the development of a multidisciplinary, high-fidelity, time-dependent adjoint technique for helicopter aeroacoustic design optimization problems. First, the feasibility of the aeroacoustic optimization is demonstrated on a two-dimensional application representative of blade-vortex interaction (BVI) noise: an isentropic vortex interacts with a NACA 0012 airfoil to generate noise, which is then propagated to a farfield observer with a two-dimensional acoustic integration in the frequency domain. After developing the two-dimensional coupled aeroacoustic adjoint, gradient-based airfoil shape optimization is performed to minimize the airfoil noise signature under a lift constraint. The two-dimensional problem is then extended to the noise minimization of three-dimensional rigid and flexible rotors in forward flight to realize a multidisciplinary adjoint optimization capability that encompasses the three discipline of aerodynamics, structural mechanics and aeroacoustics.

The thesis is structured as follows: Chapter 2 presents the two-dimensional aerodynamic and acoustic solver, their coupling and their tangent and adjoint linearization. Chapter 3 describes the aerodynamics, structural mechanics and aeroacoustic solvers used for the analysis of three-dimensional flexible rotors in forward flight. After the three discplines have been coupled together, the tangent and adjoint linearization of the coupled multidisciplinary analysis problem are derived to realize the multidisciplinary unsteady adjoint capability that represents the unique aspect of the current thesis. Chapter 4 presents the application of the adjoint methods in Chapter 2 and 3 to two-dimensional and three-dimensional design optimization problems. Results for these optimization highlight the potential for multidisciplinary adjoint techniques and enable shape optimization for large-scale flexible aeroacoustic design problems. Finally, Chapter 5 draws conclusions from the current work and suggest possible future development.

Chapter 2

Two Dimensional Aeroacoustic Problem

The two-dimensional aeroacoustics problem is presented in this chapter. The inviscid flow around a NACA-0012 airfoil interacting with an isentropic vortex is simulated using an inviscid unsteady flow solver. The noise generated by the complex interaction between the vortex and the airfoil is then propagated to a far-field observer via a two-dimensional FW-H formulation in the frequency domain. The coupled aeroacoustic simulation is then linearized in forward or tangent mode and in reverse or adjoint mode. Upon successful validation, the adjoint linearization is used to minimize the noise signature of the airfoil through the application of optimal shape modifications. While two-dimensional adjoint-based aeroacoustic optimizations have been attempted before in the literature [39, 40], the invaluable experience gained in the two-dimensional context has helped to expedite the development of the three-dimensional aeroacoustic adjoint solver, which represent the unique and innovative aspect of this work.

2.1 Aerodynamic Solver

The two-dimensional base flow solver used here is an in-house unstructured-mesh Euler solver that has been validated for steady-state and time-dependent flows and contains a discrete tangent and adjoint sensitivity capability for both steady state and time-dependent flow problems. The flow solver is based on the conservative form of the Euler equations which may be written as:

$$\frac{\partial \mathbf{V}\mathbf{U}(\mathbf{x},t)}{\partial t} + \nabla \cdot \mathbf{F}(\mathbf{U}) = 0 \tag{2.1}$$

where **V** refers to the area of the control volume, the state vector **U** consists of the conserved variables in the Euler equations and the flux vector $\mathbf{F} = \mathbf{F}(\mathbf{U})$ contains the inviscid flux. The equations are closed with the perfect gas equation of state. The solver uses a cell-centered control volume formulation that is second-order accurate in space, where the inviscid flux integral S around a closed control volume is discretized as:

$$S = \int_{dB} [\mathbf{F}(\mathbf{U})] \cdot \mathbf{n} dB = \sum_{i=1}^{n_{edge}} \mathbf{F}_{e_i}^{\perp}(\mathbf{U}, \mathbf{n}_{ei}) B_{e_i} \tag{2.2}$$

In equation (2.2) B_e is the edge length, $\mathbf{n}_e$ is the unit normal of the edge, and $F_e^{\perp}$ is the normal flux across the edge. The flux is computed using the second-order accurate matrix dissipation scheme [41] as the sum of a central difference and an artificial dissipation term as shown below,

$$\begin{aligned} \mathbf{F}_e^{\perp} &= \frac{1}{2}\{\mathbf{F}_L^{\perp}(\mathbf{U}_L, V_e, \mathbf{n}_e) + \mathbf{F}_R^{\perp}(\mathbf{U}_R, V_e, \mathbf{n}_e) \\ &\quad + \kappa^{(4)}[T]|[\lambda]|[T]^{-1}\left\{(\nabla^2\mathbf{U})_L - (\nabla^2\mathbf{U})_R\right\}\} \end{aligned} \tag{2.3}$$

the left and right state vectors are $\mathbf{U}_L$ and $\mathbf{U}_R$ while $(\nabla^2\mathbf{U})_L$, $(\nabla^2\mathbf{U})_R$ are the left and right undivided Laplacians computed for any element i as

$$(\nabla^2\mathbf{U})_i = \sum_{k=1}^{neighbors} (\mathbf{U}_k - \mathbf{U}_i) \tag{2.4}$$

The time-derivative term is discretized using a second-order accurate backward-difference formula (BDF2) scheme as:

$$\frac{\partial V\mathbf{U}}{\partial t} = \frac{\frac{3}{2}V\mathbf{U}^n - 2V\mathbf{U}^{n-1} + \frac{1}{2}V\mathbf{U}^{n-2}}{\Delta t} \tag{2.5}$$

The discretization of the BDF2 scheme shown in equation (2.5) is based on a uniform time-step size and the index n is used to indicate the current time level. Denoting the spatial residual at time level n by the operator $S^n(\mathbf{U}^n)$, the resulting system of non-linear equations to be solved for the analysis problem at each time step can be written as:

$$\mathbf{R}^n = \mathbf{R}^n(\mathbf{U}^n, \mathbf{U}^{n-1}, \mathbf{U}^{n-2}) = \frac{\frac{3}{2}V\mathbf{U}^n - 2V\mathbf{U}^{n-1} - \frac{1}{2}V\mathbf{U}^{n-2}}{\Delta t} + \mathbf{S^n}(\mathbf{U^n}) = \mathbf{0} \tag{2.6}$$

The solution to equation (2.6) is computed using Newton's method as

$$\begin{gathered} \left[\frac{\partial \mathbf{R}^k}{\partial \mathbf{U}^k}\right] \delta\mathbf{U}^k = -\mathbf{R}^k \\ \mathbf{U}^{k+1} = \mathbf{U}^k + \delta\mathbf{U}^k \\ \delta\mathbf{U}^k \rightarrow 0, \mathbf{U}^n = \mathbf{U}^k \end{gathered} \tag{2.7}$$

To guarantee robustness of Newton's method, the Jacobian matrix $\left[\frac{\partial \mathbf{R}^k}{\partial \mathbf{U}^k}\right]$ employs a linearization of the first-order accurate spatial discretization of the Euler equation (2.1). Furthermore, to accelerate convergence for every timestep a dual timestepping technique [42] is used. The Jacobian matrix in equation (2.7) is inverted iteratively using a GMRES Krylov solver [43] preconditioned with a coloured Gauss-Seidel algorithm.

2.2 Airfoil Surface Parameterization and Mesh Deformation Algorithm

Since the ultimate goal of the current exercise is the optimal shape modification of the airfoil to reduce its noise signature, a geometry parameterization technique is introduced to modify the geometry of the baseline NACA-0012 airfoil.

Modifications to the baseline airfoil geometry are achieved by displacing the nodes of the airfoil using the Class function - Shape function Transformation geometry parameterization technique [44]. This parameterization technique defines the upper and lower surfaces of the airfoil as the product of a class function $C(x)$ and a shape function $S(x)$, as shown in equation (2.8).

$$\begin{aligned} y_{upper}(x) &= C(x)Su(x) \\ y_{lower}(x) &= C(x)Sl(x) \\ x &\in [0,1] \end{aligned} \tag{2.8}$$

The class function for the airfoil geometries considered in this work is defined in equation (2.9).

$$C(x) = \sqrt{x}(1-x) \tag{2.9}$$

The upper and lower surface shape functions, $Sl(x)$ and $Su(x)$, are defined in equation (2.10) and they are linear combinations of Bernstein polynomials $S_i(x)$.

$$\begin{aligned} Su(x) &= \sum_{i=1}^{N} Au_i S_i(x) \\ Sl(x) &= \sum_{i=1}^{N} Al_i S_i(x) \end{aligned} \tag{2.10}$$

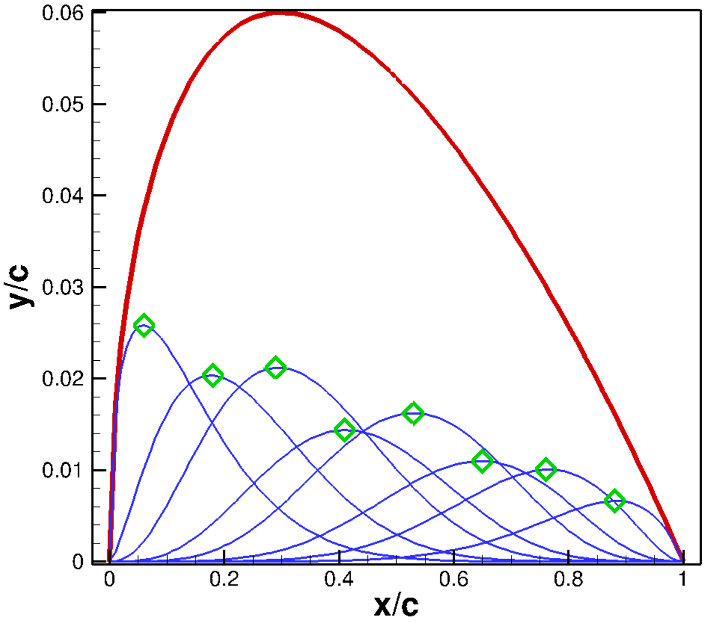

Figure 2.1: Schematic of the CST geometry parameterization technique for the NACA 0012 airfoil represented with Bernstein polynomials of order 8

The Bernstein polynomials of order N used in equation (2.10) are defined in equation (2.11).

$$S_i(x) = \frac{N!}{i!\,(N-i)!}\, x^i\,(1-x)^{N-1} \tag{2.11}$$

The weights Au_i and Al_i in equation (2.10) are used to scale the Bernstein polynomials for the airfoil's upper and lower surface, and represent the design variables for the optimization. A schematic of the geometry parameterization is shown in Figure 2.1.

Once the airfoil geometry, i.e. its surface mesh, has been defined according to the set of design variables $\mathbf{D} = [\mathbf{Au_i}, \mathbf{Al_i}]$, the displacements of the surface nodes need to be propagated to the interior mesh. This mesh deformation problem is solved with a spring analogy approach. In this approach the mesh is seen as a network of interconnected springs whose coefficients are assumed to be inversely proportional to the second power of the edges length. Two independent force balance equations are formulated for each node in response to the surface displacements. The resulting system of equations is solved using a GMRES Krylov solver preconditioned with a Jacobi algorithm, similar to the solution strategy for the flow solver. The governing equations for the mesh deformation problem can be written symbolically as:

$$\mathbf{G}(\mathbf{x}, \mathbf{D}) = \mathbf{0} \tag{2.12}$$

where **x** denotes the interior mesh coordinates and **D** denotes the shape parameters that define the surface geometry.

2.3 Two-dimensional Blade-Vortex Interaction Noise

The focus of the current exercise is to develop an adjoint-based framework to minimize blade-vortex interaction (BVI) noise. Blade vortex interaction noise happens when a rotor blade interacts with the vortices shed from a previous blade. To mimic this behavior in a two-dimensional context an isentropic vortex [45] is initialized in the steady flowfield computed around the NACA-0012 airfoil. The vortex is then convected downstream to realize an head-on interaction with the airfoil. The perturbation to the steady-state flowfield around the airfoil generated by the isentropic vortex is defined in equation (2.13)

$$\begin{aligned} \delta u &= -\frac{\alpha}{2\pi}(y - y_0)\exp\phi\left(1 - r^2\right) \\ \delta v &= \frac{\alpha}{2\pi}(x - x_0)\exp\phi\left(1 - r^2\right) \\ \delta T &= \frac{\alpha^2(\gamma - 1)}{16\phi\gamma\pi^2}\exp\phi\left(1 - r^2\right) \end{aligned} \tag{2.13}$$

The parameter ϕ controls the gradient of the solution while α determines the strength of the vortex, $r = \sqrt{(x - x_0)^2 + (y - y_0)^2}$ is the distance from the vortex center and $\gamma = 1.4$ is the ratio of specific heats. The vortex center coordinates are x_0 and y_0 and for the case of the head - on airfoil vortex interaction simulated in this work $x_0 = -4.0$ and $y_0 = 0$. The freestream Mach number is $M = 0.6$ and the angle of attack is zero. The vortex is initialized in the domain upstream of the airfoil as shown in Figure 2.2 and is freely convected downstream using the BDF2 time discretization in equation (2.5). The unsteady flowfield is computed for 256 timesteps of uniform size $dt = 0.4$ non-dimensionalized with the freestream speed of sound and every timestep is converged to machine precision as shown in Figure 2.3. The flowfield variables at each timestep are then used as input to the acoustic propagation module, as described in Section 2.4, to determine the noise signature at the acoustic observer.

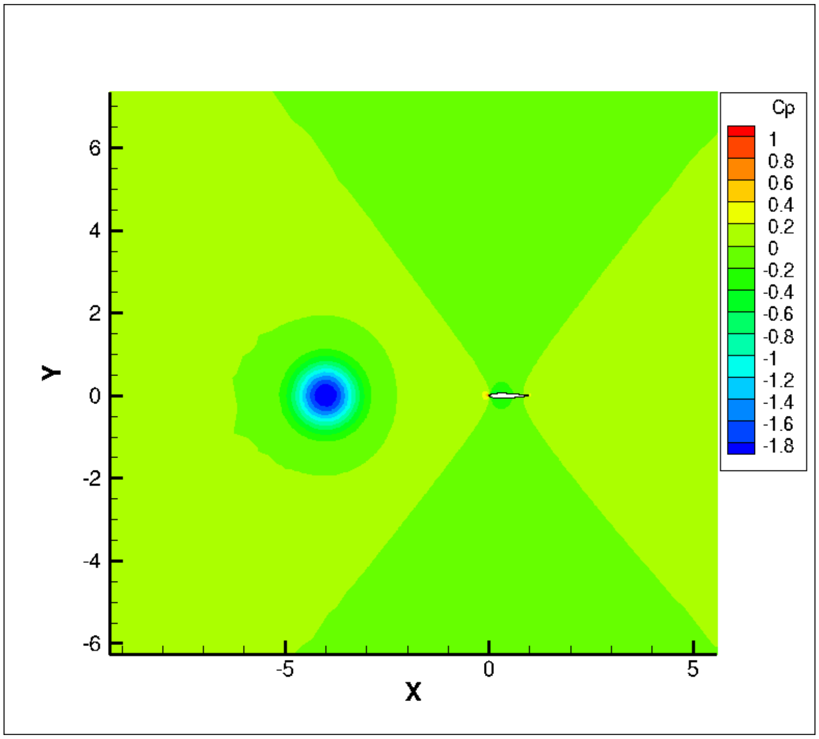

Figure 2.2: Initialization of the isentropic vortex in the steady state flowfield computed around the NACA-0012 airfoil.

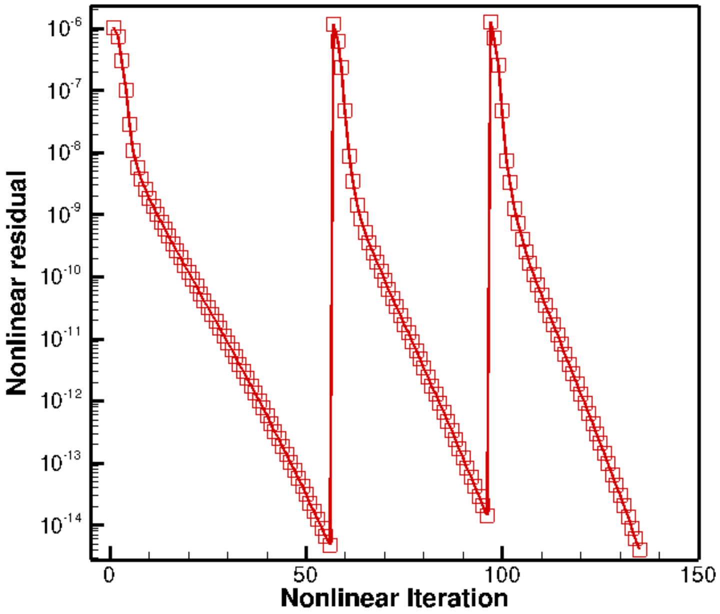

Figure 2.3: Residual convergence for the first three timestep of the unsteady CFD solution

2.4 Aeroacoustic Solver: the Two-dimensional FW-H Integration

After the complex aerodynamic environment around the blade vortex interaction has been determined, the noise signature of the airfoil at the farfield observer can be computed. Despite the continuous increase in computational resources, numerical simulations that resolve wave propagation from the nearfield to a farfield observer are still infeasible, hence a viable approach to predicting farfield noise level is the use of hybrid methods.

In hybrid methods, the finely resolved nearfield flow time history computed by a CFD solver is used as input to an acoustic integral formulation that predicts the noise radiated to a farfield observer. The acoustic formulations are often based on Lighthill's acoustic analogy, and in this work the Ffowcs-Williams and Hawkings (FW-H) acoustic integration has been used, as it is widely recognized as the workhorse in helicopter aeroacoustic applications [14]. Using the mathematical theory of distributions, Ffowcs-Williams and Hawkings [46] recombined the Navier-Stokes equation to arrive at the inhomogeneous wave equation that describes the noise generated by the relative motion between a body and a surrounding fluid. The FW-H equation can be expressed in differential form as [46]

$$\left(\frac{\partial^2}{\partial t} - c_0^2 \frac{\partial^2}{\partial x_i \partial x_j}\right)\left(H(f)\rho'\right) = -\frac{\partial F_i \delta(f)}{\partial x_i} + \frac{\partial Q \delta(f)}{\partial t} \tag{2.14}$$

where

$$Q = \left(\rho_o v_i + \rho\left(u_i - v_i\right)\right)\frac{\partial f}{\partial x_i} \tag{2.15}$$

and

$$F_j = \left(p\delta_{ij} + \rho u_i \left(u_j - v_j\right)\right)\frac{\partial f}{\partial x_i} \tag{2.16}$$

and the Lighthill's stress tensor, the quadrupole term, has been omitted since it is not used in this work. Equation (2.15) gives rise to an unsteady monopole-type contribution that can be associated with mass addition, while the dipole term, equation (2.16), involves an unsteady force. In equations (2.14), (2.15) and (2.16), the prime denotes perturbation relative to the freestream which itself is denoted with the subscript o, while x_i and t are Cartesian coordinates and time respectively. The function $f(x_i) = 0$ defines the surface of integration outside of which the solution is sought.

Density and pressure are ρ and p, and they are interpreted as the sum of their respective free-stream values and a perturbation as

$$\rho = \rho_o + \rho'$$
$$p = p_o + p'$$

The fluid velocities are u_i, while v_i are the surface velocities and c_o is the freestream speed of sound. Finally, $H(f)$ is the Heaviside function while $\delta(f)$ is the Dirac function.

The solution to the inhomogeneous wave equation (2.14) has been the subject of extensive research [13, 14, 47] and is computed by integrating the quantities in equation (2.15) and (2.16) over an acoustic integration surface. The integration surface can be the solid surface of the body moving in the surrounding fluid, as originally proposed by Ffowcs Williams and Hawkings, or an off-body permeable integration surface as proposed in [14,47]. For three-dimensional problems the acoustic integration is typically carried out in the time domain [13, 14] as described in Chapter 3. However, for two-dimensional applications Lockard [48] has derived a more efficient integration in the frequency domain that has been used for the two-dimensional BVI case considered in this work.

By assuming uniform rectilinear motion of both the surface and the acoustic observer, the solution to the two-dimensional differential FW-H equation in the frequency domain reads:

$$H(f)c_0^2\rho' = H(f)p' = -\oint_{f=0} F_i(\xi,\omega)\frac{\partial G(\mathbf{y},\xi)}{\partial \xi_i}dl - \oint_{f=0} Q(\xi,\omega)G(\mathbf{y},\xi)\mathbf{dl} \tag{2.17}$$

where $\mathbf{y}$ is the observer location, $\xi = (\xi,\eta)$ are the two-dimensional source coordinates on the integration surface $f = 0$, ω is the frequency, $Q(\xi,\omega)$ and $F_i(\xi,\omega)$ are the monopole and dipole terms in the frequency domain at the source locations and dl is the infinitesimal length along the surface $f = 0$.

The function

$$G(\mathbf{y},\xi) = \frac{i}{4\beta} \quad e^{\frac{Mk\bar{x}}{\beta^2}} H_0^2\left(\frac{k}{\beta^2}\sqrt{\bar{x}^2+\beta^2\bar{y}^2}\right) \tag{2.18}$$

is the free space Green's function, where H_0^2 is the Hankel function of second kind of order zero, and

$$\bar{x} = (x-\xi)\cos\theta + (y-\eta)\sin\theta$$
$$\bar{y} = -(x-\xi)\sin\theta + (y-\eta)\cos\theta$$

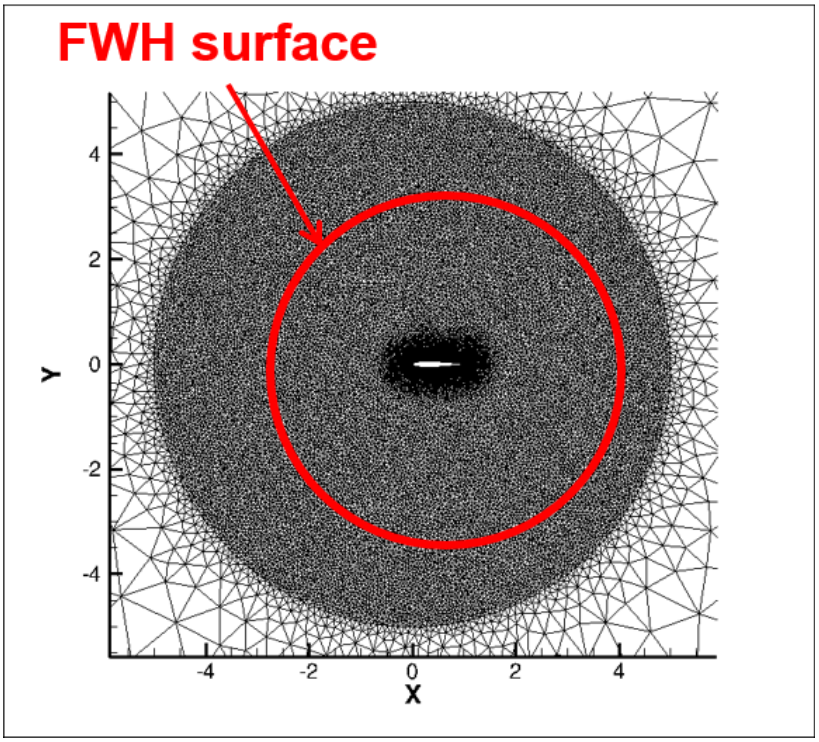

Figure 2.4: CFD mesh and approximate location of the FW-H integration surface

Here x and y are the observer coordinates, $\tan\theta = V/U$ with U and V being the freestream Cartesian velocities of the flow, $M = \sqrt{U^2+V^2}/c_o$ is the Mach number and $\beta = \sqrt{1-M^2}$ is the Prandtl-Glauert factor.

Numerical evaluation of the integral in equation (2.17) is performed as follows:

1. Definition of the integration surface $f(x_i) = 0$. The integration surface used in this work is a collection of edges from the unstructured CFD mesh. This set of edges is selected using a geometrical distance function criterion. The integration surface is placed four chords away from the airfoil and its approximate location is shown in Figure 2.4.

2. For every acoustic source on the FW-H acoustic integration surface, assemble the monopole and dipole term in equations (2.15) and (2.16) for every timestep of the CFD time-integration process.

3. Apply a window function to the monopole and dipole terms to account for the non-periodicity of their time histories. In this work the window function proposed by Lockard [48] has been

used.

4. Transform the monopole and dipole term to the frequency domain via a Fast Fourier Transform (FFT). While very efficient FFT algorithms are available [49], the one used in this exercise had to be implemented ex-novo to allow easy access to the source code for tangent and adjoint differentiation purposes.

   Note that steps 3 and 4 require the prior availability of the complete flow time history. For this reason the acoustic integration in the frequency domain can only be carried out at the end of the CFD time-integration process and can be considered a post-processing step of the CFD time-integration.

5. For each frequency in the Fourier Transform and for each observer location, compute the two-dimensional Green's function in equation (2.18) to evaluate the integral in equation (2.17) and determine the total acoustic pressure at the observer in the frequency domain. In this work the integral is evaluated with a one point Gaussian quadrature.

6. Perform inverse Fourier Transform (iFFT) to recover the acoustic pressure time history at the observer.

The current acoustic implementation has been validated against two analytical test cases, a monopole in uniform flow and the scattering of sound by an edge [48,50].

The complex potential for the monopole in uniform flow is given by Lockard [48] as

$$\phi(\mathbf{x},t) = Ae^{i\omega t}G(\mathbf{y},\xi) \tag{2.19}$$

where A is the amplitude, ω is the frequency, t is time and $G(\mathbf{y},\xi)$ is the Green's function defined in equation (2.18). Equation (2.19) gives the value of the potential at any point in space and time and the variables needed for the FW-H integration are obtained by taking the real part of $p' = -\rho_o(\frac{\partial\phi}{\partial t} + U_i\frac{\partial\phi}{\partial x_i})$, $u'_i = \frac{\partial\phi}{\partial x_i}$ and using the isentropic condition $\rho' = p'/c_o^2$. The FW-H is then validated by first evaluating the exact acoustic pressure at the observer location. Then all the variables needed to evaluate the FW-H integral in equation (2.17) are evaluated at the FW-H surface and the integration is performed. The acoustic prediction is then compared to the exact analytical solution. Results for this test case are presented in Figure 2.5: Figure 2.5(a) shows

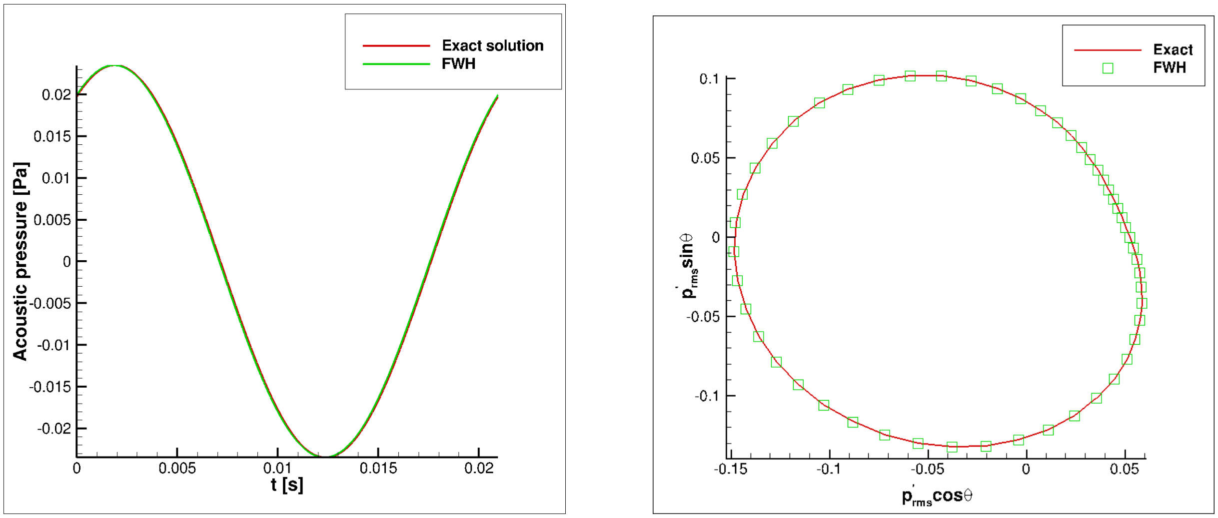

(a) Comparison between the exact acoustic pressure and the one computed by the two-dimensional FW-H acoustic integration for an observer at $r = 500m$, $\theta = 180deg$ for a monopole in uniform flow

(b) Directivity plot for the monopole in uniform flow for an observer at $r = 500m$

Figure 2.5: Validation of the two-dimensional acoustic integration for the monopole in uniform flow test case [48]

excellent agreement between the exact and the predicted acoustic pressure time histories for an observer at a radial distance $r = 500m$ and an azimuthal location $\theta = 180deg$. Figure 2.5(b) shows the root mean square of the acoustic pressure for the exact solution and the acoustic integration at different azimuthal locations but for the same radial distance $r = 500m$, confirming the accuracy of the acoustic integration.

The same procedure is followed for the scattering of sound by an edge. A vortex of strength k moves around the edge of a semi-infinite plate along the path shown in Figure 2.6. The vortex reaches its maximum speed when it is closest to the plate, reaching a Mach number $M = 0.001$. The potential for this flow is given by Crighton [50] as:

$$\phi(\mathbf{x},t) = \frac{2\sqrt{2}}{[M^2(r-t)^2+4]^{\frac{1}{4}}}\frac{sin(\frac{\theta}{2})}{r^{\frac{1}{2}}} \tag{2.20}$$

where $r = \sqrt{x^2+y^2}$ is the radial distance from the origin to a general (x,y) location in the 2D plane, non dimensionalized with the distance b in Figure 2.6 and θ is the angle measured relative to the positive x-axis. Results for this case are shown in Figure 2.7. Figure 2.7(a) compares the acoustic-pressure time histories for the exact solution and the acoustic integration at a radial

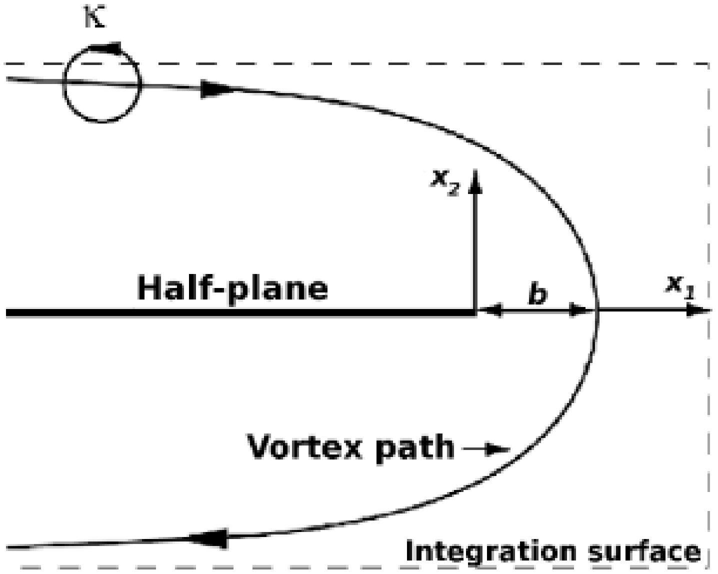

Figure 2.6: Schematic of the scattering by an edge from Rumpfkeil [51]

distance $r = 50m$ and $\theta = 0deg$, while Figure 2.7(b) shows the exact and predicted root mean square of the acoustic pressure for an observer at $r = 50m$ and different azimuthal locations. In both cases the agreement between the exact solution and the acoustic integration is excellent.

2.5 Tangent and Adjoint Formulations for the Two-dimensional Aeroacoustic Problem

To perform the efficient gradient-based aeroacoustic optimization of the NACA-0012 airfoil in blade-vortex interaction the adjoint sensitivities need to be derived for the coupled aeroacoustic problem. First, the tangent and adjoint sensitivities for the airfoil in vortex interaction are presented: for simplicity the sensitivities are derived for a BDF1 time discretization and the derivation closely follows that of Mani and Mavriplis [35]. The sensitivity formulation is then extended to include the tangent and adjoint acoustic sensitivities, to realize the coupled aeroacoustic sensitivity. The tangent sensitivity is derived first, while the adjoint sensitivity is obtained by transposing and reversing all the operations performed in forward mode. The tangent sensitivity is then validated with respect to the complex step method [52,53], while the adjoint sensitivity is validated with the

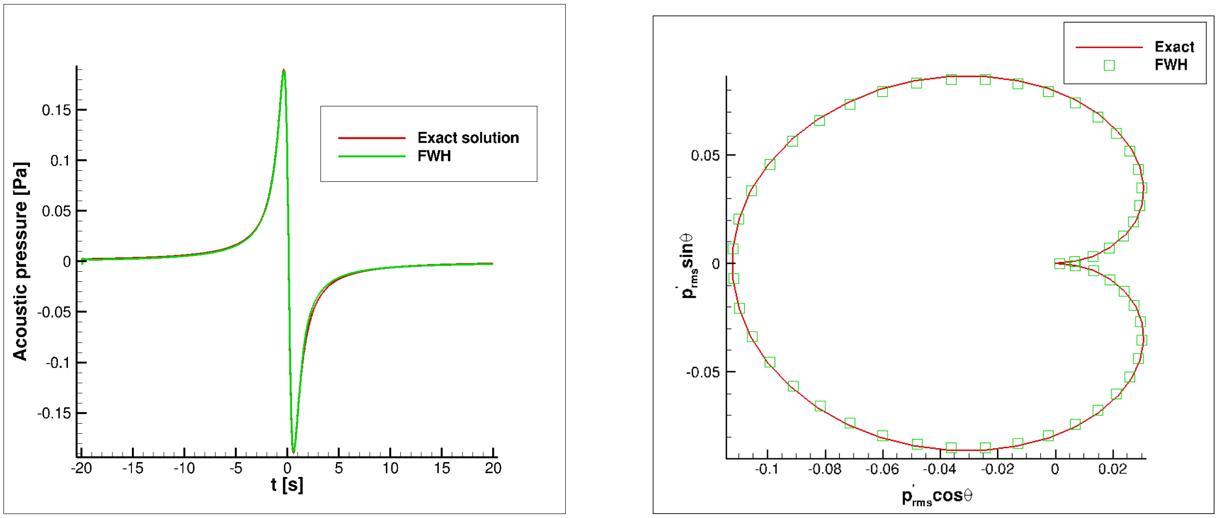

(a) Exact and FWH acoutic pressure solution for an observer at $r = 50m$ and $\theta = 0deg$ for a vortex passing over an edge

(b) Directivity plot for the vortex over edge flow for an observer at $r = 50m$

Figure 2.7: Validation of the acoustic solver for the scattering of sound by an edge [50]

duality relation [54] with the tangent model.

2.5.1 Sensitivity Analysis Formulation for Airfoil in Vortex Interaction

To derive the tangent and adjoint sensitivities for the airfoil in vortex interaction, the objective function L^n at the end of the time-integration process can be expressed as

$$L^n = L^n\left(\mathbf{U^n}(\mathbf{D}), \mathbf{x}(\mathbf{D})\right) \tag{2.21}$$

where $\mathbf{D}$ is the vector of design variables and $\mathbf{x}(\mathbf{D})$ is the vector of mesh coordinates that depends on the design variables, but not on time.

Differentiating equation (2.21) with respect to one design variable yields:

$$\frac{dL^n}{dD} = \frac{\partial L^n}{\partial \mathbf{U}^n}\frac{d\mathbf{U}^n}{dD} + \frac{\partial L^n}{\partial \mathbf{x}}\frac{d\mathbf{x}}{dD} \tag{2.22}$$

The flow residual at each timestep for a BDF1 time discretization scheme is given as

$$\mathbf{R}^n = \mathbf{R}^n\left(\mathbf{U}^n(\mathbf{D}), \mathbf{U}^{n-1}(\mathbf{D}), \mathbf{x}(\mathbf{D})\right) = \frac{\mathbf{V}\left(\mathbf{U}^n - \mathbf{U}^{n-1}\right)}{\Delta t} + \mathbf{S}^n(\mathbf{U}^n, \mathbf{n}) = 0 \tag{2.23}$$

and an expression for $\frac{d\mathbf{U}^n}{dD}$ to be used in equation (2.22) is obtained by differentiating equation (2.23) with respect to a design variable D

$$\frac{\partial \mathbf{R}^n}{\partial \mathbf{U}^n}\frac{d\mathbf{U}^n}{dD}+\frac{\partial \mathbf{R}^n}{\partial \mathbf{U}^{n-1}}\frac{d\mathbf{U}^{n-1}}{dD}+\frac{\partial \mathbf{R}^n}{d\mathbf{x}}\frac{d\mathbf{x}}{\partial D}=0 \tag{2.24}$$

and solving for the flow tangent sensitivity at timestep n as

$$\frac{d\mathbf{U}^n}{dD}=-\left[\frac{\partial \mathbf{R}^n}{\partial \mathbf{U}^n}\right]^{-1}\left(\frac{\partial \mathbf{R}^n}{\partial \mathbf{U}^{n-1}}\frac{d\mathbf{U}^{n-1}}{dD}+\frac{\partial \mathbf{R}^n}{d\mathbf{x}}\frac{d\mathbf{x}}{\partial D}\right) \tag{2.25}$$

In equation (2.25), $\left[\frac{\partial \mathbf{R}^n}{\partial \mathbf{U}^n}\right]$ is the exact second-order-accurate Jacobian of equation (2.23) that is inverted using the GMRES - Krylov algorithm used in the analysis problem. Equation (2.25) represents a forward integration in time where the initial condition $\frac{d\mathbf{U}^0}{dD}$ is given by the linearization of the vortex equations with respect to the design variables.

The term $\frac{d\mathbf{x}}{dD}$ is obtained from

$$[\mathbf{K}]\frac{d\mathbf{x}}{dD}=\frac{d\mathbf{x}_{surf}}{dD} \tag{2.26}$$

where $[\mathbf{K}]$ is the stiffness matrix of the mesh deformation problem as described in Section 2.2 and $\frac{d\mathbf{x}_{surf}}{dD}$ is the forward sensitivity of the mesh boundary nodes with respect to the design variables computed by linearization of the geometry paramterization described in Section 2.2. The system in equation (2.26) is solved with the same GMRES-Krylov algorithm described in Section 2.2.

Once the term $\frac{d\mathbf{U}^n}{dD}$ has been computed as per equation (2.25), the objective function sensitivity at the final timestep can be evaluated with the matrix vector products described in equation (2.22).

Equation (2.22) gives the sensitivity of the objective function in equation (2.21) with respect to one design variable D. However, for gradient-based optimization, the sensitivity of the objective function with respect to the full vector of design variables $\mathbf{D}$ is needed. Hence, the expensive forward time integration in equation (2.25) would need to be repeated for every design variable in the vector $\mathbf{D}$. A more efficient approach is to compute the adjoint sensitivity of the objective function by transposing and reversing all the operations performed in the tangent mode. Transposing equation (2.22) gives the reverse linearization of the objective function in equation (2.21)

$$\frac{dL^{n\,T}}{d\mathbf{D}}=\frac{d\mathbf{U}^{n\,T}}{d\mathbf{D}}\frac{\partial L^{n\,T}}{\partial \mathbf{U}^n}+\frac{d\mathbf{x}}{d\mathbf{D}}^T\frac{\partial L^{n\,T}}{\partial \mathbf{x}} \tag{2.27}$$

The term $\frac{d\mathbf{U}^{n\,T}}{d\mathbf{D}}$ is obtained by transposing equation (2.25) as

$$\frac{d\mathbf{U}^{n\,T}}{dD}=-\left(\frac{\partial \mathbf{R}^n}{\partial \mathbf{U}^{n-1}}\frac{d\mathbf{U}^{n-1}}{dD}+\frac{\partial \mathbf{R}^n}{\partial \mathbf{x}}\frac{d\mathbf{x}}{dD}\right)^T\left[\frac{\partial \mathbf{R}^n}{\partial \mathbf{U}^n}\right]^{-T} \tag{2.28}$$

So that equation (2.27) becomes

$$\frac{dL^{n}}{d\mathbf{D}}^{T} = -\left(\frac{d\mathbf{U}^{n-1}}{d\mathbf{D}}^{T}\frac{\partial\mathbf{R}^{n}}{\partial\mathbf{U}^{n-1}}^{T} + \frac{d\mathbf{x}}{d\mathbf{D}}^{T}\frac{\partial\mathbf{R}^{n}}{\partial\mathbf{x}}^{T}\right)\left[\frac{\partial\mathbf{R}^{n}}{\partial\mathbf{U}^{n}}\right]^{-T}\frac{\partial L^{n}}{\partial\mathbf{U}^{n}}^{T} + \frac{d\mathbf{x}}{d\mathbf{D}}^{T}\frac{\partial L^{n}}{\partial\mathbf{x}}^{T} \tag{2.29}$$

The flow adjoint variable at time level n is now defined as

$$\Lambda_{u}^{n} = \left[\frac{\partial\mathbf{R}^{n}}{\partial\mathbf{U}^{n}}\right]^{-T}\frac{\partial L^{n}}{\partial\mathbf{U}^{n}}^{T} \tag{2.30}$$

And equation (2.29) becomes

$$\frac{dL^{n}}{d\mathbf{D}}^{T} = -\frac{d\mathbf{U}^{n-1}}{d\mathbf{D}}^{T}\frac{\partial\mathbf{R}^{n}}{\partial\mathbf{U}^{n-1}}^{T}\Lambda_{u}^{n} + \frac{d\mathbf{x}}{d\mathbf{D}}^{T}\left(\frac{\partial L^{n}}{\partial\mathbf{x}}^{T} - \frac{\partial\mathbf{R}^{n}}{\partial\mathbf{x}}^{T}\Lambda_{u}^{n}\right) \tag{2.31}$$

The first term in equation (2.31) depends on the sensitivity $\frac{d\mathbf{U}^{n-1}}{d\mathbf{D}}^{T}$ at the previous timestep, which can be computed by evaluating equation (2.28) at timestep $n-1$ as

$$\frac{d\mathbf{U}^{n-1}}{dD}^{T} = -\left(\frac{\partial\mathbf{R}^{n-1}}{\partial\mathbf{U}^{n-2}}\frac{d\mathbf{U}^{n-2}}{dD} + \frac{\partial\mathbf{R}^{n-1}}{\partial\mathbf{x}}\frac{d\mathbf{x}}{dD}\right)^{T}\left[\frac{\partial\mathbf{R}^{n-1}}{\partial\mathbf{U}^{n-1}}\right]^{-T} \tag{2.32}$$

Substituting equation (2.32) into equation (2.31) and defining a new adjoint variable at timestep $n-1$ as

$$\Lambda_{u}^{n-1} = \left[\frac{\partial\mathbf{R}^{n-1}}{\partial\mathbf{U}^{n-1}}\right]^{-T}\frac{\partial R^{n}}{\partial\mathbf{U}^{n-1}}^{T}\Lambda_{u}^{n} \tag{2.33}$$

equation (2.31) becomes

$$\frac{dL^{n}}{d\mathbf{D}}^{T} = -\frac{d\mathbf{U}^{n-2}}{d\mathbf{D}}^{T}\frac{\partial\mathbf{R}^{n-1}}{\partial\mathbf{U}^{n-2}}^{T}\Lambda_{u}^{n-1} + \frac{d\mathbf{x}}{d\mathbf{D}}^{T}\left(\frac{\partial L^{n}}{\partial\mathbf{x}}^{T} - \sum_{i=n-1}^{n}\frac{\partial\mathbf{R}^{i}}{\partial\mathbf{x}}^{T}\Lambda_{u}^{i}\right) \tag{2.34}$$

Equation (2.34) now depends on the sensitivity $\frac{d\mathbf{U}^{n-2}}{d\mathbf{D}}^{T}$ at timestep $n-2$, hence equation (2.31) represents a backward time integration for the flow adjoint variable that at a given time level k is given by

$$\Lambda_{u}^{k} = -\left[\frac{\partial\mathbf{R}^{k}}{\partial\mathbf{U}^{k}}\right]^{-T}\left[\frac{\partial\mathbf{R}^{k+1}}{\partial\mathbf{U}^{k}}^{T}\Lambda_{u}^{k+1}\right] \tag{2.35}$$

where $\left[\frac{\partial\mathbf{R}^{n}}{\partial\mathbf{U}^{n}}\right]^{T}$ is the transpose of the second-order-accurate flow Jacobian that is inverted iteratively using a GMRES - Krylov algorithm preconditioned with a colored Gauss - Seidel iteration scheme. The final (initial) term $\frac{d\mathbf{U}^{0}}{d\mathbf{D}}^{T}$ is taken from the linearization of the vortex equations with respect to the design parameter in reverse mode. At the end of the backward time integration the sensitivity vector is

$$\frac{dL^n}{d\mathbf{D}}^T = \frac{d\mathbf{x}}{d\mathbf{D}}^T \left(\frac{\partial L^n}{\partial \mathbf{x}}^T - \sum_{i=1}^{n} \frac{\partial \mathbf{R}^i}{\partial \mathbf{x}}^T \Lambda_u^i \right) \tag{2.36}$$

By transposing equation (2.26), the term $\frac{d\mathbf{x}}{d\mathbf{D}}^T$ becomes

$$\frac{d\mathbf{x}}{d\mathbf{D}}^T = \frac{d\mathbf{x}_{surf}}{d\mathbf{D}}^T [\mathbf{K}]^T \tag{2.37}$$

and substituting equation (2.37) into equation (2.36) the mesh adjoint problem can be defined as

$$\Lambda_x = [\mathbf{K}]^{-T} \left[\frac{\partial L^n}{\partial \mathbf{x}}^T - \sum_{i=1}^{n} \frac{\partial \mathbf{R}^i}{\partial \mathbf{x}}^T \Lambda_u^i \right] \tag{2.38}$$

The system is solved with a Jacobi preconditioned GMRES - Krylov algorithm. Finally, the sensitivity vector $\frac{dL^n}{d\mathbf{D}}^T$ is given by the product

$$\frac{dL^n}{d\mathbf{D}}^T = \frac{d\mathbf{x}_{\mathbf{surf}}}{d\mathbf{D}}^T \Lambda_x \tag{2.39}$$

where the term $\frac{d\mathbf{x}_{\mathbf{surf}}}{d\mathbf{D}}^T$ is the known sensitivity of the boundary nodes with respect to the design variables. For the two-dimensional optimizations presented in Chapter 4 the linear systems in equations (2.35) and (2.38) are both converged to machine precision as shown in Figure 2.8
In the case of a time-integrated objective function, equation (2.21) is modified as

$$L^g = L^g \left(L^1, L^2 \cdots, L^n \right) \tag{2.40}$$

and its forward linearization is

$$\frac{dL^g}{d\mathbf{D}} = \sum_n \left[\frac{\partial L^g}{\partial L^n} \frac{\partial L^n}{\partial \mathbf{U}^n} \frac{d\mathbf{U}^n}{dD} + \frac{\partial L^g}{\partial L^n} \frac{\partial L^n}{\partial \mathbf{x}} \frac{d\mathbf{x}}{dD} \right] \tag{2.41}$$

with $\frac{d\mathbf{U}^n}{dD}$ and $\frac{d\mathbf{x}}{dD}$ that are still computed from equations (2.25) and (2.26). The term $\frac{\partial L^g}{\partial L^n}$ is the derivative of the global (time-integrated) objective function L^g with respect to the local (instantaneous) objective function L^n. Transposing equation (2.41) gives the adjoint or reverse linearization of equation (2.40) as

$$\frac{dL^g}{d\mathbf{D}}^T = \sum_n \left[\frac{d\mathbf{U}^n}{d\mathbf{D}}^T \frac{\partial L^n}{\partial \mathbf{U}^n}^T \frac{\partial L^g}{\partial L^n}^T + \frac{d\mathbf{x}}{d\mathbf{D}}^T \frac{\partial L^n}{\partial \mathbf{x}}^T \frac{\partial L^g}{\partial L^n}^T \right] \tag{2.42}$$

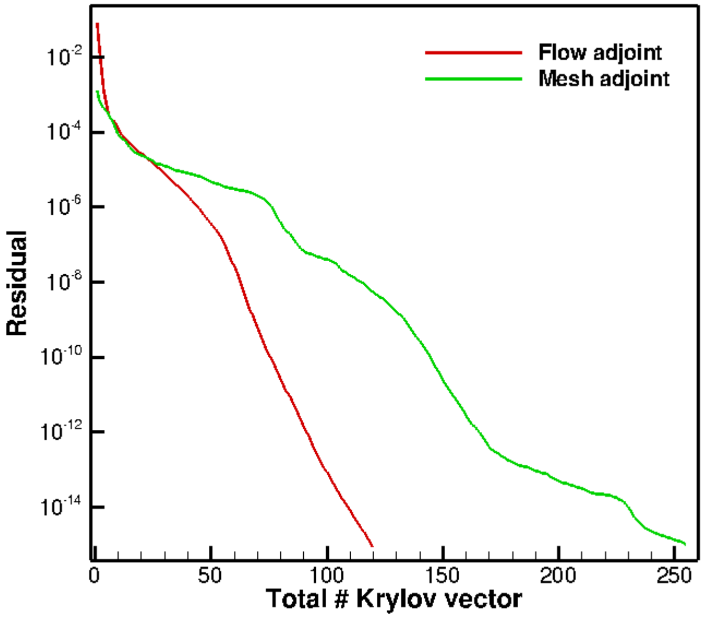

Figure 2.8: Residual convergence for the flow adjoint problem at a generic timestep and the final mesh adjoint problem

Substituting again equation (2.28) into equation (2.42) and following the same rationale used to arrive at equation (2.35), the flow adjoint equation for a time-integrated objective function now becomes

$$\Lambda_u^k = -\left[\frac{\partial \mathbf{R}^k}{\partial \mathbf{U}^k}\right]^{-T}\left[\frac{\partial \mathbf{L}^k}{\partial \mathbf{U}^k}^T \frac{\partial \mathbf{L}^g}{\partial \mathbf{L}^k}^T + \frac{\partial \mathbf{R}^{k+1}}{\partial \mathbf{U}^k}^T \Lambda_u^{k+1}\right] \tag{2.43}$$

and at the end of the backward time integration process the mesh adjoint equation can be computed as

$$\Lambda_x = [\mathbf{K}]^{-T}\sum_{i=1}^{n}\left[\frac{\partial L^g}{\partial L^i}^T \frac{\partial L^i}{\partial \mathbf{x}}^T - \frac{\partial \mathbf{R}^i}{\partial \mathbf{x}}^T \Lambda_u^i\right] \tag{2.44}$$

so that the final sensitivity in equation (2.42) becomes

$$\frac{dL^g}{d\mathbf{D}}^T = \frac{d\mathbf{x}_{\mathbf{surf}}}{d\mathbf{D}}^T \Lambda_x \tag{2.45}$$

Hence, as described by Mani and Mavriplis [35], the only difference between the time-integrated and the non-time-integrated objective function is the pre/post multiplication of the terms $\frac{\partial L^n}{\partial \mathbf{U}^n}$ and $\frac{\partial L^n}{\partial \mathbf{x}}$ by the global-to-local sensitivity $\frac{\partial L^g}{\partial L^n}$ for the forward/adjoint sensitivity respectively. The two terms $\frac{\partial L^n}{\partial \mathbf{U}^n}^T$ and $\frac{\partial L^n}{\partial \mathbf{x}}^T$ drive the backward adjoint time integration: in the case of the acoustic optimization these terms come from the adjoint linearization of the FW-H acoustic module as explained in Section 2.5.2.

Verification of the Aerodynamic Sensitivities for the Airfoil in Blade-vortex Interaction

The tangent linearization has been verified against the complex step method [52,53]. Any function $f(x)$ operating on a real variable x can be used to compute both the function and its derivative $f'(x)$ if the input variable x and all the intermediate variables used in the discrete evaluation of $f(x)$ are redefined as complex variables. In this case for a complex input the function will produce a complex output. A Taylor series of the now complex function $f(x+ih)$, where h is a small step-size and i is the imaginary unit, reads

$$f(x+ih) = f(x) + ihf'(x) + O\left(h^2\right) \tag{2.46}$$

from which the real part is simply the function value at x, while from the imaginary part the function derivative can be easily evaluated as

$$f'(x) = \frac{Im\left[f(x+ih)\right]}{h} \tag{2.47}$$

Despite requiring a step size, as in the case of finite-differencing, the complex step method is insensitive to small step-sizes since no differencing is required. Hence, by using a step size $h = 10^{-31}$ the tangent formulation for the blade vortex interaction case can be verified to machine precision against the complex step method.

The adjoint sensitivities are then verified with the duality relationship [54] between the tangent and the adjoint formulations. Table 2.1 shows the comparison between the adjoint linearization and the complex step method for the 7th design variable for the time-integrated aerodynamic objective function defined in equation (4.1). The error between the complex step method and the flow adjoint is of the order of machine precision, thus verifying the correctness of the adjoint linearization.

Table 2.1: Complex step validation of the 7th design sensitivity of the flow adjoint.

Adjoint	Complex	Error
-1.7854017702037789E-01	-1.7854017702038E-01	-2.10942374678780E-15

2.5.2 Sensitivity Analysis for the FW-H Equation

To enable adjoint-based aeroacoustic optimization the tangent and adjoint differentiation of the FW-H acoustic integration needs to be derived. The linearizations of the acoustic integrals will then be coupled to the corresponding tangent and adjoint linearizations of the CFD flow solver to realize the tangent and adjoint linearizations of the coupled aeroacoustic problem.

The functional dependencies for the quantities in the acoustic integrals in equation (2.17) are shown in equation (2.48)

$$\begin{aligned} Q &= Q\left(\mathbf{x}_s(\mathbf{D}),\mathbf{U}(\mathbf{D}),\omega\right) \\ F_i &= F_i\left(\mathbf{x}_s(\mathbf{D}),\mathbf{U}(\mathbf{D}),\omega\right) \\ G &= G\left(\mathbf{x}_s(\mathbf{D}),\mathbf{x}_o,\omega\right) \\ \frac{\partial G}{\partial \mathbf{x}_s} &= \frac{\partial G}{\partial \mathbf{x}_s}\left(\mathbf{x}_s(\mathbf{D}),\mathbf{x}_o,\omega\right) \end{aligned} \tag{2.48}$$

where $\mathbf{x_s}(\mathbf{D})$ is the discrete source location on the discrete FW-H integration surface, $\mathbf{x_o}$ is the observer location and ω is the frequency. From equation (2.48) it is evident that the monopole and dipole terms depend on the design parameters **D** through both the FW-H surface geometry and the input CFD solution. The acoustic pressure at the observer can then be expressed as

$$p'(\mathbf{D},\omega) = \mathbf{FWH}(\mathbf{U}(\mathbf{D},\omega),\mathbf{x}(\mathbf{D}),\omega) \tag{2.49}$$

where $FWH(\mathbf{U}(\mathbf{D},\omega),\mathbf{x}(\mathbf{D}),\omega)$ represents all the discrete operations necessary to evaluate equation (2.17) numerically, as described in Section 2.4. Differentiation of equation (2.49) with respect to one design variable yields the pressure sensitivity at the observer as

$$\frac{dp(\mathbf{D},\omega)}{dD} = \sum_n \frac{\partial FWH}{\partial \mathbf{U^n_{FWH}}}\frac{d\mathbf{U^n_{FWH}}}{dD} + \frac{\partial FWH}{\partial x_{FWH}}\frac{dx_{FWH}}{dD} \tag{2.50}$$

where $\frac{d\mathbf{U^n_{FWH}}}{dD}$ is the tangent CFD solution at the $n-th$ timestep evaluated at the FW-H surface location, and $\frac{dx_{FWH}}{dD}$ is the CFD mesh sensitivity at the FWH integration surface. The matrices

$\frac{\partial FWH}{\partial \mathbf{U}_{FWH}}$ and $\frac{\partial FWH}{\partial \mathbf{x}_{FWH}}$ have been obtained by forward linearization of each component in the acoustic integration.

The time-integrated acoustic objective function used in this work is the overall sound pressure level (OSPL) at the observer location, defined as in equation (2.51):

$$L_{FWH} = OSPL(p(D)) = 20\log_{10}\left(\frac{p'_{RMS}}{p_0}\right) \tag{2.51}$$

Here p'_{RMS} is the root mean square of the acoustic pressure at the observer as computed by the FW-H acoustic integration and $p_0 = 20\mu Pa$ is a reference pressure. Thus the final form of the aeroacoustic objective sensitivity reads:

$$\begin{aligned} \frac{dL_{FWH}}{dD} &= \frac{\partial SPL}{\partial p}\frac{dp}{dD} = \frac{\partial SPL}{\partial p}\left[\sum_n \frac{\partial FWH}{\partial \mathbf{U^n_{FWH}}}\frac{d\mathbf{U^n_{FWH}}}{dD} + \frac{\partial FWH}{\partial x_{FWH}}\frac{dx_{FWH}}{dD}\right] \\ &= \sum_n \frac{\partial L^n_{FWH}}{\partial U^n_{FWH}}\frac{dU^n_{FWH}}{dD} + \frac{\partial L_{FWH}}{\partial x_{FWH}}\frac{dx_{FWH}}{dD} \end{aligned} \tag{2.52}$$

The flow and the acoustic analysis codes are loosely coupled and, as stated before, the FW-H acoustic propagation model can be considered a post-processing step of the unsteady CFD simulation. All the two-dimensional aeroacoustic simulations are carried out on a computational mesh consisting of approximately 60000 elements. The non-conserved variables of the CFD solution must be extracted at the source locations on the FW-H integration surface for the complete time history to assemble the monopole and dipole terms in equations (2.15) and (2.16). Since the CFD solver is a cell-centered solver and the FW-H surface is a concatenation of edges from the unstructured CFD mesh, an unlimited least-square gradient reconstruction procedure is employed to guarantee second-order accuracy while extracting the CFD data at the acoustic surface location. The edges of the FW-H surface are chosen using a wall distance criterion four chords away from the airfoil and the approximate location of the integration surface is shown in Figure 2.4. The extracted CFD solution time history is then used as input to the FW-H acoustic solver and the acoustic objective function can be computed. The same procedure is followed to couple the tangent flow and the tangent acoustic codes. The complete time history of the tangent flow sensitivity must be reconstructed at the FW-H integration surface, then both the flow and the mesh sensitivities at the integration surface can be passed as input to the tangent FW-H solver and finally the sensitivity of the time-integrated objective function, the overall sound pressure level at the observer, can be

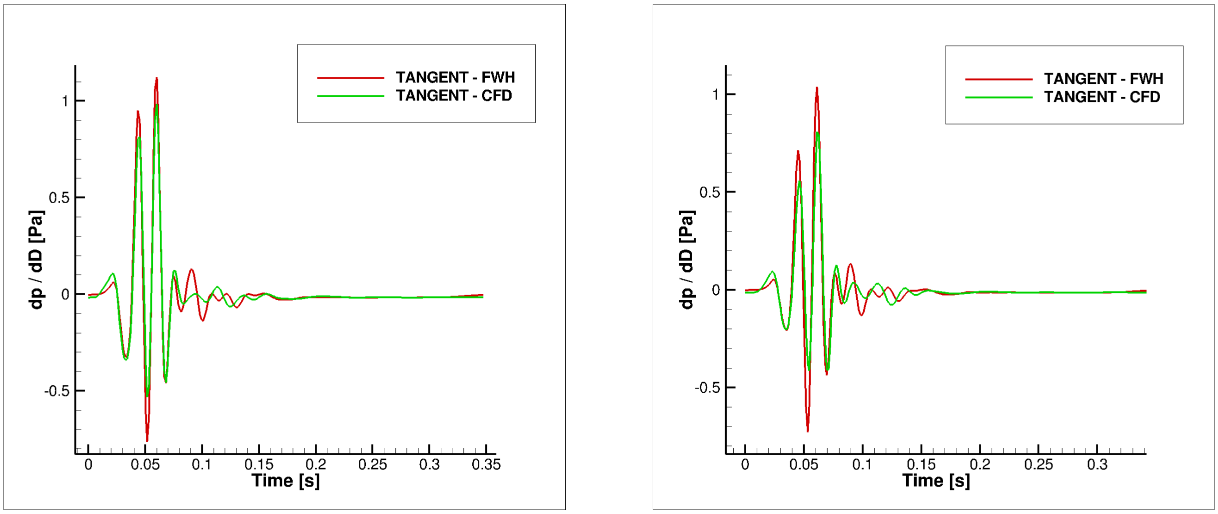

(a) Propagated and computed acoustic pressure sensitivity for an observer 0.4 chords away from the FW-H integration surface

(b) Propagated and computed acoustic pressure sensitivity for an observer 1.5 chords away from the FW-H integration surface

Figure 2.9: Comparison of FW-H propagated and CFD computed acoustic pressure sensitivity at different observer locations highlighting the detrimental effect that numerical dissipation has on the computed acoustic pressure sensitivity as the observer is moved to the far field.

computed. Hence, the sensitivity in equation (2.52) can be computed once the vectors $\frac{d\mathbf{U}^n}{dD}$ and $\frac{d\mathbf{x}}{dD}$ are known at the FW-H surface from the flow and mesh tangent problem. Therefore the tangent FW-H solver can be considered a post-processing step of the flow tangent problem. A comparison between the propagated and the computed observer acoustic pressure sensitivity is shown in Figure 2.9 for two different observer locations. In Figure 2.9(a) the observer is placed underneath the airfoil at the center of a CFD cell approximately 0.4 chords away from the FW-H integration surface while in Figure 2.9(b) the observer is placed approximately 1.5 chords away and for both cases the acoustic pressure sensitivity computed by the tangent flow solver can be compared to that propagated by the tangent FW-H solver. Figure 2.9 shows good agreement between the two codes. Note that the tangent CFD solution consistently underestimates all the peaks in the sensitivity time history, a consequence of the numerical dissipation associated with the employed spatial discretization. Furthermore, this behaviour deteriorates as the observer is placed further away from the FW-H integration surface.

Transposing equation (2.52) yields the adjoint linearization of the acoustics objective fuction as

Table 2.2: Finite difference validation of the 7th design sensitivity.

Adjoint	FD	Error
-3.1819940460451508E-03	-3.17975314778490E-03	2.24089826024758E-06

$$\frac{dL_{FWH}}{dD}^{T} = \sum_{n} \frac{dU^{n}}{dD}^{T} \frac{\partial L_{FWH}^{n}}{\partial U^{n}}^{T} + \frac{dx}{dD}^{T} \frac{\partial L_{FWH}}{\partial x}^{T} \tag{2.53}$$

The terms $\frac{\partial L_{FWH}^{n}}{\partial U_{FWH}^{n}}^{T}$ and $\frac{\partial L_{FWH}}{\partial x}^{T}$ are known once the products $\frac{\partial FWH}{\partial \mathbf{U}_{FWH}}^{T} \frac{\partial SPL}{\partial p'}^{T}$ and $\frac{\partial FWH}{\partial \mathbf{x}_{FWH}}^{T} \frac{\partial SPL}{\partial p'}^{T}$ have been evaluated. These two matrix - vector products are the adjoint linearization of the discrete FW-H equation and are obtained by transposition of the corresponding matrices in the forward linearization. Equation (2.53) is now in the form of equation (2.42) and the backward time integration described in Section 2.5.1 can start with the terms $\frac{\partial L^{n}}{\partial U^{n}}^{T} = \frac{\partial L_{FWH}^{n}}{\partial U_{FWH}^{n}}^{T} = \frac{\partial FWH}{\partial \mathbf{U}_{FWH}}^{T} \frac{\partial SPL}{\partial p}^{T}$ and $\frac{\partial L}{\partial x}^{T} = \frac{\partial L_{FWH}}{\partial x}^{T} = \frac{\partial FWH}{\partial \mathbf{x}_{FWH}}^{T} \frac{\partial SPL}{\partial p}^{T}$ provided by the adjoint linearization of the acoustic integration. Hence, the adjoint of the acoustic module can be considered a preprocessing step to the flow adjoint solver described in Section 2.5.1: once the two terms $\frac{\partial L_{FWH}^{n}}{\partial U_{FWH}^{n}}^{T}$ and $\frac{\partial L_{FWH}}{\partial x}^{T}$ are known the flow adjoint solver can start as described in Section 2.5.1.

The tangent and FW-H integration have been verified with a finite-difference approach as the complex-step method [52, 53] is not applicable in this case since the acoustic analysis equation itself includes complex variables via the Fourier transform and the Green's function in equation (2.17). The adjoint solver has then been validated by the duality-relation [54] to the tangent solver to machine precision. Table 2.2 shows the finite difference validation of the 7th adjoint design sensitivity. A second-order-accurate centered finite-difference scheme with a step $\delta D = 10^{-4}$ has been used.

With minor modifications the coupling strategy for the two-dimensional tangent and adjoint aeroacoustic linearizations will be applied to the three dimensional problem, the main differences resulting from the time-domain formulation for the three-dimensional FW-H acoustic integration as described in Chapter 3.

Chapter 3

Three Dimensional Aeroacoustic Problem for Helicopter Rotors

The three-dimensional adjoint-based multidisciplinary design capability is introduced in this chapter. The design tool encompasses the three disciplines of aerodynamics, structural mechanics and aeroacoustics. First, the solver for each discipline is presented, with particular emphasis on the acoustic integration. The coupling of the three discipline is then discussed and the linearization of the coupled multidisciplinary unsteady problem is introduced.

3.1 Aerodynamic Solver

The base flow solver used in this work is the NSU3D unstructured mesh Reynolds-averaged Navier-Stokes solver [41,55]. NSU3D has been widely validated for steady-state and time-dependent flows and is augmented with a discrete tangent and adjoint sensitivity capability which has been demonstrated previously for optimization of steady-state and time-dependent flow problems. As such, only a concise description of these formulations will be given in this thesis, with additional details available in references [32,54,56]. The flow solver is based on the conservative form of the Navier-Stokes equations which may be written as:

$$\frac{\partial \mathbf{u}(\mathbf{x},t)}{\partial t} + \nabla \cdot \mathbf{F}(\mathbf{u}) = 0 \tag{3.1}$$

For moving mesh problems these are written in arbitrary Lagrangian-Eulerian (ALE) form as:

$$\frac{\partial V\mathbf{u}}{\partial t} + \int_{dB(t)} [\mathbf{F}(\mathbf{u}) - \dot{\mathbf{x}}\mathbf{u}] \cdot \mathbf{n} dB = 0 \tag{3.2}$$

Here V is the control volume, $\dot{\mathbf{x}}$ is the vector of mesh face velocities, $\mathbf{n}$ is the unit normal of the face, and $B(t)$ is the surface area of the time varying control volume. The state vector $\mathbf{u}$ consists of the conserved variables and the Cartesian flux vector $\mathbf{F} = (\mathbf{F}_x, \mathbf{F}_y, \mathbf{F}_z)$ contains both inviscid and viscous fluxes. The equations are closed with the perfect gas equation of state and the Spalart-Allmaras turbulent eddy viscosity model [57] for all cases presented in this work. The time derivative term is discretized using a second-order accurate backward-difference formula (BDF2) scheme and the implicit residual is solved using Newton's method. The Jacobian matrix is inverted iteratively using a line-implicit agglomeration multigrid scheme that can also be used as a preconditioner for a GMRES Krylov solver [58]. For the remainder of this chapter, the system of non-linear equations for the CFD analysis problem will be represented by the generalized notation:

$$\mathbf{R}(\mathbf{u}, \mathbf{x}) = 0 \tag{3.3}$$

where the vector $\mathbf{u}$ denotes the flow values, $\mathbf{x}$ represents the CFD mesh coordinates, and equation (3.3) denotes the simultaneous solution of all time steps.

3.2 Structural Dynamics Solver

The structural dynamics of the blade are modeled with an Hodges-Dowell [59], non-linear, bend-twist finite-element model that is well suited for rotary-wing aircraft structures. The model has previously been developed and coupled to the NSU3D flow solver for both steady [60, 61] and time-dependent problems [62]. Figure 3.1 shows a typical beam with 15 degrees of freedom per element to accommodate bend wise, lag wise, axial and torsional displacements. The second-order equation of motion for the beam can be expressed as: $M\ddot{q} + C\dot{q} + Kq = F$. Here $[M]$, $[C]$ and $[K]$ are mass, damping and stiffness matrices of the system of equations representing the beam. The vector $F = F(t)$ is the forcing vector, while $\mathbf{q}$ represents the displacements along all degrees of freedom. This set of equations can be reduced to a first-order system and solved using a second-order backward difference formula (BDF2) time integration with standard Newton-type linearization and

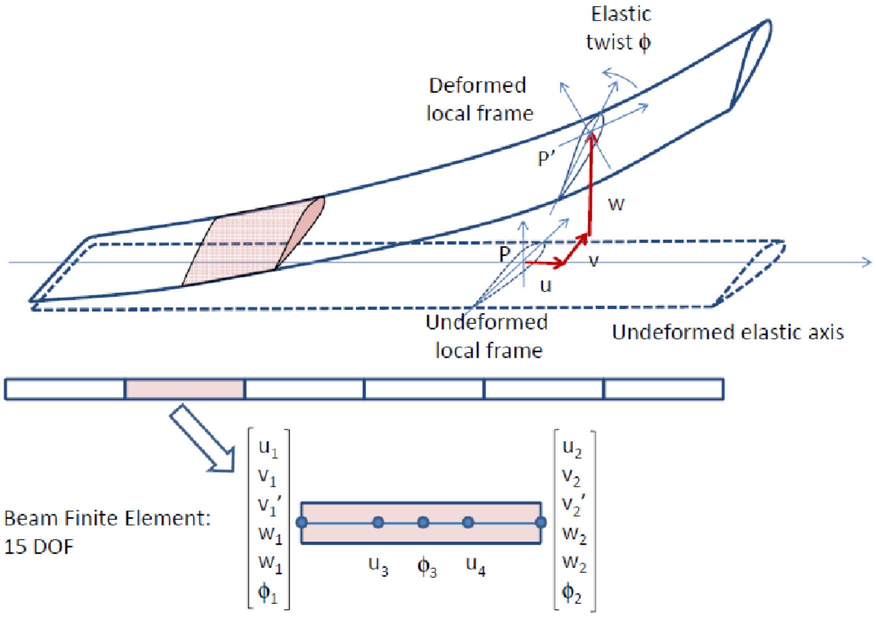

Figure 3.1: Beam element with flap, lag, torsional and axial (total 15) degrees of freedom.

sub-iterations to efficiently invert the implicit system: $[I]\dot{\mathbf{Q}}+[A]\mathbf{Q}=\mathbf{F}$, where $[I]$ is the identity matrix, $\mathbf{Q}=[\mathbf{q},\dot{\mathbf{q}}]^T$, $\mathbf{F}=[0,\ [M]^{-1}F]^T$ and $[A]=\begin{bmatrix} 0 & -[I] \\ [M]^{-1}[K] & [M]^{-1}[C] \end{bmatrix}$. The residual of the structural equations can be defined as: $\mathbf{J}=[I]\ \dot{\mathbf{Q}}+[A]\ \mathbf{Q}-\mathbf{F}=0$, and can be expressed in a simplified form as:

$$\mathbf{J}(\mathbf{Q},\mathbf{F})=\mathbf{0} \tag{3.4}$$

The beam model for the applications presented in Chapter 4 consists of 20 elements per blade and has been validated for the standard HART-II rotor case [5] by comparing its natural frequency predictions with the predictions from other reliable computational structural dynamics models, such as UMARC [63] and DLR [64], as shown in Table 3.1. Tangent and adjoint linearizations of the structural model have been developed and coupled to the NSU3D flow solver as shown in previous work [62].

Table 3.1: Comparison of HART-II Natural Frequencies [65]

Modes	**Present Model**	**UMARC**	**DLR**
Flap 1	1.104	1.112	1.125
Flap 2	2.802	2.843	2.835
Flap 3	5.010	5.189	5.168
Torsion 1	3.878	3.844	3.845

3.2.1 Fluid-structure Interface

In addition to the solution of the aerodynamic problem and the structural dynamics problem, the solution of the fully coupled time-dependent aeroelastic problem requires the exchange of aerodynamic loads from the CFD solver to the beam structure, which in turn returns surface displacements to the fluid flow solver. In practice, the fluid-structure-interface computes forces at each CFD surface mesh point $\mathbf{F}(\mathbf{x},\mathbf{u})$ by integrating the surface stresses (pressure and shear) over the surface area associated with each surface grid point. These forces are then projected onto the beam finite-element basis functions where they are assembled in the form of forces on the beam finite-element nodal locations denoted as $\mathbf{F_b}$. Conversely, once the beam deflections have been computed, the structural displacements are transferred back to the surface CFD mesh in a similar manner. The governing equations for the FSI can be written in residual form as:

$$\begin{aligned} \mathbf{S}(\mathbf{F_b},\mathbf{x},\mathbf{u}) &= \mathbf{F_b} - [T(\mathbf{Q})]\mathbf{F}(\mathbf{x},\mathbf{u}) = 0 \\ \mathbf{S}^{'}(\mathbf{x_s},\mathbf{Q}) &= \mathbf{x_s} - [T(\mathbf{Q})]^T\mathbf{Q} = 0 \end{aligned} \tag{3.5}$$

In equation (3.5), $[T]$ represents the rectangular transfer matrix that projects the CFD loads $\mathbf{F}(\mathbf{x},\mathbf{u})$ on the beam model, while its transpose $[T]^T$ is used to obtain the CFD surface coordinates $\mathbf{x_s}$ from the CSD degrees of freedom $\mathbf{Q}$

3.3 Prescribed Blade Motion

The time-dependent simulation of a rotor in forward flight requires a prescribed blade motion capability, in particular the individual blade cycling pitching motion must be superimposed with a simple solid body rotation of the entire rotor blade system and CFD mesh that contains the rotor.

For each blade, the time-dependent pitch angle can be represented by a combination of mean pitch angle and several harmonic components:

$$\theta = \theta_0 + \sum_{i=1}^{n} \theta_{c_i} \cos(i\psi) + \sum_{i=1}^{n} \theta_{s_i} \sin(i\psi) \tag{3.6}$$

where ψ is the rotor azimuth. Only one harmonic is used to attain the required thrust and moments values, hence $i = 1$, and the control parameters $\mathbf{D_{pitch}} = [\theta_0, \theta_{1c}, \theta_{1s}]$ are to be chosen such that the rotor is trimmed, where $\boldsymbol{\theta_0}$ is the collective and $\boldsymbol{\theta_{1c}}, \boldsymbol{\theta_{1s}}$ are the two cyclic pitch parameters. To incorporate rotor pitch actuation in the CFD simulation two additional equations need to be considered:

- a pitch actuation equation

$$\mathbf{S}^{\theta}(\mathbf{x_{s\theta}}, \mathbf{x_s}, \mathbf{D_{pitch}}) = \mathbf{0} \tag{3.7}$$

- an azimuthal mesh rotation equation

$$\mathbf{S}^{\psi}(\mathbf{x}, \mathbf{x_\theta}) = \mathbf{0} \tag{3.8}$$

Evaluation of equation (3.7) pitches the blade and yields a new set of surface grid coordinates $\mathbf{x_{s\theta}}$. Then, to avoid negative-volume cells in the region surrounding the blade, the interior mesh must be deformed. This is accomplished with the mesh deformation algorithm described in Section 3.5 and results in a new set of interior mesh coordinates denoted x_θ. Equation (3.8) is then applied to rotate the entire mesh to the current azimuthal location and results in the final set of grid coordinates $\mathbf{x}$.

3.4 Geometry Parameterization Facility

To perform blade shape optimization, a shape parameterization technique must be implemented. The blade parameterization technique defines the blade surface, and in turn the intial CFD surface mesh coordinates $\mathbf{x_{so}}$, as a function of a set of shape design variables, $\mathbf{D}$. Hence the blade surface mesh points are computed as the solution of a parameterization equation that, in residual form, reads

$$\mathbf{B_{CAD}}(\mathbf{x_{so}}, \mathbf{D}) = \mathbf{0} \tag{3.9}$$

The specific geometry parameterization used in this work is discussed in Chapter 4.

3.5 Mesh Deformation Capability

In order to deform the interior CFD mesh in response to surface displacements a linear elastic analogy mesh deformation approach has been implemented. In this approach, the CFD mesh is modeled as a linear elastic solid with a variable modulus of elasticity that can be prescribed either as inversely proportional to the cell volume or to the distance of each cell from the nearest wall [60,66]. The resulting equations are discretized and solved on the mesh in its original undeformed configuration in response to surface displacements. The governing equations for mesh deformation can be written symbolically as:

$$\mathbf{G}(\mathbf{x}, \mathbf{x_{s\theta}}(\mathbf{D})) = \mathbf{0} \tag{3.10}$$

where $\mathbf{x}$ denotes the interior mesh coordinates and $\mathbf{x_{s\theta}}$ represents the displaced surface mesh coordinates.

3.6 Aeroacoustic Solver: the Three-dimensional FW-H Integration

As done for the two-dimensional blade vortex interaction case in Chapter 2, the acoustic signature of the helicopter rotor is determined with an FW-H acoustic integration. The NSU3D CFD flow solver provides the nearfield flow time history to a newly developed three-dimensional FW-H acoustic integration module that propagates the acoustic pressure at a farfield observer. The location of the FW-H acoustic integration surface depends on the noise problem being investigated. When significant non-linear flow effects are present, as in the case of high-speed helicopter forward flight, an off-body permeable integration surface should be used [14,67] to account for quadrupole noise effects. Noise prediction with an off-body permeable surface is only accurate when the flow field between the body and the integration surface is finely resolved, resulting in a significant increase in the computational cost of the CFD time-integration process. However, quadrupole noise is neglected in this work and an on-body impermeable integration surface is used. Figure 3.2 shows the FW-H acoustic integration surface and the observer location used for validation and optimization purposes. The acoustic surface coincides with the CFD rotor surface mesh and every node on

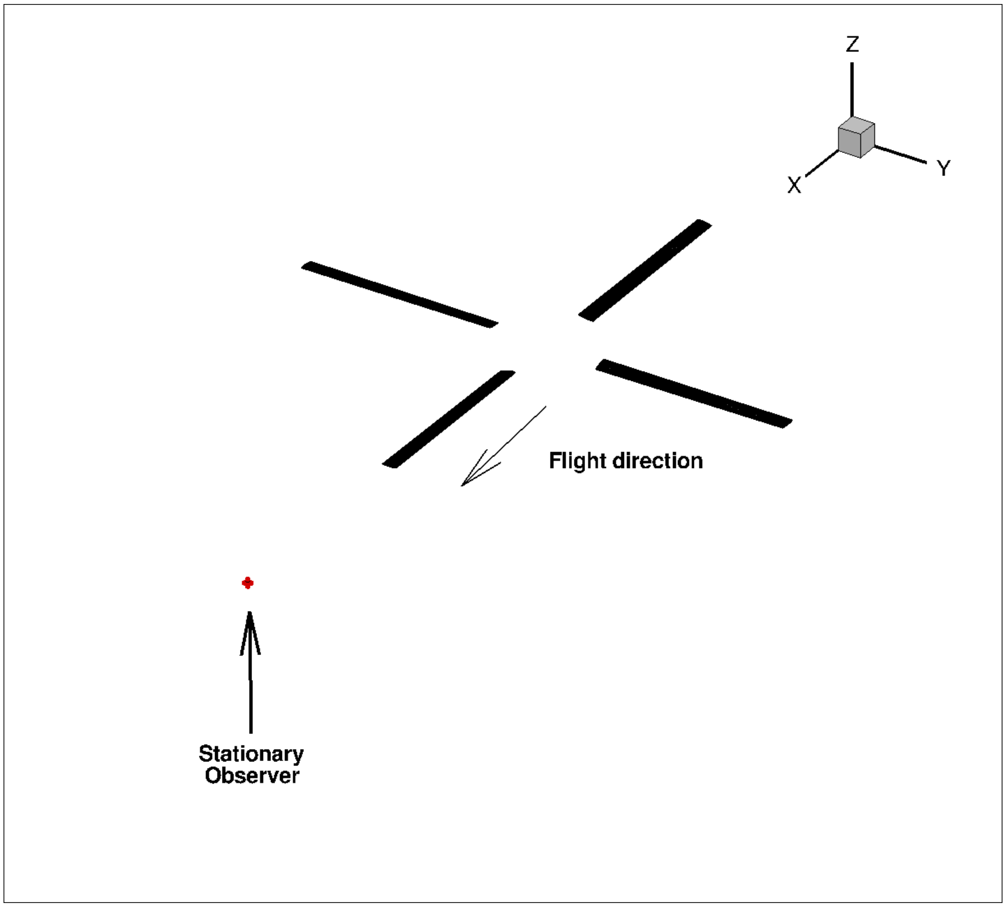

Figure 3.2: Acoustic integration surface and observer location: the observer is stationary in the plane of the rotor two radii from the rotor hub at $\psi = 180$ deg.

the surface is an acoustic source that produces an acoustic pressure at the observer location via the FW-H integration process.

Acoustic Analysis Formulation: the FW-H Integration in the Time Domain

As mentioned in Chapter 2, the acoustic integration in three dimension is typically carried out in the time domain following the derivation from Farassat [13] using the variables

$$\begin{aligned} U_i &= \left(1 - \frac{\rho}{\rho_o}\right) v_i + \frac{\rho u_i}{\rho_o} \\ L_i &= p' n_j + \rho u_i \left(u_n - v_n\right) \end{aligned} \tag{3.11}$$

as proposed by Di Francescantonio [47]. In equation (3.11), $p' = p - p_o$ is the acoustic pressure, n_i is the unit normal of the acoustic surface, $u_n = u_i n_i$ and $v_n = v_i n_i$ are the flow and surface velocities in the direction normal to the integration surface, and for the on-body solid acoustic integration surface used in this work $u = v$. The integral solution is then given, neglecting the quadrupole term, by equation (3.12)

$$\begin{aligned}
4\pi p'_T(\mathbf{y},t) &= \int_{f=0} \left[\frac{\rho_o \left(\dot{U}_n + U_{\dot{n}} \right)}{r(1-M_r)^2} \right]_{ret} dS \\
&+ \int_{f=0} \left[\frac{\rho_o U_n K}{r^2(1-M_r)^3} \right]_{ret} dS \\
4\pi p'_L &= \frac{1}{c_o} \int_{f=0} \left[\frac{\dot{L}_r}{r(1-M_r)^2} \right]_{ret} dS \\
&+ \int_{f=0} \left[\frac{L_r - L_M}{r^2(1-M_r)^2} \right]_{ret} dS \\
&+ \frac{1}{c_o} \int_{f=0} \left[\frac{L_r K}{r^2(1-M_r)^3} \right]_{ret} dS \\
4\pi p'(\mathbf{y},t) &= 4\pi p'_T(\mathbf{y},t) + 4\pi p'_L(\mathbf{y},t)
\end{aligned} \tag{3.12}$$

where $\mathbf{y}$ is the observer location, t is the observer time, r is the distance between the source $\mathbf{x}$ and the observer $\mathbf{y}$ with normalized cartesian components r_i, M is the acoustic source Mach number and

$$\begin{aligned}
U_n &= U_i n_i \\
M_r &= M_i r_i \\
L_r &= L_i r_i \\
L_M &= L_i M_i \\
K = r\dot{M}_r &+ c_o(M_r - M^2)
\end{aligned} \tag{3.13}$$

Equation (3.12) requires the evaluation of the integrals at the emission or retarded time τ: for a given observer location $\mathbf{y}$ and time t the retarded time must be computed via the solution of the nonlinear equation (3.14)

$$\tau = t - r(\mathbf{x}(\tau), \mathbf{y}(t))/c_o \tag{3.14}$$

where $r(\mathbf{x}(\tau), \mathbf{y}(t))$ is the distance between the source $\mathbf{x}$ at the emission time τ and the observer $\mathbf{y}$ at the observer time t. This approach has been followed in most acoustic-analogy-based codes [14].

However, by regarding the source time as the primary time one can choose the source time for an acoustic source and determine when the signal will reach the observer using equation (3.15)

$$t = \tau + r(\mathbf{x}(\tau), \mathbf{y}(t))/c_o \tag{3.15}$$

where τ is again the source time and t is the reception time, i.e. the time at which the acoustic disturbance reaches the observer. Equation (3.15), a rearrangement of equation (3.14), is easier to solve than its retarded time counterpart as the observer motion is usually simpler than the motion of the acoustic integration surface. For each acoustic source a sequence of uniformly spaced source times leads to a sequence of unequally spaced observer times as each source has a different source-to-observer distance, hence the acoustic pressure time history for each source must be interpolated at the desired observer time to determine the final acoustic pressure at the observer location. A comparison of the retarded time and the source-time-dominant algorithm is given in [68].

The source-time-dominant algorithm has been followed in this work since it allows a seamless integration of the acoustic module with the CFD solver. The aerodynamic and aeroacoustic time integration proceed simultaneously and the acoustic surface of integration is the unstructured surface mesh of the rotor. Hence each node of the CFD surface grid corresponds to an acoustic source. The FW-H acoustic integration in the time domain can be summarized as follows:

1. At every CFD timestep and for every acoustic source compute the flow and surface time derivatives $\dot{U}_n$, $U_{\dot{n}}$, $\dot{L}_r$ and $\dot{M}_r$ in equations (3.12) and (3.13) as

   $$\begin{aligned} \dot{U}_n &= \frac{dU_i}{dt} n_i \\ U_{\dot{n}} &= U_i \frac{dn_i}{dt} \\ \dot{L}_r &= \frac{dL_i}{dt} r_i \\ \dot{M}_r &= \frac{dM_i}{dt} r_i \end{aligned}$$

   The time derivatives are based on a BDF2 time discretization with the exception of the source acceleration term $\dot{M}_r$ that is approximated with a second-order-accurate central difference scheme.

2. At every timestep and for every acoustic source assemble the terms in equations (3.11) and (3.13).

3. At every timestep and for every acoustic source evaluate the acoustic integrals in equation (3.12) using a one point Gaussian quadrature to determine the acoustic pressure time history at the observer. In general, the relative distance between the observer and the acoustic source is different for each source, hence a sequence of uniformly spaced source times will result in a sequence of unequally spaced observer reception times for every acoustic source.

4. At the end of the CFD time-integration process build the total acoustic pressure at the observer by linear interpolation of each source acoustic pressure at a sequence of specified observer times.

5. Compute the aeroacoustic objective to be used in the optimizations presented in Chapter 4.

$$L_{FWH} = p'_{RMS} = \sqrt{\frac{\sum_{i=1}^{N_{sample}} p'^2(\mathbf{D})}{N_{sample}}} \tag{3.16}$$

   where N_{sample} is the number of samples in the observer acoustic pressure time history and $\mathbf{D}$ is the vector of design variables.

The current implementation of the FW-H integral equation has been validated against the PSU-WOPWOP [68] acoustic code for the HART-II flexible rotor in trimmed forward flight as shown in Figure 3.3. The rotor has a freestream Mach number of $M = 0.095$ with a tip Mach number of $M_{tip} = 0.638$, a shaft angle $\alpha_{shaft} = 5.4\,\text{deg}$ and a Reynolds Number of 2 million. The corresponding rotor rotational speed is $\Omega = 1041$ RPM (advance ratio $\mu = 0.15$). The CFD simulation has been carried out for two rotor revolutions on a mesh consisting of approximately 2.32 million nodes with a 2-degree timestep, 6 CFD/CSD coupling iterations per time step and a stationary in-plane observer located two radii from the rotor hub at an azimuthal angle $\psi = 180$ deg as shown in Figure 3.2 and described in Table 3.2. Two different observer time windows are shown in Figure 3.3: an extended time window, Figure 3.3(a), and the observer time window targeted during the optimization, Figure 3.3(b). In both cases agreement between the new FW-H implementation and the legacy PSU-WOPWOP code [68] is excellent. The effect that blade flexibility has on the predicted total acoustic pressure is investigated in Figure 3.4: the positive pressure peak is more pronounced in the flexible case while the negative pressure peak is significantly reduced as a consequence of blade deformation. A comparison of the rigid and flexible blades is shown in Figure 3.5 together

Table 3.2: Observer location for the acoustic objective function with respect to the rotor hub, R being the rotor radius

x	**y**	**z**
2R	0	0

with a surface countour plot of the pressure coefficient. All four blades show different deformation characteristics due to the corresponding different aerodynamic environment they experience during trimmed forward flight: the largest flap displacement is attained at $\psi = 180\ deg$ while the smallest happens at $\psi = 0\ deg$.

3.7 Fully Coupled Multidisciplinary Analysis Problem

After introducing each discipline separately, the solvers for aerodynamics, structural mechanics and aeroacoustics will now be linked together to realize the multidisciplinary analysis problem for rotorcraft design.

For a given design geometry, the analysis problem consists of a coupled system of equations that needs to be solved at every timestep. At the beginning of the CFD time-integration process, equation (3.17) defines the new blade shape. At every timestep blade pitch control is applied by explicit evaluation of equation (3.18): the cyclic pitching acts directly on the deflected blade shape coordinates $\mathbf{x_s}$, although these depend on the original undeflected blade surface coordinates $\mathbf{x_{so}}$ and reduce to these values at the beginning of the solution procedure prior to the solution of the structural equations. Next, the combined surface displacements from equations (3.17) and (3.18) are propagated to the interior CFD mesh by iterative solution of the mesh deformation problem in equation (3.19), and the deformed mesh is then rigidly rotated through explicit evaluation of equation (3.20). The fully coupled fluid-structure problem can now be solved by performing multiple coupling iterations on each discipline using the latest available values from the other disciplines. The flow residual equations, equation (3.21), are solved iteratively using the updated grid coordinates $\mathbf{x}$, and the resulting flow variables $\mathbf{u}$ are used to compute the aerodynamic forces that are then

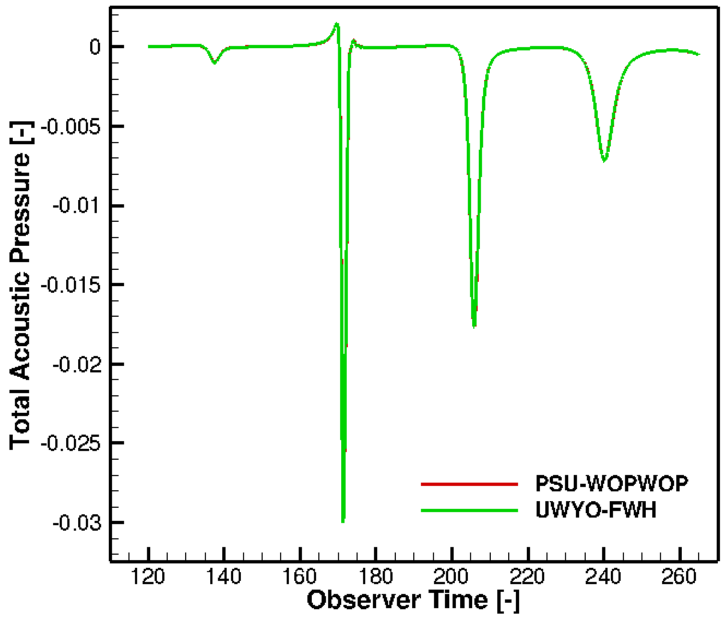

(a) Validation of the current FW-H implementation with the PSU-WOPWOP acoustic code over an extended observer time window.

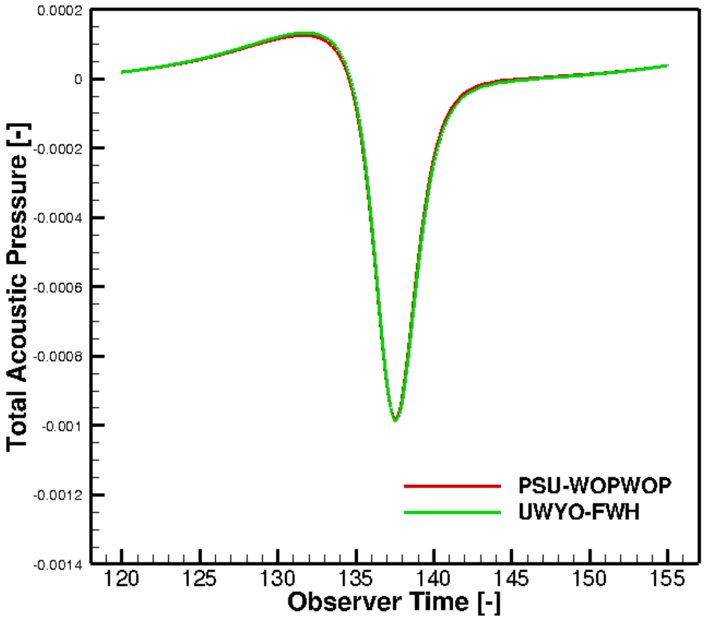

(b) Comparison between the current FW-H implementation and PSU-WOPWOP over the observer time window used for optimization purposes

Figure 3.3: Validation of the current FW-H implementation over an extended (a) and the optimization (b) time window

applied to the structural model through explicit evaluation of the FSI equation (3.22). Using these forces, the structural model in equation (3.23) is solved directly and the resulting displacements are transferred back to the CFD mesh as determined by equation (3.24).

$$\mathbf{B_{CAD}}(\mathbf{x_{so}},\mathbf{D}) = \mathbf{0} \tag{3.17}$$

$$\mathbf{S}^{\theta}(\mathbf{x_{s\theta}},\mathbf{x_s},\mathbf{x_{so}},\mathbf{D}) = \mathbf{0} \tag{3.18}$$

$$\mathbf{G}(\mathbf{x_{\theta}},\mathbf{x_{s\theta}}) = \mathbf{0} \tag{3.19}$$

$$\mathbf{S}^{\psi}(\mathbf{x},\mathbf{x_{\theta}}) = \mathbf{0} \tag{3.20}$$

$$\mathbf{R}(\mathbf{u},\mathbf{x}) = \mathbf{0} \tag{3.21}$$

$$\mathbf{S}(\mathbf{F_b},\mathbf{x},\mathbf{u}) = \mathbf{0} \tag{3.22}$$

$$\mathbf{J}(\mathbf{F_b},\mathbf{Q}) = \mathbf{0} \tag{3.23}$$

$$\mathbf{S}^{'}(\mathbf{x_s},\mathbf{Q}) = \mathbf{0} \tag{3.24}$$

Since the surface mesh coordinates are now modified, the entire process must be repeated until full convergence to machine accuracy is achieved or until a prescribed number of coupling iterations has been reached.

Finally, following an approach similar to that of Dunn and Farassat [69], the aeroelastically converged flow and mesh solutions are used to evaluate the FW-H equation, i.e. to evaluate the acoustic integrals in equation (3.12), for the current CFD source-time. At the end of the CFD time-integration process, the linear interpolation of each source acoustic pressure time history allows for the computation of the total noise signature at the far-field observer as detailed in Section 3.6.

3.8 Fully Coupled Multidisciplinary Tangent and Adjoint Problems

Now that the multidisciplinary analysis problem has been properly formulated, the corresponding tangent and adjoint linearizations can be implemented and verified in order to enable the multidisciplinary adjoint-based optimization of flexible rotors in forward flight. For gradient-based optimization, sensitivities of the objective functional with respect to the design parameters are

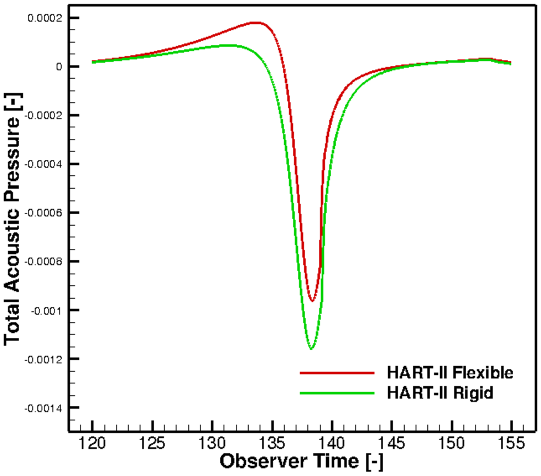

Figure 3.4: Acoustic pressure at the observer for the baseline rigid and flexible HART-II rotor.

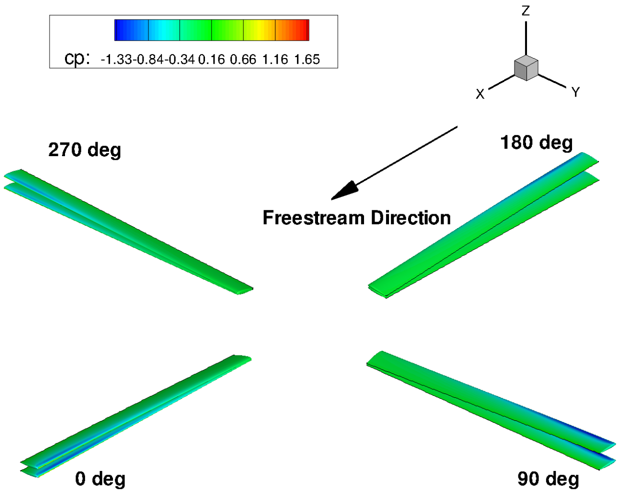

Figure 3.5: Comparison between the rigid and the flexible HART-II rotor.

required. Because of the large-scale nature of the rotor design problem, the number of design variables is large and an adjoint procedure is used to compute these sensitivities in an efficient manner. While a forward or tangent linearization of the analysis problem scales linearly with the number of design variables, the cost of the adjoint or reverse calculation is virtually independent of the number of design parameters. Both tangent and adjoint sensitivity approaches have been implemented in this work by hand differentiation of the flexible aeroacoustic analysis problem. The tangent sensitivity is verified by comparison with the complex-step method [53] while the adjoint linearization is verified using the duality relation [54] to the tangent approach. Upon verification of the adjoint linearization, the adjoint approach is used in all optimizations.

In this thesis only aerodynamic or aeroacoustic objective functionals are considered, and these depend only on the flow and mesh solution, and on the geometric shape. To derive the tangent linearization any objective functional L is expressed as

$$L = L(\mathbf{u}(\mathbf{D}), \mathbf{x}(\mathbf{D})) \tag{3.25}$$

where $\mathbf{u}(\mathbf{D})$ and $\mathbf{x}(\mathbf{D})$ are the aeroelastically converged flow and mesh solution at every time step respectively. Linearization of equation (3.25) with respect to one design variable gives

$$\frac{dL}{d\mathbf{D}} = \begin{bmatrix} \frac{\partial L}{\partial \mathbf{x}} & \frac{\partial L}{\partial \mathbf{u}} \end{bmatrix} \begin{bmatrix} \frac{d\mathbf{x}}{dD} \\ \frac{d\mathbf{u}}{dD} \end{bmatrix} \tag{3.26}$$

where the inner products are intended over all space and time. Differentiation of the system of equations (3.17-3.24) yields the system of equations (3.27) which represent the tangent sensitivity of the fully coupled aeroelastic problem.

$$\begin{bmatrix}
\frac{\partial \mathbf{B_{CAD}}}{\partial \mathbf{x_{so}}} & 0 & 0 & 0 & 0 & 0 & 0 & 0 \\
\frac{\partial \mathbf{S}^{\theta}}{\partial \mathbf{x_{so}}} & \frac{\partial \mathbf{S}^{\theta}}{\partial \mathbf{x}_{\mathbf{s}\theta}} & 0 & 0 & 0 & 0 & 0 & \frac{\partial \mathbf{S}^{\theta}}{\partial \mathbf{x_s}} \\
0 & \frac{\partial \mathbf{G}}{\partial \mathbf{x}_{\mathbf{s}\theta}} & \frac{\partial \mathbf{G}}{\partial \mathbf{x}_{\theta}} & 0 & 0 & 0 & 0 & 0 \\
0 & 0 & \frac{\partial \mathbf{S}^{\psi}}{\partial \mathbf{x}_{\theta}} & \frac{\partial \mathbf{S}^{\psi}}{\partial \mathbf{x}} & 0 & 0 & 0 & 0 \\
0 & 0 & 0 & \frac{\partial \mathbf{R}}{\partial \mathbf{x}} & \frac{\partial \mathbf{R}}{\partial \mathbf{u}} & 0 & 0 & 0 \\
0 & 0 & 0 & \frac{\partial \mathbf{S}}{\partial \mathbf{x}} & \frac{\partial \mathbf{S}}{\partial \mathbf{u}} & \frac{\partial \mathbf{S}}{\partial \mathbf{F_b}} & 0 & 0 \\
0 & 0 & 0 & 0 & 0 & \frac{\partial \mathbf{J}}{\partial \mathbf{F_b}} & \frac{\partial \mathbf{J}}{\partial \mathbf{Q}} & 0 \\
0 & 0 & 0 & 0 & 0 & 0 & \frac{\partial \mathbf{S}'}{\partial \mathbf{Q}} & \frac{\partial \mathbf{S}'}{\partial \mathbf{x_s}}
\end{bmatrix}
\begin{bmatrix}
\frac{d\mathbf{x_{so}}}{d\mathbf{D}} \\
\frac{d\mathbf{x}_{\mathbf{s}\theta}}{d\mathbf{D}} \\
\frac{d\mathbf{x}_{\theta}}{d\mathbf{D}} \\
\frac{d\mathbf{x}}{d\mathbf{D}} \\
\frac{d\mathbf{u}}{d\mathbf{D}} \\
\frac{d\mathbf{F_b}}{d\mathbf{D}} \\
\frac{d\mathbf{Q}}{d\mathbf{D}} \\
\frac{d\mathbf{x_s}}{d\mathbf{D}}
\end{bmatrix}
=
\begin{bmatrix}
-\frac{\partial \mathbf{B_{CAD}}}{\partial \mathbf{D}} \\
-\frac{\partial \mathbf{S}^{\theta}}{\partial \mathbf{D}} \\
0 \\ 0 \\ 0 \\ 0 \\ 0 \\ 0
\end{bmatrix}
\tag{3.27}$$

In equation (3.27), the first equation corresponds to the equation for the surface mesh point sensitivity with respect to the shape design variables, while the second equation rotates this sensitivity through the prescribed pitch angle, and adds the sensitivity with respect to the pitch control inputs. The third equation propagates the surface mesh sensitivity to the interior mesh points through the mesh deformation equations, while the fourth equation corresponds to the azimuthal rotation of this mesh sensitivity. The fifth equation generates the flow sensitivity based on the mesh sensitivity and the solution of the linearized flow problem. The flow sensitivity is then used to construct force sensitivity for the structural model using the tangent linearization of the FSI, which in turn generates the structural sensitivity in the seventh equation. This is passed back to the CFD surface mesh in the last equation, to be reused at the next aeroelastic coupling iteration. The tangent aeroelastic system performs the same number of coupling iterations as the aeroelastic analysis problem. The system in equation (3.27) represents a forward integration in time, the solution of which includes the aeroelastically converged flow and mesh tangent sensitivities $\frac{d\mathbf{u}}{dD}$ and $\frac{d\mathbf{x}}{dD}$ respectively that can be used to compute the objective functional sensitivity in equation (3.26). In the case of an acoustic objective, the flow and mesh tangent sensitivities are passed to the forward linearization of the FW-H equation at every CFD time step to determine the sensitivity of the acoustic objective functional in equation (3.16), following the same approach used in the analysis problem and as detailed in the next section.

The system of equations (3.27) depends on the particular design parameter chosen for the linearization through its right hand side. Hence, every time the design variable D is changed in equation (3.26) the system of equations (3.27) needs to be solved again. This makes the tangent approach infeasible for the large-scale rotorcraft design problems treated in this work.

A more efficient technique to compute the objective sensitivity vector is the adjoint method. In analogy with the derivation of the adjoint problem for the two-dimensional blade-vortex interaction presented in Section 2.5.1, the derivation of the coupled aeroelastic adjoint formulation starts by transposing equation (3.26)

$$\frac{dL}{d\mathbf{D}}^T = \begin{bmatrix} \dfrac{d\mathbf{x}}{d\mathbf{D}}^T & \dfrac{d\mathbf{u}}{d\mathbf{D}}^T \end{bmatrix} \begin{bmatrix} \dfrac{\partial L}{\partial \mathbf{x}}^T \\ \dfrac{\partial L}{\partial \mathbf{u}}^T \end{bmatrix} \tag{3.28}$$

An expression for the unknown sensitivities $\frac{d\mathbf{x}}{d\mathbf{D}}^T$ and $\frac{d\mathbf{u}}{d\mathbf{D}}^T$ is obtained by transposing equation (3.27) that, after substitution in equation (3.28), leads to the definition of the adjoint system

$$
\begin{bmatrix}
\frac{\partial \mathbf{B_{CAD}}}{\partial \mathbf{x_{so}}}^T & \frac{\partial \mathbf{S}^\theta}{\partial \mathbf{x_{so}}}^T & 0 & 0 & 0 & 0 & 0 & 0 \\
0 & \frac{\partial \mathbf{S}^\theta}{\partial \mathbf{x_{s\theta}}}^T & \frac{\partial \mathbf{G}}{\partial \mathbf{x_{s\theta}}}^T & 0 & 0 & 0 & 0 & 0 \\
0 & 0 & \frac{\partial \mathbf{G}}{\partial \mathbf{x_\theta}}^T & \frac{\partial \mathbf{S}^\psi}{\partial \mathbf{x_\theta}}^T & 0 & 0 & 0 & 0 \\
0 & 0 & 0 & \frac{\partial \mathbf{S}^\psi}{\partial \mathbf{x}}^T & \frac{\partial \mathbf{R}}{\partial \mathbf{x}}^T & \frac{\partial \mathbf{S}}{\partial \mathbf{x}}^T & 0 & 0 \\
0 & 0 & 0 & 0 & \frac{\partial \mathbf{R}}{\partial \mathbf{u}}^T & \frac{\partial \mathbf{S}}{\partial \mathbf{u}}^T & 0 & 0 \\
0 & 0 & 0 & 0 & 0 & \frac{\partial \mathbf{S}}{\partial \mathbf{F_b}}^T & \frac{\partial \mathbf{J}}{\partial \mathbf{F_b}}^T & 0 \\
0 & 0 & 0 & 0 & 0 & 0 & \frac{\partial \mathbf{J}}{\partial \mathbf{Q}}^T & \frac{\partial \mathbf{S}'}{\partial \mathbf{Q}}^T \\
0 & \frac{\partial \mathbf{S}^\theta}{\partial \mathbf{x_s}}^T & 0 & 0 & 0 & 0 & 0 & \frac{\partial \mathbf{S}'}{\partial \mathbf{x_s}}^T
\end{bmatrix}
\begin{bmatrix}
\Lambda_{\mathbf{x_{so}}} \\ \Lambda_{\mathbf{x_{s\theta}}} \\ \Lambda_{\mathbf{x_\theta}} \\ \Lambda_{\mathbf{x}} \\ \Lambda_{\mathbf{u}} \\ \Lambda_{\mathbf{F_b}} \\ \Lambda_{\mathbf{Q}} \\ \Lambda_{\mathbf{x_s}}
\end{bmatrix}
=
\begin{bmatrix}
0 \\ 0 \\ 0 \\ \frac{\partial \mathbf{L}}{\partial \mathbf{x}}^T \\ \frac{\partial \mathbf{L}}{\partial \mathbf{u}}^T \\ 0 \\ 0 \\ 0
\end{bmatrix}
\tag{3.29}
$$

Equation (3.29) represents a backward integration in time and at every timestep the adjoint aeroelastic system performs the same number of iterations as the analysis aeroelastic problem. The solution of the backward time integration is then used to compute the sensitivity of the objective function with respect to the full vector of design variables **D**, as shown in equation (3.30)

$$
\frac{dL}{d\mathbf{D}} = \begin{bmatrix} -\frac{\partial \mathbf{B_{cad}}}{\partial \mathbf{D}}^T & -\frac{\partial \mathbf{S}^\theta}{\partial \mathbf{D}}^T & 0 & 0 & 0 & 0 & 0 & 0 \end{bmatrix}
\begin{bmatrix}
\Lambda_{\mathbf{x_{so}}} \\ \Lambda_{\mathbf{x_{s\theta}}} \\ \Lambda_{\mathbf{x_\theta}} \\ \Lambda_{\mathbf{x}} \\ \Lambda_{\mathbf{u}} \\ \Lambda_{\mathbf{F_b}} \\ \Lambda_{\mathbf{Q}} \\ \Lambda_{\mathbf{x_s}}
\end{bmatrix}
\tag{3.30}
$$

The backward time-integration procedure requires the solution of the flexible aeroacoustic problem to be written out to disk at each time step in the analysis run, so that it can be read by the adjoint solver as it proceeds backwards in time.

The right hand side in equation (3.29) depends on the particular objective function L chosen, hence one backward time integration is computed for each objective or constraint for the optimizations discussed in Chapter 4. In the case of the aeroacoustic objective function in equation (3.16), the reverse linearization of the FW-H equation provides the right hand side term in equation (3.29) at every CFD time as detailed in the next section.

Figure 3.6 summarizes the flow of information among all the disciplines for the analysis, tangent, and adjoint solvers. In the analysis problem, the CFD solver sends a force vector to the structural solver and receives a surface displacement vector. At the end of the aeroelastic loop the flow and surface data are passed to the FW-H to determine the acoustic signature. In the tangent problem these quantities are replaced by the corresponding forward sensitivities.

For the adjoint problem, the information proceeds in reverse order with the FW-H sending an acoustic adjoint vector to the adjoint aeroelastic loop. In all cases, these vectors have the same dimension as those used in the analysis problem and make use of the same data structures for inter-disciplinary coupling.

3.8.1 Sensitivity Formulation for the Integral FW-H Equation

Computing the sensitivities of the coupled flexible aeroacoustic problem requires the linearization of the acoustic module with respect to the design variables. The sensitivity formulation for the current implementation of the integral FW-H equation closely mimics the linearization of the CFD code as detailed in references [32, 54]. First the tangent linearization of the acoustic integration has been developed by exact hand-differentiation of the discretized integral FW-H equation. The tangent linearization has then been transposed and applied in reverse order to obtain the adjoint sensitivity with respect to the full vector of design variables. The derivation of the tangent and adjoint sensitivities for the three dimensional acoustic integration closely follows the two-dimensional derivation presented in Section 2.5.2: the main differences between the two derivations follow from the time-domain formulation of the three-dimensional acoustic integration and

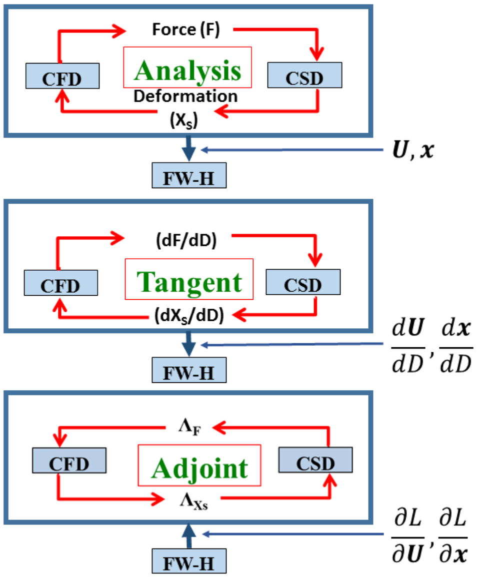

Figure 3.6: Flow of information for analysis, tangent and adjoint solution processes at every timestep.

the corresponding coupling strategy to the CFD code.

Tangent Sensitivity Formulation

The tangent linearization of the acoustic objective function allows the computation of the objective function sensitivity with respect to a single design variable. The acoustic pressure at the observer location and time is defined as

$$p'(\mathbf{y}, t, \mathbf{D}) = \mathbf{FWH}(\mathbf{u}(\mathbf{D}), \mathbf{x}(\mathbf{D})) \tag{3.31}$$

where $\mathbf{D}$ is the vector of design variables and $\mathbf{FWH}(\mathbf{u}(\mathbf{D}), \mathbf{x}(\mathbf{D}))$ represents all the discrete operations necessary to evaluate equation (3.12) numerically, as outlined in the algorithm from Section 3.6. In this expression $\mathbf{u}(\mathbf{D})$ and $\mathbf{x}(\mathbf{D})$ are the flow and mesh solution at every time step of the time-integration process at the acoustic integration surface, after the aeroelastic coupling has converged. The acoustic pressure tangent sensitivity time history can be expressed as

$$\frac{dp'(\mathbf{y}, t, \mathbf{D})}{dD} = \frac{\partial \mathbf{FWH}}{\partial \mathbf{u}_{\mathbf{FWH}}} \frac{d\mathbf{u}_{\mathbf{FWH}}}{dD} + \frac{\partial \mathbf{FWH}}{\partial \mathbf{x}_{\mathbf{FWH}}} \frac{d\mathbf{x}_{\mathbf{FWH}}}{dD} \tag{3.32}$$

so that the tangent linearization of the acoustic objective function p'_{RMS} defined in equation (3.16) becomes:

$$\begin{aligned} \frac{dL_{FWH}}{dD} &= \frac{\partial L_{FWH}}{\partial \mathbf{u_{FWH}}}\frac{d\mathbf{u_{FWH}}}{dD} + \frac{\partial L_{FWH}}{\partial \mathbf{x_{FWH}}}\frac{d\mathbf{x_{FWH}}}{dD} \\ &= \frac{\partial p'_{RMS}}{\partial p'}\frac{dp'}{dD} \\ &= \frac{\partial p'_{RMS}}{\partial p'}\left[\frac{\partial \mathbf{FWH}}{\partial \mathbf{u_{FWH}}}\frac{d\mathbf{u_{FWH}}}{dD} + \frac{\partial \mathbf{FWH}}{\partial \mathbf{x_{FWH}}}\frac{d\mathbf{x_{FWH}}}{dD}\right] \end{aligned} \tag{3.33}$$

In equation (3.33) the terms $\frac{d\mathbf{u_{FWH}}}{dD}$ and $\frac{d\mathbf{x_{FWH}}}{dD}$ are the aeroelastically-converged flow and mesh tangent sensitivities at every time step evaluated at the acoustic integration surface that are computed via the forward time integration described by equation (3.27). The terms $\frac{\partial \mathbf{FWH}}{\partial \mathbf{u_{FWH}}}$ and $\frac{\partial \mathbf{FWH}}{\partial \mathbf{x_{FWH}}}$ are the tangent linearizations of equation (3.12). The tangent acoustic problem proceeds by analogy with the acoustic analysis problem. The tangent flow solution and the tangent acoustic solution are carried out simultaneously: the aeroelastically-converged tangent flow solution is used to assemble the tangent sensitivities of all the terms in equation (3.13) which in turn are used to evaluate the tangent sensitivity of the integral equation (3.12) at every timestep, resulting in an unequally spaced acoustic pressure sensitivity at the observer location for every acoustic source. The final observer acoustic pressure sensitivity time history is built via linearization of the time interpolation algorithm at the end of the time-integration process allowing for the computation of the acoustic objective function sensitivity, equation (3.33), with respect to one design variable.

Adjoint Sensitivity Formulation

The adjoint sensitivity can be derived by transposing the tangent sensitivity formulation. Transposing equation (3.33) yields

$$\begin{aligned} \frac{dL_{FWH}}{dD}^T &= \left[\frac{d\mathbf{u_{FWH}}}{dD}^T\frac{\partial FWH}{\partial \mathbf{u_{FWH}}}^T + \frac{d\mathbf{x_{FWH}}}{dD}^T\frac{\partial FWH}{\partial \mathbf{x_{FWH}}}^T\right]\frac{\partial p'_{RMS}}{\partial p}^T \\ &= \frac{d\mathbf{u}}{\partial D}^T\frac{\partial L_{FWH}}{\partial \mathbf{u}}^T + \frac{d\mathbf{x}}{\partial D}^T\frac{\partial L_{FWH}}{\partial \mathbf{x}}^T \end{aligned} \tag{3.34}$$

The terms $\frac{\partial L_{FWH}}{\partial \mathbf{u}}^T = \frac{\partial FWH}{\partial \mathbf{u_{FWH}}}^T\frac{\partial p'_{RMS}}{\partial p}^T$ and $\frac{\partial L_{FWH}}{\partial \mathbf{x}}^T = \frac{\partial FWH}{\partial \mathbf{x_{FWH}}}^T\frac{\partial p'_{RMS}}{\partial p}^T$ represent the right-hand-side of equation (3.29) for the case of the acoustic objective function and drive the adjoint backward time-integration described in equation (3.29). The term $\frac{\partial p'_{RMS}}{\partial p}^T$ is the reverse linearization of the observer time interpolation process that needs to be evaluated before the adjoint time-integration can start while the term $\frac{\partial FWH}{\partial \mathbf{u_{FWH}}}^T$ and $\frac{\partial FWH}{\partial \mathbf{x_{FWH}}}^T$ correspond to the reverse linearization of the acoustic integrals in equation (3.12). At the end of the backward time-integration process, the full sensitivity vector of the acoustic objective function is recovered.

Verification of the Flexible Aeroacoustic Sensitivities

The coupled adjoint flexible aeroacoustic sensitivity to be used by the gradient based optimization algorithm is verified with the complex step differentiation method [53], that has been described in Section 2.5.1. As a consequnce of the time-domain implementation of the three-dimensional acoustic integration, and contrary to the two-dimensional case that employed complex variables in the acoustic formulation, the complex-step method can be used to verify the tangent and adjoint sensitivities of the multidisciplinary flexible aeroacoustic problem. By using a step size of $h = 10^{-31}$ the tangent formulation has been verified to machine accuracy.

For the verification study, two revolutions of the HART-II flexible rotor are simulated on a mesh consisting of approximately 107,000 nodes using a 4-degree timestep. The acoustic integration is performed only over the last revolution targeting the same observer time window as in Figure 3.3(b) and the sensitivity is computed with respect to the twist of the root section and to the first cyclic pitch parameter. Figure 3.7 shows excellent agreement between the tangent acoustic pressure sensitivity time history, equation (3.32), and its complex counterpart. Further verification of the acoustic objective function sensitivity in equation (3.33) is shown in Table 3.3 for the root twist design variable and in Table 3.4 for the first cyclic pitch parameter. The tangent sensitivity allows for the verification of the adjoint sensitivity by the duality relation [54]. The current aeroacoustic adjoint implementation is verified by comparing the adjoint sensitivity to the unsteady forward and complex step sensitivities with respect to the twist of the root section, in Table 3.3, and to the first cyclic pitch parameter, in Table 3.4. The coupled flow and structural equations are converged to machine precision at each time step to avoid any algebraic error, and the complex, tangent and adjoint sensitivities are seen to agree to 9 significant figures. The adjoint sensitivities can then be used in the gradient based optimization process.

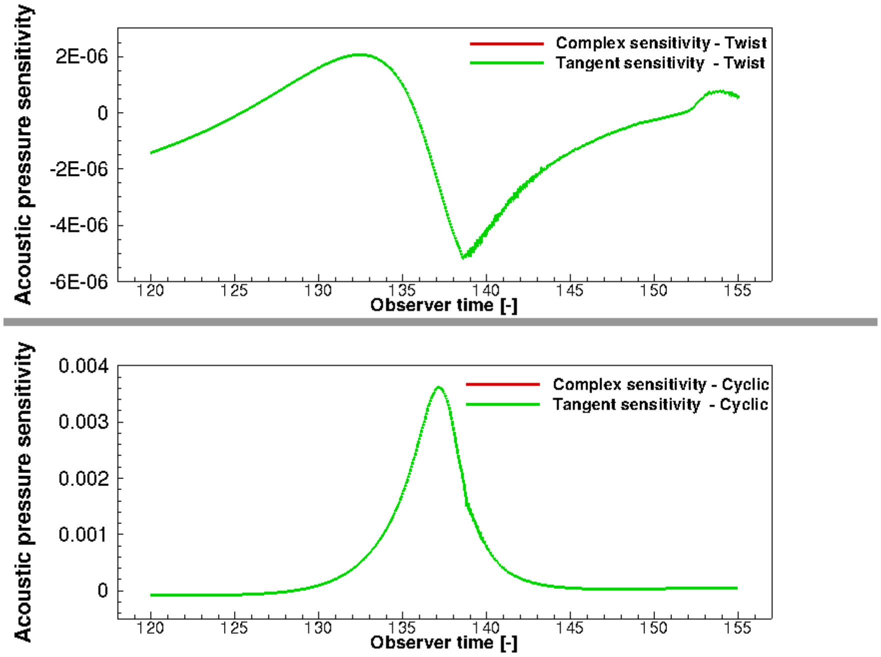

Figure 3.7: Complex step verification of the tangent acoustic pressure time history sensitivity

Table 3.3: Adjoint sensitivity verification for the $p^{'}_{RMS}$ objective function w.r.t. the root twist design variable.

Complex	1.46204808**801E-06**
Tangent	1.4620480**608E-06**
Adjoint	1.46204808**794E-06**

Table 3.4: Adjoint sensitivity verification for the $p^{'}_{RMS}$ objective function w.r.t. the first cyclic design variable.

Complex	-4.269878110**954E-04**
Tangent	-4.269878110**962E-04**
Adjoint	-4.269878110**854E-04**

Chapter 4

Optimization Results

This chapter presents optimization results for both the two-dimensional and the three-dimensional aeroacoustic adjoint capabilities presented in this thesis. In both cases gradient-based optimization algorithms are used to minimize noise under a constraint on the aerodynamic performance of the geometry considered in the application. The gradients needed by the optimization algorithms are computed with the newly developed aeroacoustic adjoints.

Two dimensional results are presented first. In this case, a comparison between a constrained and an unconstrained optimization method highlights the superior performance of the constrained optimization approach. Three dimensional optimization results are presented next. Optimization results for the rigid HART-II rotor are presented first. The effect of blade flexibility is then introduced in the aeroacoustic optimization process to realize a multidisciplinary optimization capability that encompasses the three disciplines of aerodynamics, structural mechanics and aeroacoustics.

4.1 Two-dimensional Optimization Results

The goal of the following optimizations is to reduce the noise signature of the BVI noise case described in Chapter 2 without suffering significant aerodynamic penalties. In the three-dimensional framework, such as that presented in Section 4.2, the optimization goal would be to minimize the observer noise under the condition that the helicopter rotor is trimmed. In the present two-dimensional framework the trim condition is replaced by requiring that the optimized airfoil time-integrated lift is constrained to that of the baseline NACA-0012 airfoil, hence the aerodynamic constraint for the present two-dimensional optimization is expressed as shown in equation (4.1)

$$L_{AERO} = \frac{\sum_{n=1}^{Ntsteps} \left(C_L^n - C_{L_{baseline}}^n \right)^2}{N_{tsteps}} \tag{4.1}$$

In equation (4.1) $C_{L_{baseline}}$ is the lift time history of the baseline NACA 0012 airfoil and C_L is the lift time history for the current design iteration. The Overall Sound Pressure Level defined in equation (2.51) has been chosen as a measure of the noise signature at the observer and the acoustic objective function is defined as in equation (4.2)

$$L_{FWH} = \frac{OSPL_{@x=0.5,y=-50}}{OSPL_{baseline}} \tag{4.2}$$

where $OSPL_{baseline} = 87.1dB$ is the OSPL of the baseline NACA - 0012 airfoil at the observer location used for the two-dimensional optimization. Two different optimization algorithms have been used for this optimization problem: the L-BFGS-B quasi-Newton method from Zhu [70] and the sequential quadratic programming (SQP) algorithm implemented in SciPy [71]. The two algorithms differ in that the L-BFGS-B is an unconstrained optimization algorithm while the SQP algorithm can handle linear and nonlinear, equality and inequality constraints. Since the L-BFGS-B algorithm does not handle constraint explicitly a penalty function formulation must be employed [22] to take into account the aerodynamic constraint. In a penalty function formulation the objective and the constraint are combined into one objective function to be minimized. The algorithm then tries to find a set of design variables for which the gradient of the combined objective function is zero. For this reason only the gradients of the combined objective function are needed to drive the optimization, hence only the adjoint of the combined objective function needs to be computed. For the current two-dimensional optimization the objective function is defined in equation (4.3).

The SQP algorithm handles constraints explicitly by finding the set of design variables that satisfies the Karush-Kuhn-Tucker optimality condition [22, 72]. However, this requires the solution of multiple adjoints, one for the objective and one for each constraint in the problem. For the two-dimensional aeroacoustic application the constrained optimization problem is defined in equation (4.4).

4.1.1 L-BFGS-B Optimization

The objective function for the L-BFGS-B optimization algorithm is

$$L^g = \omega L_{FWH} + (1-\omega)L_{AERO} \tag{4.3}$$

where the aerodynamic and acoustic objectives have been defined in equation (4.1) and (4.2) respectively. The parameter ω varies between zero and one and enforces the aerodynamic constraint as a penalty term. For $\omega = 1$ there is no aerodynamic penalty, while the case $\omega = 0$ corresponds to a pure aerodynamic optimization. Only two values of ω have been used: the value $\omega = 1$ has been used to perform the unpenalized optimization of the aeroacoustic objective function in order to asses the maximum noise signature reduction achievable regardless of the aerodynamic performance of the airfoil. The value $\omega = 0.1$ has been used to find an airfoil with reduced noise signature and untarnished aerodynamic performance. For this optimization one design cycle corresponds to one unsteady flow solution and one unsteady adjoint solution.

Figure 4.1 shows the baseline, the acoustically optimized ($\omega = 1$) and the aerodynamically penalized ($\omega = 0.1$) airfoils. For the $\omega = 1$ case the optimizer reduces the lower surface thickness and increases the upper surface thickness of the airfoil. The effect of the aerodynamic penalty term is evident in the shape for the $\omega = 0.1$ optimization where an almost symmetric shape is recovered although the chordwise thickness distribution of the optimized airfoil is significantly different from that of the baseline NACA-0012. The lift time histories for the two optimizations and for the baseline airfoil are shown in Figure 4.2 where it is evident how the aerodynamically penalized optimization tries to recover the baseline lift time history. Convergence of the optimization for the $\omega = 0.1$ case is shown in Figure 4.3. The objective function reaches a plateau already after 10 iterations while the gradient magnitude is reduced more than one order of magnitude, suggesting that an optimum has in fact been reached. In terms of noise signature the unconstrained optimization ($\omega = 1$) has an OSPL $3dB$ lower than the baseline airfoil, while the aerodynamically penalized optimization ($\omega = 0.1$) reduces the baseline OSPL by approximately $1dB$, as shown in Table 4.1.

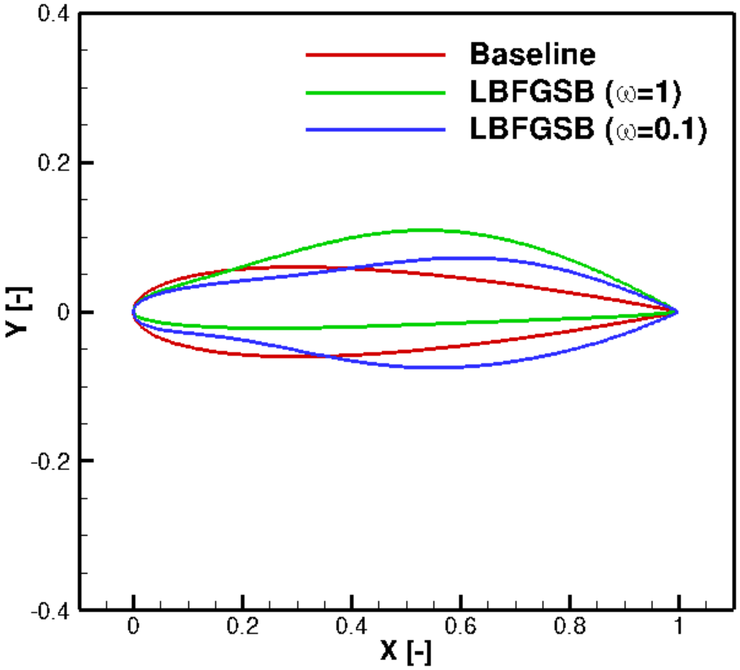

Figure 4.1: Baseline, acoustically optimized ($\omega = 1$) and aeroacoustically optimized ($\omega = 0.1$) airfoils

Table 4.1: Overall Sound Pressure Level (OSPL) values for different weights ω.

	SPL [dB]
Baseline	87.1
$\omega = 0.1$	86.3
$\omega = 1.0$	84.8
SQP	86.5

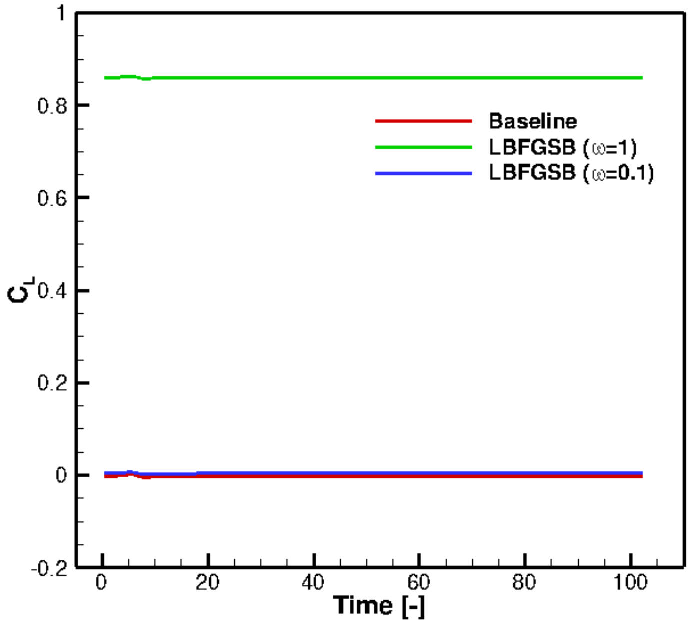

(a) Lift time histories for the baseline, the acoustically optimized ($\omega = 1$) and the aeroacoustically optimized ($\omega = 0.1$) airfoils

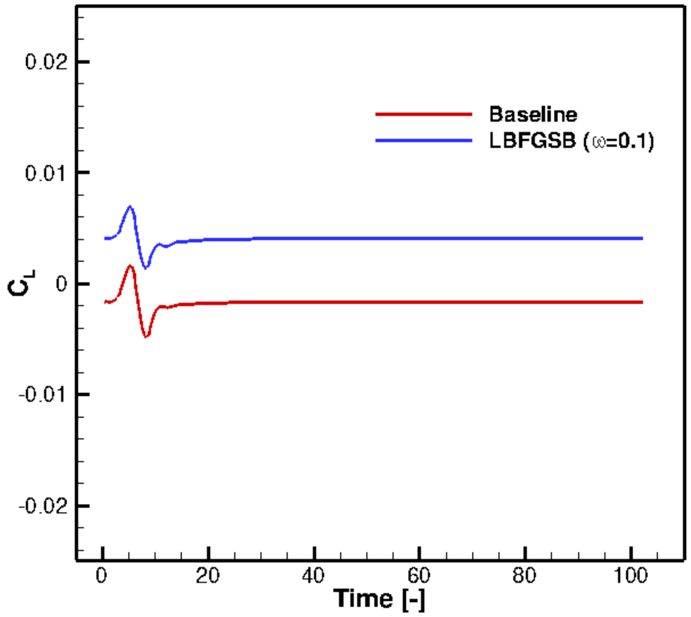

(b) Detail of the lift time histories for the baseline and the aeroacoustically optimized ($\omega = 0.1$) airfoils

Figure 4.2: Lift time histories for the baseline and the optimized airfoil highlithing the importance of the aerodynamic penalty term

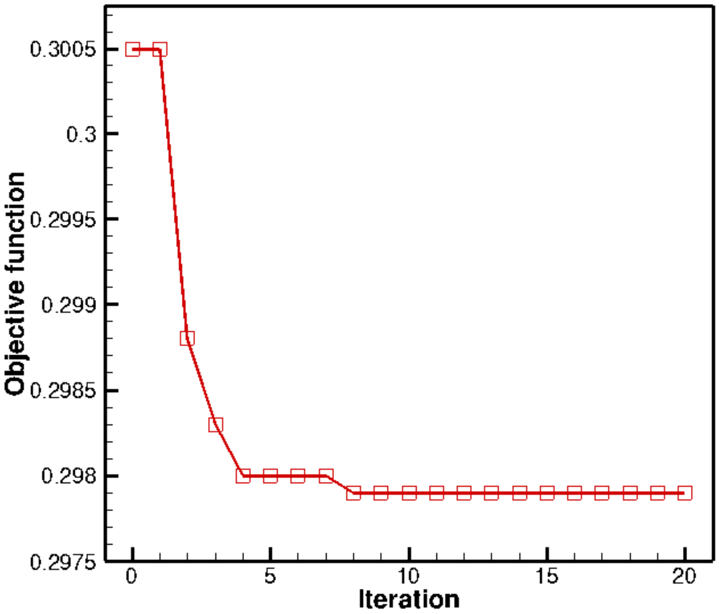

(a) Objective as function of the number of iterations

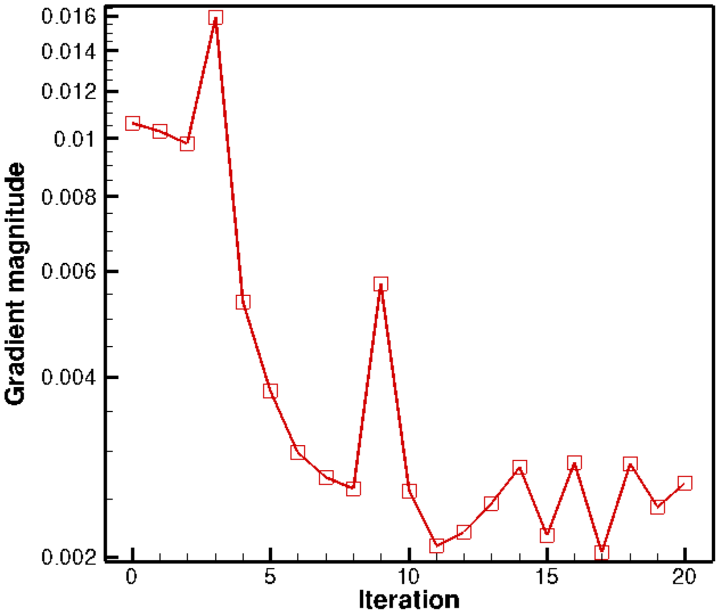

(b) Gradient magnitude as function of the number of iterations

Figure 4.3: Convergence of the L-BFGS-B $\omega = 0.1$ optimization

4.1.2 Sequential Quadratic Programming Optimization

The optimization problem for the SQP optimization can be formulated as in equation (4.4)

$$\begin{aligned} \text{Minimize } & L_{FWH} \\ \text{Subject to } & \\ L_{AERO} &= 0 \\ w.r.t. & \; \mathbf{D} \end{aligned} \tag{4.4}$$

where now the aerodynamic constraint is strongly enforced and this requires the solution of an additional adjoint problem for the constraint. Hence, one design cycle for this optimization corresponds to one unsteady flow solution and two unsteady adjoint solutions, one for the aeroacoustic objective and one for the aerodynamic constraint. The SQP optimized airfoil shape is shown in Figure 4.4 together with the penalized L-BFGS-B and the baseline airfoil. The overall sound pressure level for the SQP optimized airfoil is $86.5dB$ which is comparable to the penalized L-BFGS-B OSPL value reported in Table 4.1. However, despite an almost identical optimized OSPL value the two airfoil shapes differ significantly, with the SQP airfoil that considerably departs from the almost symmetric shape of the penalized L-BFGS-B airfoil. This is a consequence of the direct enforcement of the aerodynamic constraint, as shown in Figure 4.5 where the lift time histories of the two optimizations are compared to that from the baseline NACA-0012 airfoil. The convergence behaviour of the SQP optimization is shown in Figure 4.6. The objective function reaches a minimum after approximately 30 iterations compared to the 10 iterations from the L-BFGS-B algorithm.

4.2 Three-Dimensional Optimization Results

The three-dimensional aeroacoustic optimizations of the rigid and flexible HART-II rotors are presented next. The optimization of the rigid rotor is presented first, followed by the optimization of the flexible rotor to realize the multidisciplinary adjoint based optimization capability that represents the unique aspect of this thesis.

In both the rigid and flexible case the HART-II rotor is first trimmed according to equation (4.5) to

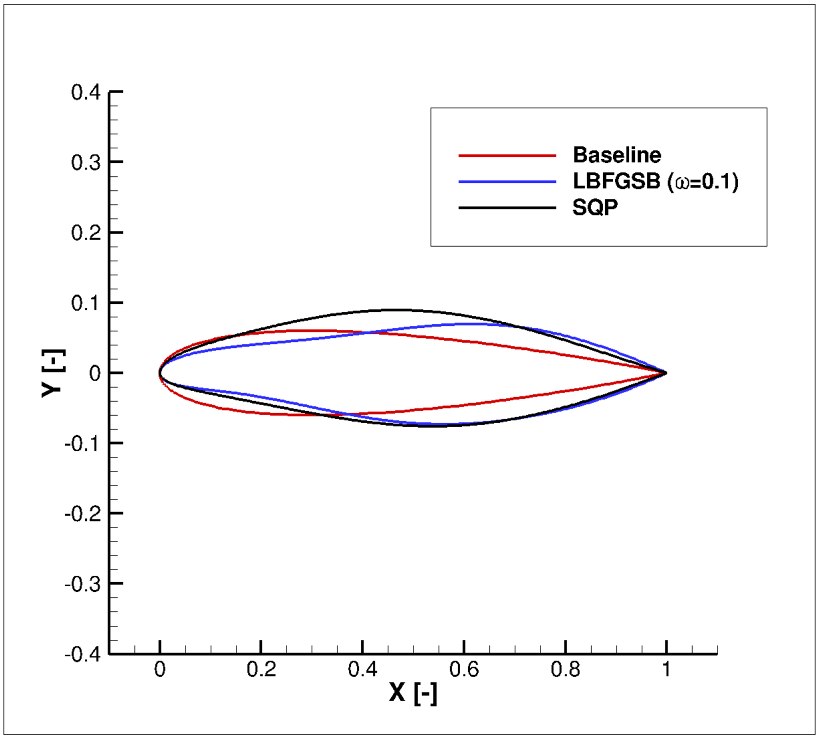

Figure 4.4: Baseline, L-BFGSB-B ($\omega = 0.1$) and SQP optimized airfoils.

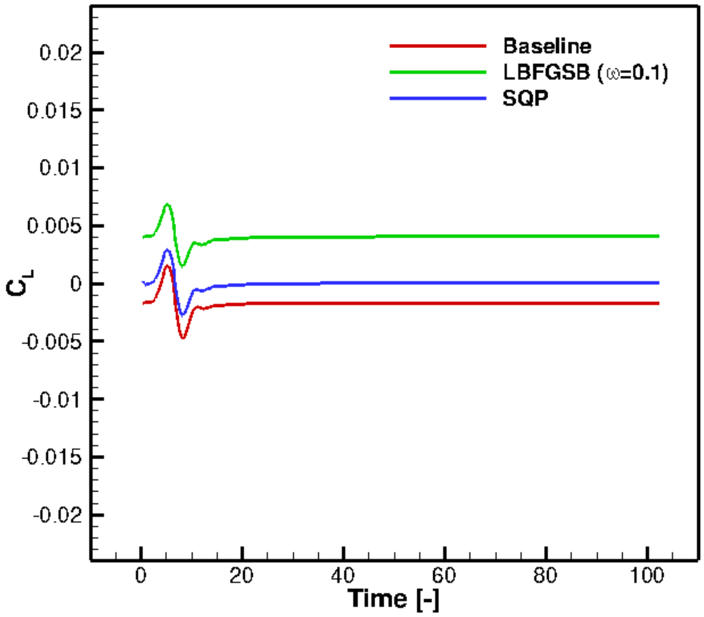

Figure 4.5: Baseline, L-BFGSB-B ($\omega = 0.1$) and SQP lift time histories.

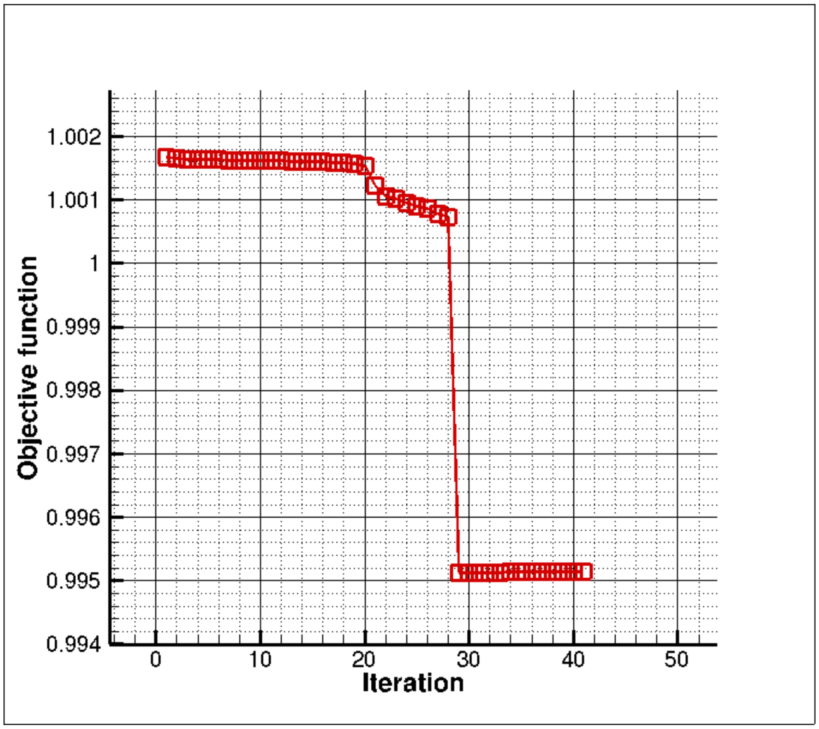

(a) Objective as function of the number of iterations

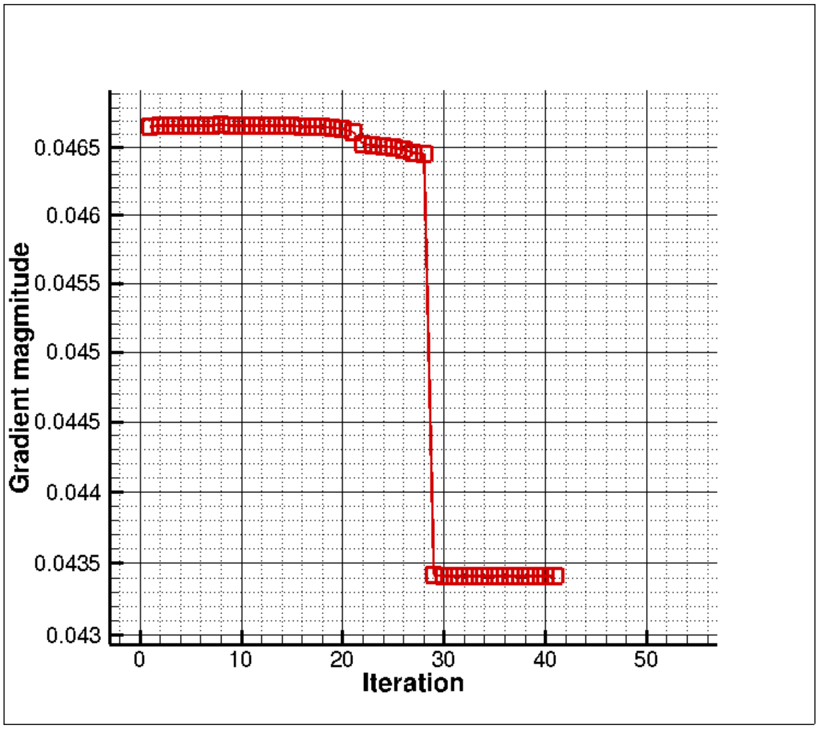

(b) Gradient magnitude as function of the number of iterations

Figure 4.6: Convergence of the Sequential Quadratic Programming optimization for the NACA 0012 airfoil

establish the baseline noise signature and torque level.

$$\begin{aligned} &min\ L_{THRUST} \\ &\texttt{subject to} \\ &L_{LATERAL} = 0 \\ &w.r.t.\ \mathbf{D_{pitch}} \end{aligned} \tag{4.5}$$

where the vector of design variables $\mathbf{D_{pitch}}$ includes only pitch control parameters and has been described in Section 3.3. Then, an aeroacoustic optimization aims at reducing the rotor's noise signature under a trim constraint as shown in equation (4.6).

$$\begin{aligned} &min\ p'_{RMS} \\ &\texttt{subject to} \\ &L_{THRUST} = 0 \\ &L_{LATERAL} = 0 \\ &w.r.t.\ \mathbf{D} \end{aligned} \tag{4.6}$$

and the vector of design variables $\mathbf{D}$ now consists of both shape and pitch design variables. The noise signature of the resulting optimal rotor provides a limit of the achievable noise reduction, but it comes at the expense of the rotor's performance, highlighting the need to include rotor torque in the optimization process: for the rigid rotor the acoustic signature is minimized under a torque constraint as detailed in equation (4.7)

$$\begin{aligned} &min\ p'_{RMS} \\ &\texttt{subject to} \\ &L_{THRUST} = 0 \\ &L_{LATERAL} = 0 \\ &L_{TORQUE} < L_{TORQUE_{BASE}} \\ &w.r.t.\ \mathbf{D} \end{aligned} \tag{4.7}$$

For the flexible rotor, a torque minimization under an acoustic constraint will be performed according to equation (4.8) and the value $p'_{RMS_{TARGET}}$ has been chosen to guarantee a 2dB OSPL noise signature reduction of the baseline rotor.

$$\begin{aligned} min\ L_{TORQUE} \\ \texttt{subject to} \\ L_{THRUST} = 0 \\ L_{LATERAL} = 0 \\ p'_{RMS} = p'_{RMS_{TARGET}} \\ w.r.t.\ \mathbf{D} \end{aligned} \tag{4.8}$$

The aerodynamic functionals L_{THRUST}, $L_{LATERAL}$ and L_{TORQUE} measure the aerodynamic performance averaged over one rotor revolution and are defined as

$$\begin{aligned} L_{THRUST} &= \frac{1}{N}\left(\sum_{i=1}^{N}\left(C_T^i - C^i_{T_{AVERAGE}}\right)\right)^2 \\ L_{LATERAL} &= \frac{1}{N}\left[\left(\sum_{i=1}^{N} C^i_{M_x}\right)^2 + \left(\sum_{i=1}^{N} C^i_{M_y}\right)^2\right] \\ L_{TORQUE} &= \frac{1}{N}\sum_{i=1}^{N}\left(C_Q^i\right)^2 \end{aligned} \tag{4.9}$$

In equation (4.9) C_T, C_Q, C_{M_x} and C_{M_y} are the rotor's thrust, torque, pitching and rolling moments coefficients respectively [1], while $C^i_{T_{AVERAGE}} = 0.0044$ is the target thrust coefficient for the baseline HART-II rotor and N is the number of time step in a rotor revolution. The aeroacoustic functional is the root mean square of the acoustic pressure as computed by the FW-H acoustic integration and is defined in equation (3.16).

One design cycle for the trim optimization in equation (4.5) corresponds to one unsteady flow solution and two unsteady adjoint solutions. For the acoustic optimization in equation (4.6) one design cycle corresponds to one unsteady flow solution and three time-dependent adjoint integrations, one for the acoustic objective and two for the trim constraints. Finally one design cycle for the optimizations in equations (4.7) or (4.8) corresponds to one unsteady flow solution and four unsteady adjoint solutions, one for the objective and three for the constraints. For the case of the rigid rotor one unsteady flow solution takes approximately one hour of wall-clock time on 1024 cores with each unsteady adjoint integration costing approximately the same as one flow solution. For the

Table 4.2: Operating condition for the HART-II rotor in trimmed forward flight

Freestream Mach number (velocity)	$M_\infty = 0.095$ (64 kt)
Tip Mach Number	$M_{tip} = 0.638$
Advance ratio	$\mu = 0.15$
Rotational speed	$\Omega = 1041\ RPM$
Shaft angle	$\alpha_{shaft} = 5.4\,\mathrm{deg}$

flexible rotor one unsteady flow solution takes approximately 90 minutes of wall-clock time on 1024 cores with each unsteady adjoint solution costing approximately 45 minutes of wall clock time. Approximately 650 Gbytes of data are stored to disk during the analysis problem and read in by the flexible aeroacoustic adjoint procedure. The computational cost of any of the optimizations in equations (4.6), (4.7) or (4.8) is approaximately 96 hours of wall-clock time on 1024 cores on the Yellowstone supercomputer at the NCAR-Wyoming Supercomputing Center (NWSC).

The flow conditions for the HART-II rotor are described in Table 4.2 and the simulations are run for two rotor revolutions using a 2 degree timestep and a computational mesh that consists of approximately 2.32 million nodes. The aerodynamic functionals in equation (4.9) are accumulated only over the second revolution to prevent the optimization algorithm from focusing on the initial transient. The acoustic integration is performed only over the second revolution and the acoustic objective function is evaluated over the observer time window shown in Figure 3.3(b). For all optimizations the observer is stationary and is placed in front of the rotor as shown in Figure 3.2 and detailed in Table 3.2.

Only shape design variables that affect the outer mold line of the CFD geometry are considered here. The baseline blade is constructed by stacking 9 airfoils along the span. Each airfoil is parameterized with 10 Hicks-Henne bump functions [73], 5 for the upper surface and 5 for the lower surface respectively. Blade twist varies linearly between root and tip, while one collective and two cyclics allow the trimming of the rotor, for a total of 95 design variables in the vector of design variables **D** in equation (4.6), (4.7) and (4.8). For the flexible optimizations no structural design variables are considered and the optimization design variables affect the aeroelastic loop only through changes in the aerodynamic forces applied to the structural model.

All the optimizations are driven by the SNOPT sequential quadratic programming algorithm [72] using the unsteady aeroacoustic adjoint capability developed in this work. Convergence results for the optimization problems are given as a function of nonlinear optimization iterations and of design cycles. While the number of design cycles is a measure of the optimization wall-clock time, the number of nonlinear iterations is the number of iterations used by SNOPT to solve the optimization problem; convergence of the optimization is assessed through feasibility, which is a measure of the constraint violation, and optimality, which is a measure of the satisfaction of the Karush - Kuhn - Tucker condition as described in [72].

4.2.1 Rigid HART-II Rotor

Trim Results

The trim optimization problem is described by equation (4.5). The optimization convergence is shown in Figure 4.7. After 9 nonlinear iterations and 17 design cycles the feasibility and optimality of the optimization problem are reduced by more than 2 orders of magnitude and the baseline HART-II rotor is trimmed as further confirmed by thrust and lateral moments time histories shown in Figure 4.8.

The trimmed HART-II rotor will now serve as the initial design for all subsequent aeroacoustic optimizations for the rigid rotor.

Aeroacoustic Optimization

As mentioned above the initial design is the trimmed HART-II rotor from the previous section and the optimization problem is described in equation (4.6). SNOPT convergence is shown in terms of nonlinear optimization iterations and design cycles in Figure 4.9. After 17 design cycles the optimization produces a geometry that reduces the Overall Sound Pressure Level of 3.4 dB while keeping the rotor trimmed as highlighted by the thrust and lateral moments time histories shown in Figure 4.10. Thickness, loading and total acoustic pressure time histories are shown in Figure 4.11. Noise minimization is achieved with rather thick airfoils especially at the inboard sections, as shown in Figure 4.12, while twist and pitch control variables are shown in Table 4.3.

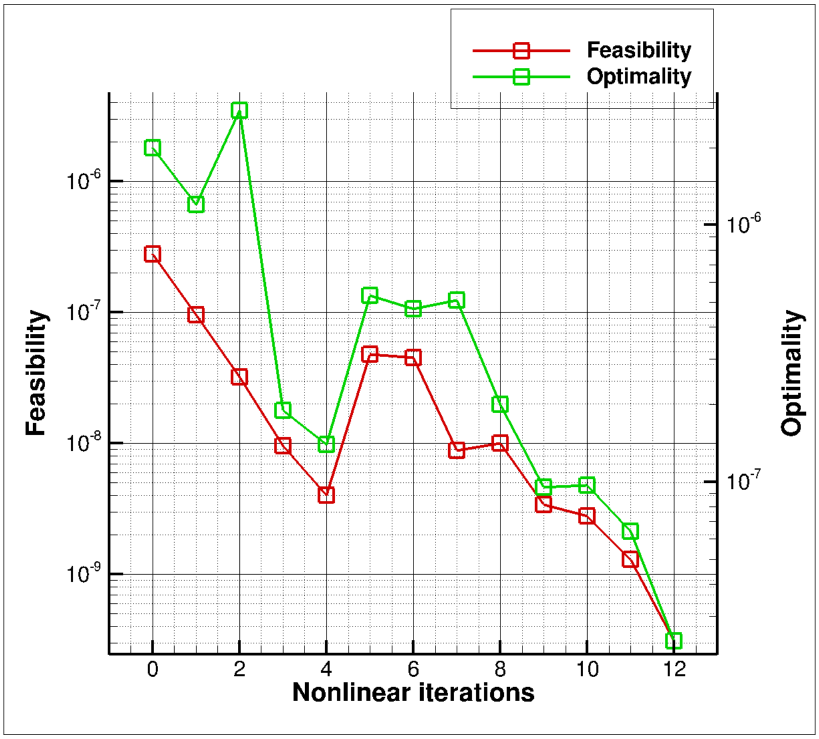

(a) Feasibility and optimality of the rigid trim optimization problem as a function of nonlinear optimization iterations

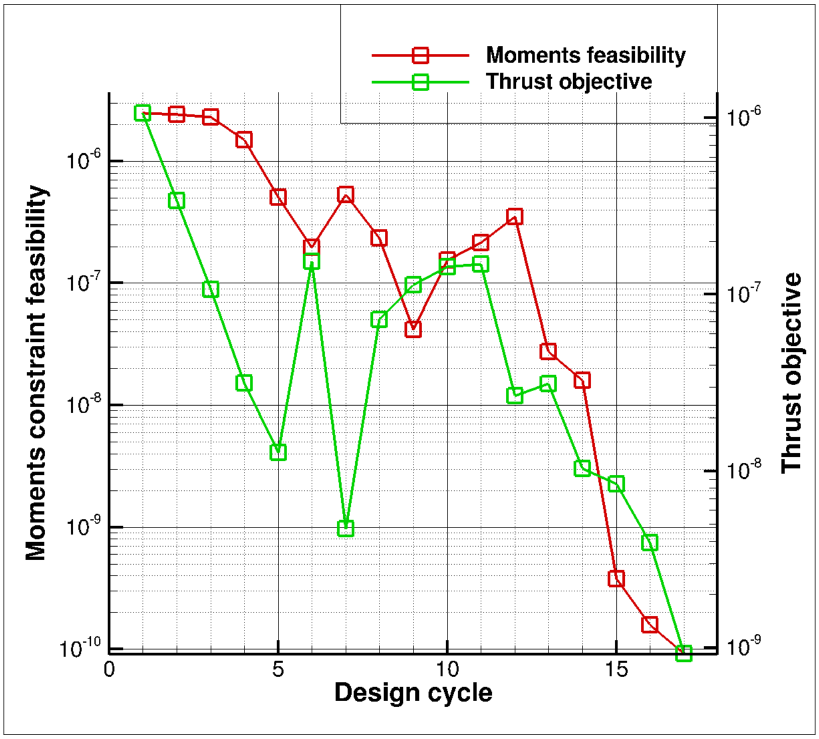

(b) Convergence of the thrust objective function and moment constraint as a function of design cycles.

Figure 4.7: Convergence of the rigid trim optimization problem

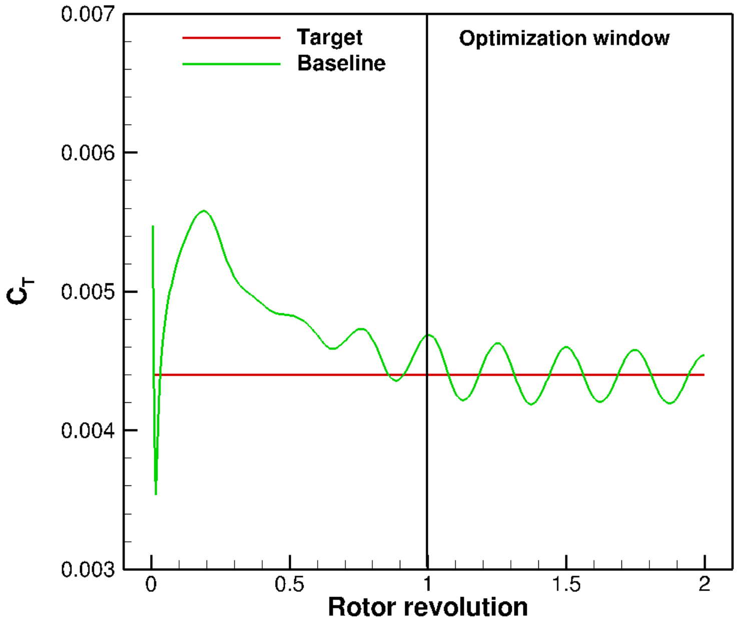

(a) Target and computed thrust time history for the trimmed HART-II rotor

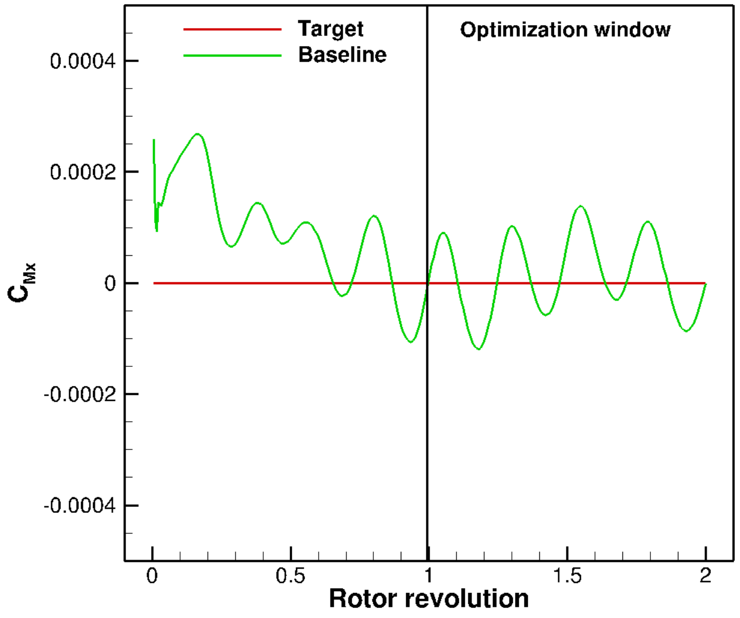

(b) Target and computed roll moment time history for the trimmed HART-II rotor

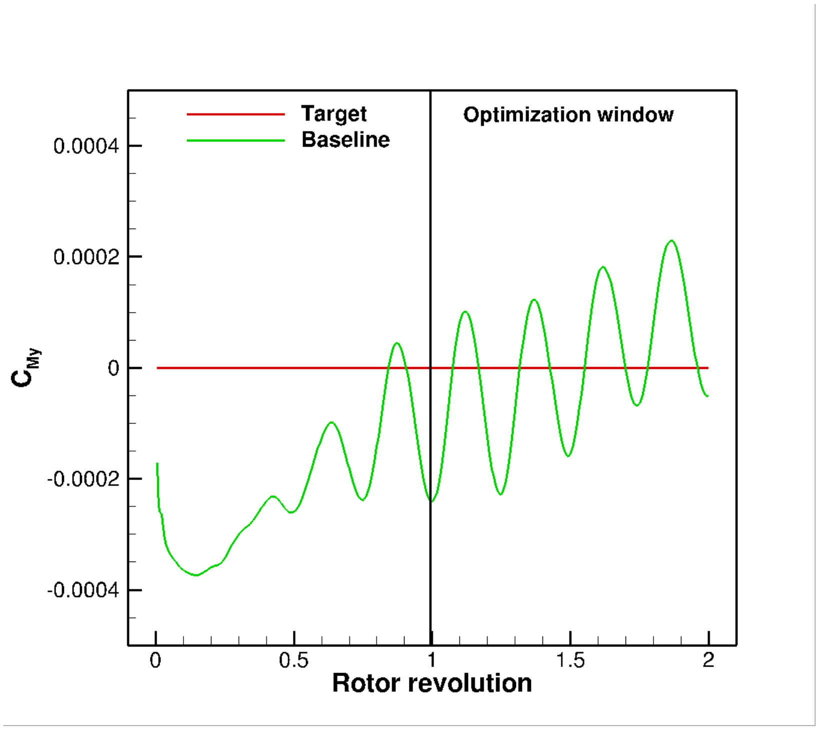

(c) Target and computed pitch moment time history for the trimmed HART-II rotor

Figure 4.8: Thrust and moments time histories for the trimmed baseline HART-II rigid rotor

Table 4.3: Twist, collective and cyclics values for the baseline and the aeroacoustically optimized rigid rotors. All quantities in degrees

	Baseline (deg)	Aeroacoustic opt. (deg)
Root twist	6.0000	6.006
Tip twist	-2.0000	-2.2513
Collective θ_0	-0.7769	-1.0278
Cyclic θ_{1c}	0.8954	1.3687
Cyclic θ_{1s}	-1.7161	-1.7140

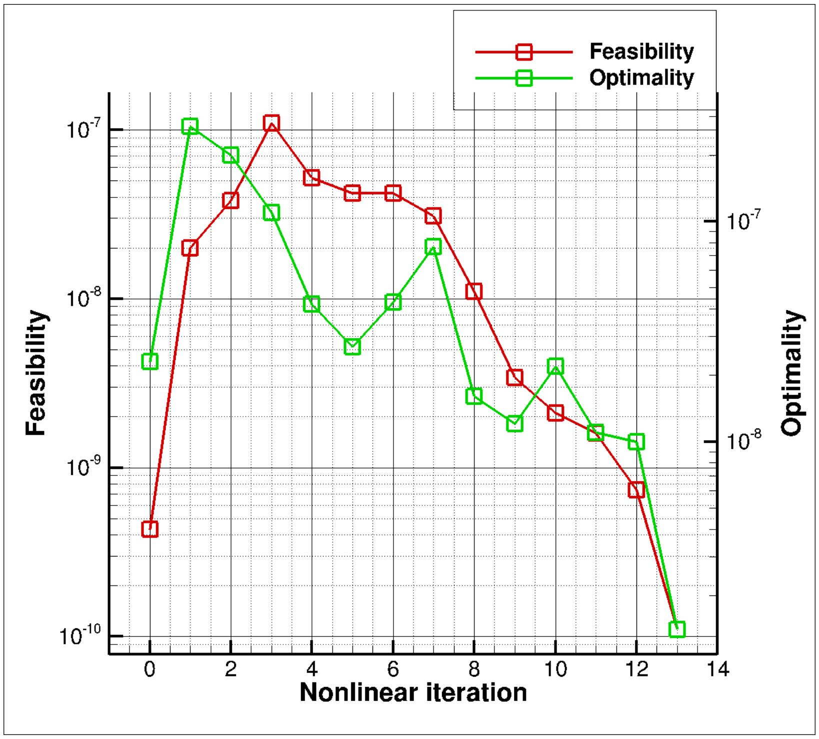

(a) Feasibility and optimality for the aeroacoustic optimization problem as a function of nonlinear iterations

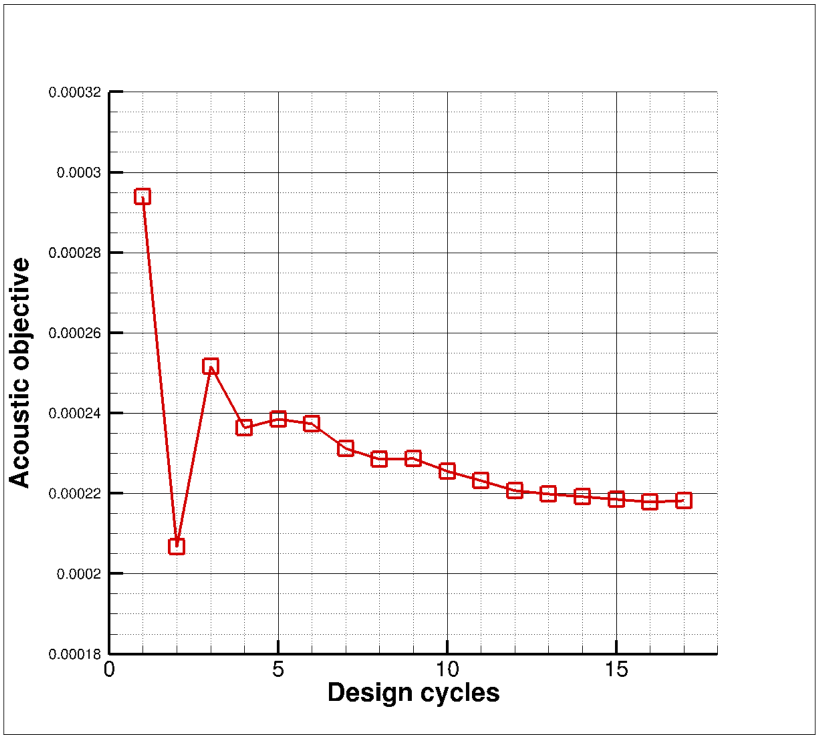

(b) Convergence of the aeroacoustic objective function as a function of design cycles.

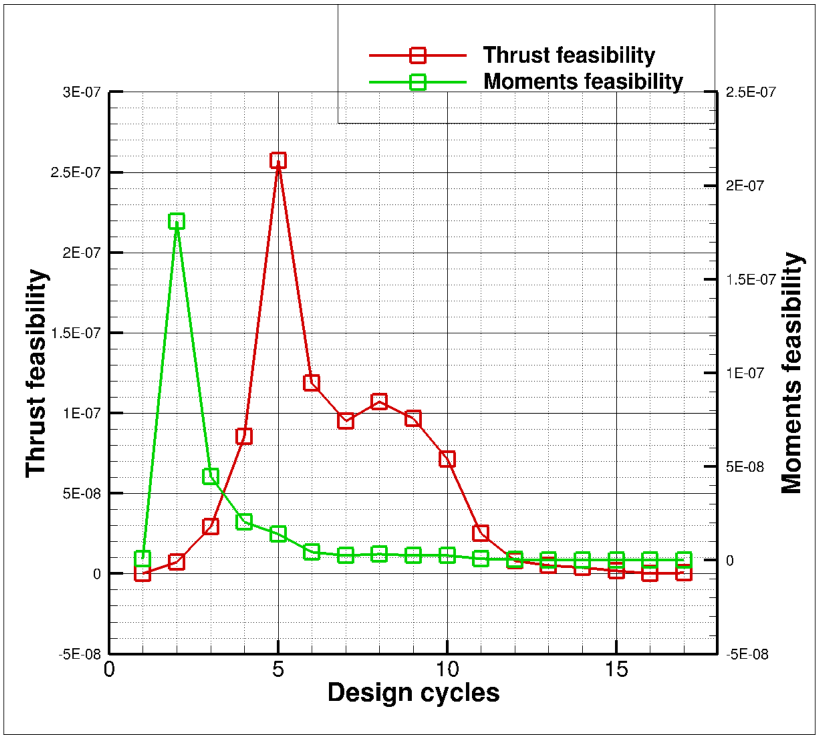

(c) Convergence of the trim constraint as a function of design cycles.

Figure 4.9: Convergence of the aeroacoustic optimization problem for the rigid HART-II rotor

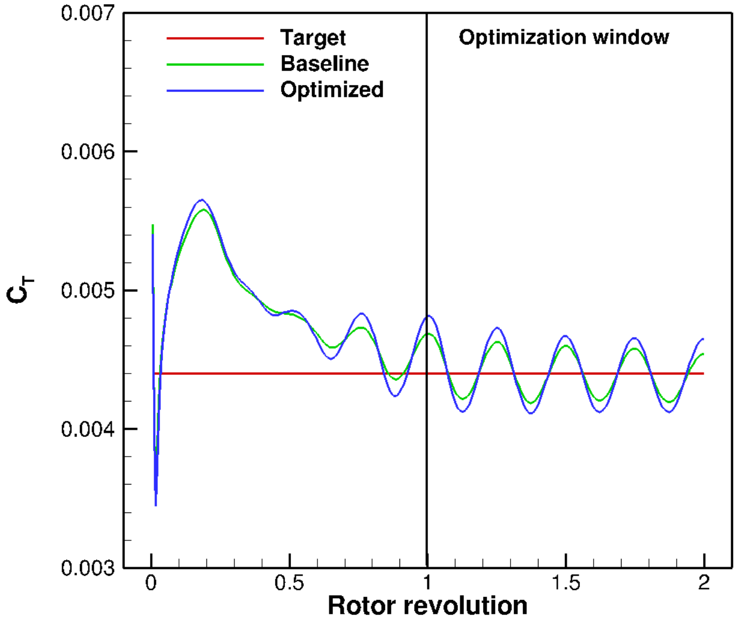

(a) Thrust time history for the baseline and the aeroacoustically optimized trimmed HART-II rigid rotor

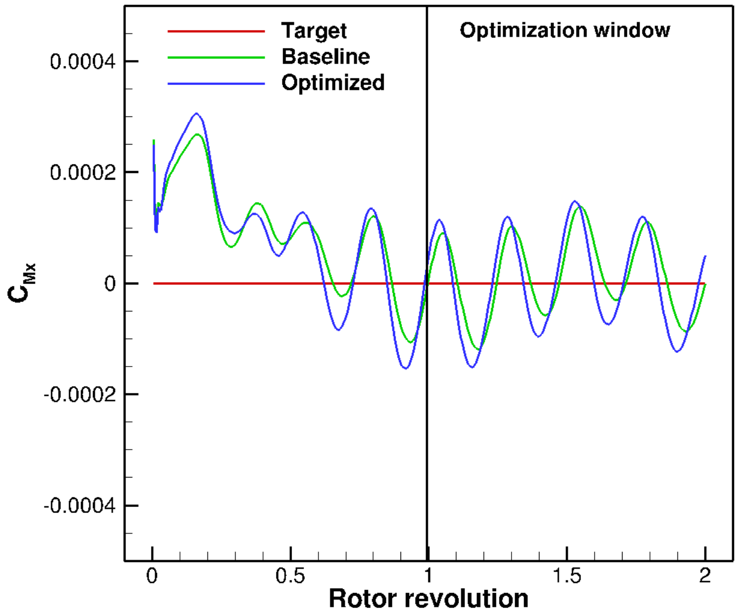

(b) Rolling moment time history for the baseline and the aeroacoustically optimized trimmed HART-II rigid rotor

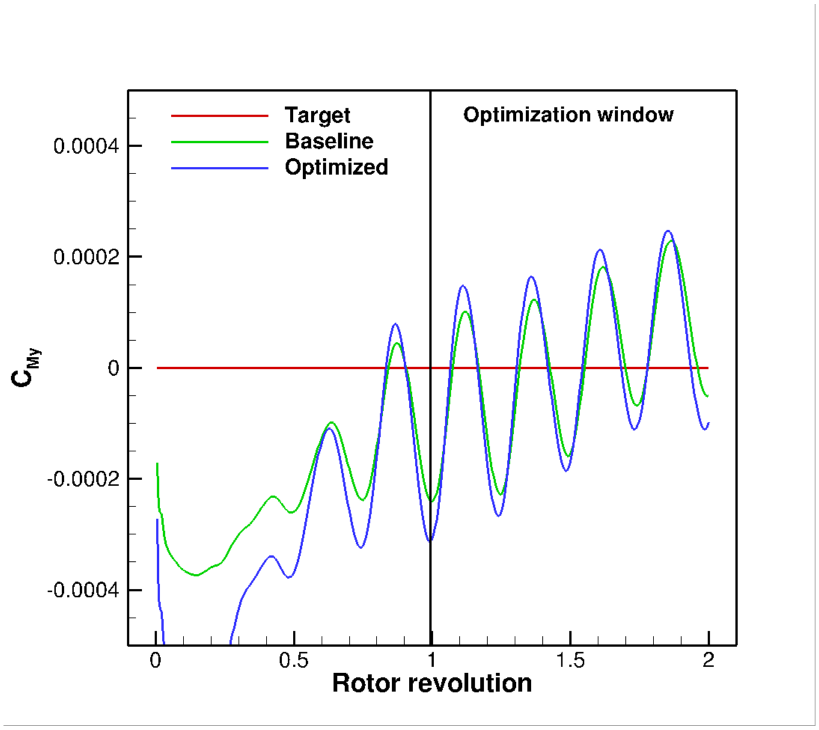

(c) Pitching moment time history for the baseline and the aeroacoustically optimized trimmed HART-II rigid rotor

Figure 4.10: Thrust and moment time histories for the aeroacoustically optimized HART-II rigid rotor

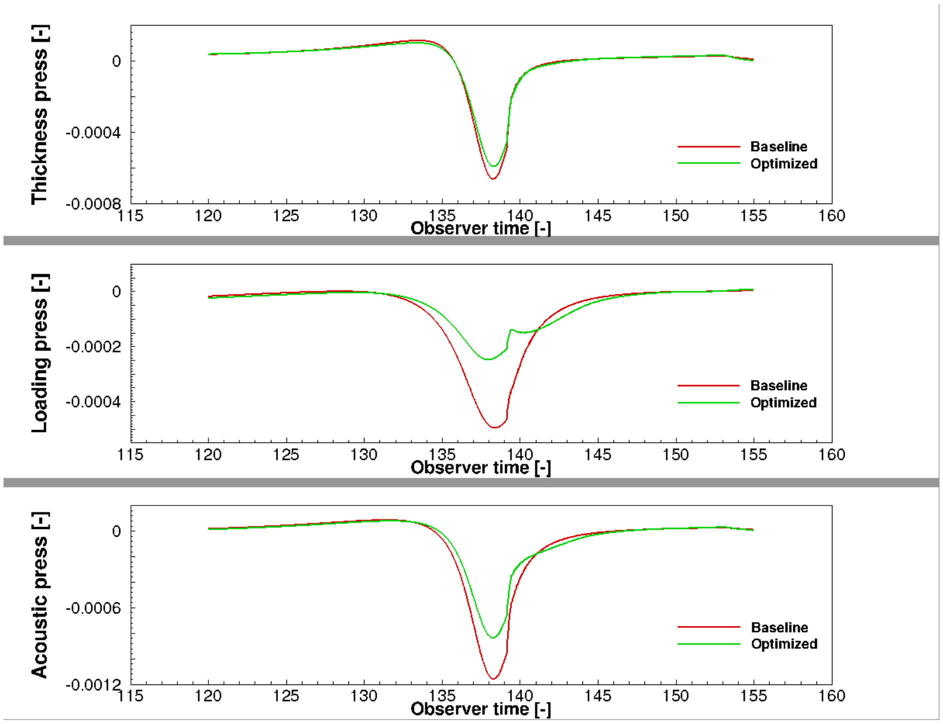

Figure 4.11: Thickness, loading and total acoustic pressures at the observer for the aeroacoustically optimized rigid rotor

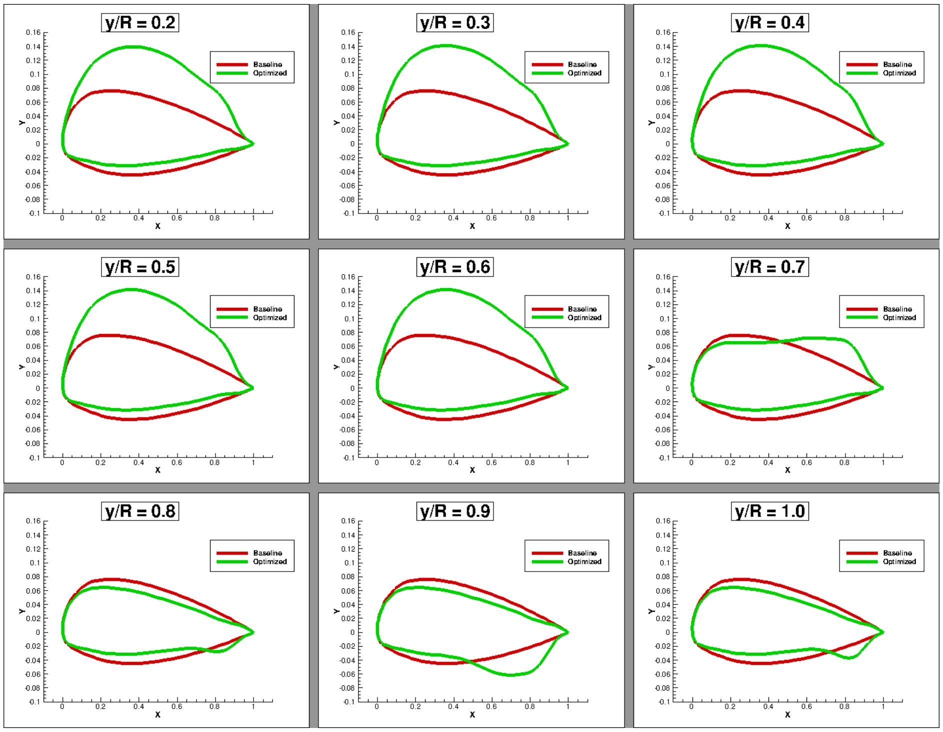

Figure 4.12: Baseline and optimized airfoil shapes for the aeroacoustically optimized rigid rotor

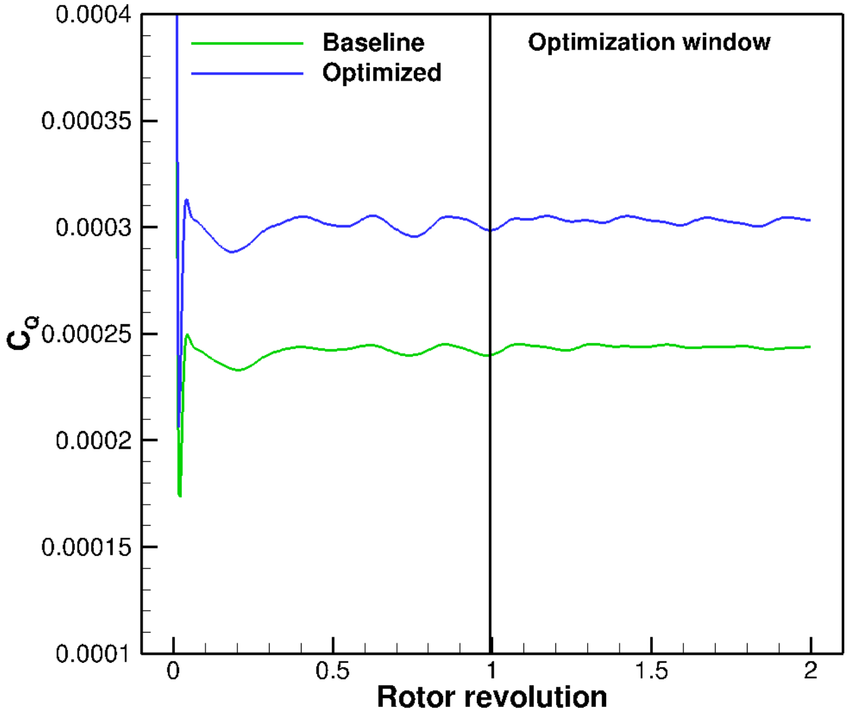

Figure 4.13: Baseline and optimized torque time histories for the aeroacoustically optimized rigid rotor showing the performance penalty paid to minimize the acoustic signature.

Since rotor torque is not included in the optimization, the noise reduction achieved here, despite representing the maximum noise reduction achievable within the current optimization framework, comes at the expense of rotor performance, as clearly indicated in Figure 4.13. Consequently the next step is to introduce a torque constraint in the optimization process.

Torque-constrained Aerocoustic Optimization

The initial design for this multidisciplinary aeroacoustic optimization is again the trimmed HART-II rigid rotor and the optimization problem is described in equation (4.7). After 20 design cycles the acoustic objective function settles down while attaining the same torque level as the baseline HART-II rotor, as shown in Figure 4.14(b). The trim constraint feasibility is shown in Figure 4.14(c) and indicates that the optimized rotor is trimmed, as confirmed by the thrust and lateral moments time histories shown in Figure 4.15. Contrary to the aeroacoustic optimization, the

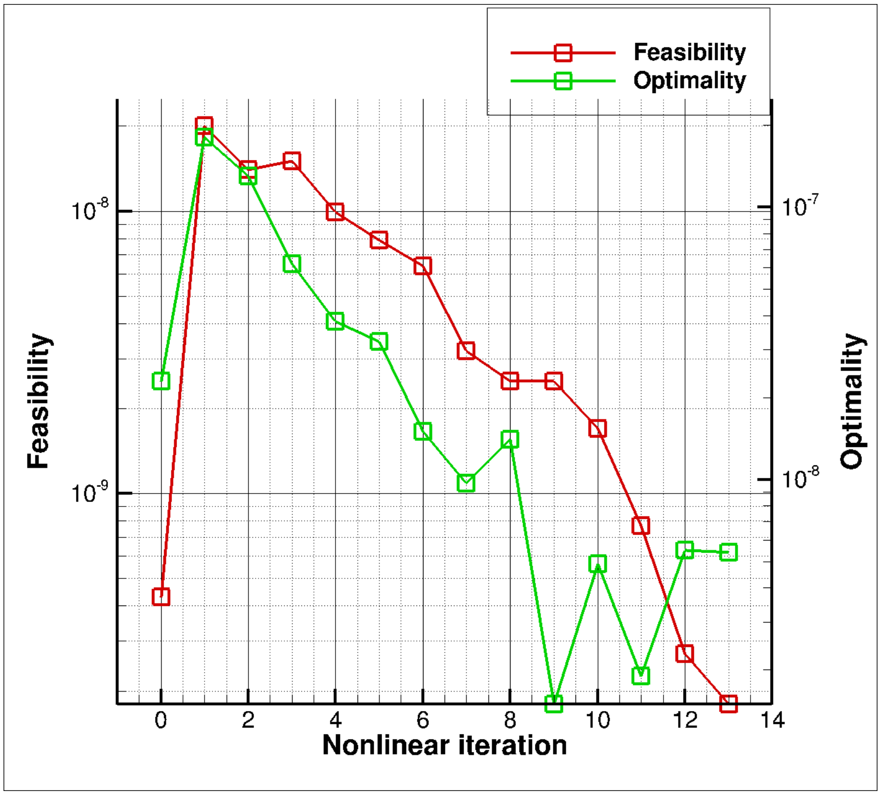

(a) Feasibility and optimality for the torque-constrained aeroacoustic optimization problem as a function of nonlinear iterations

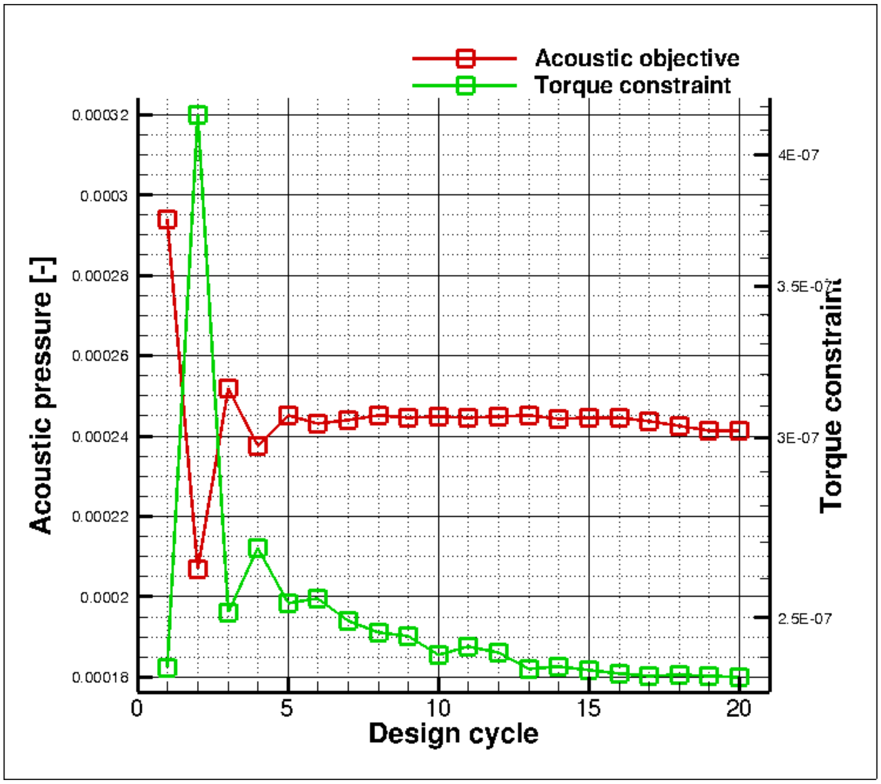

(b) Convergence of the acoustic objective function and the torque constraint as a function of design cycles.

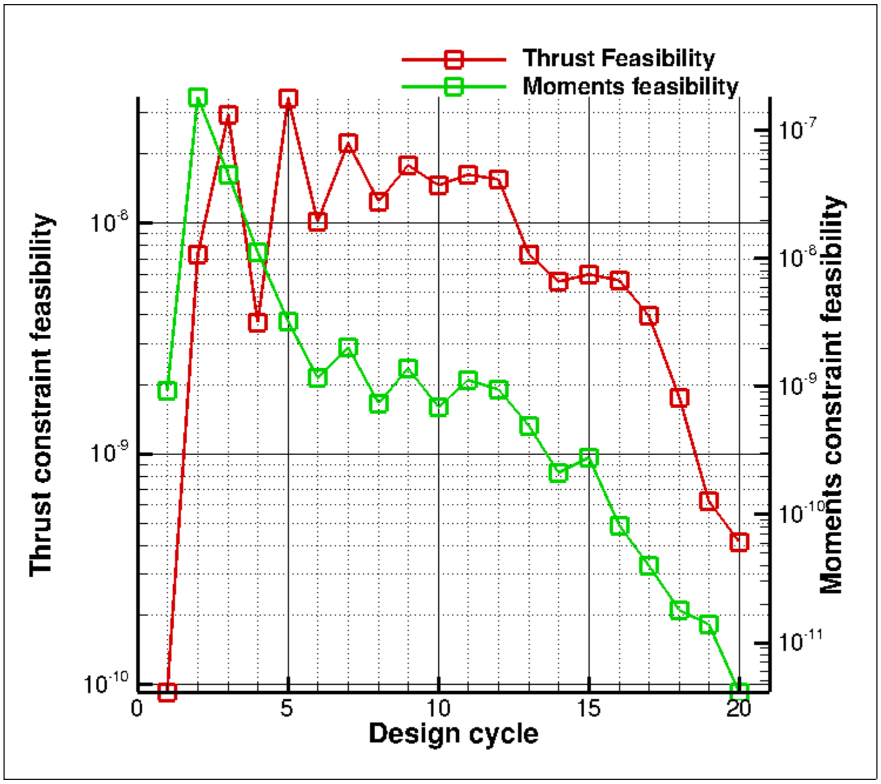

(c) Convergence of the trim feasibility as a function of design cycles.

Figure 4.14: Convergence of the torque-constrained aeroacoustic optimization problem

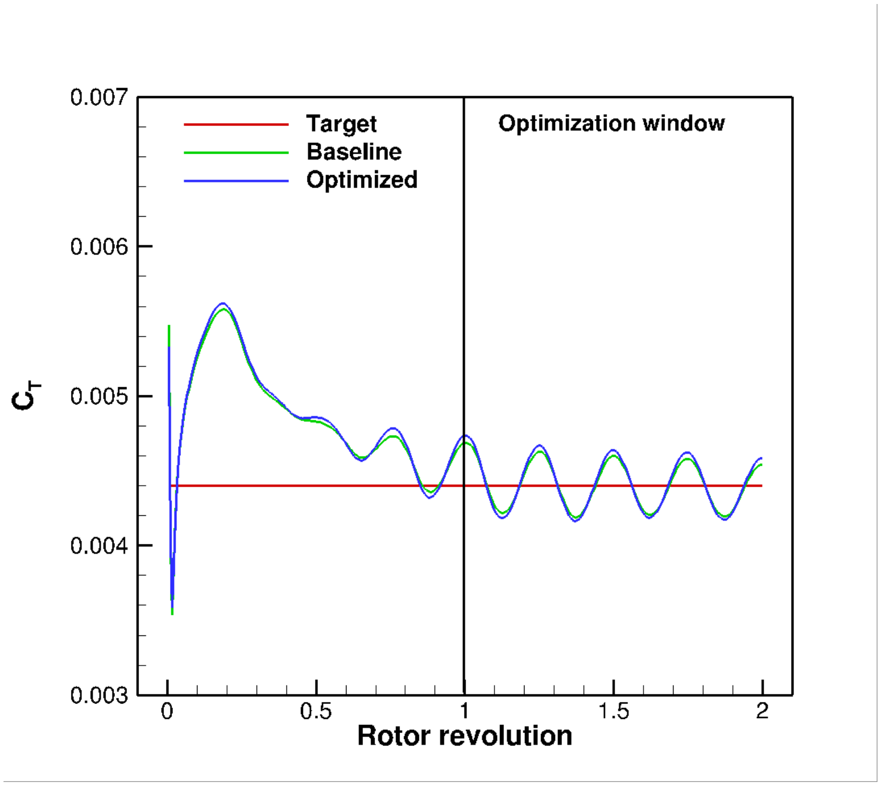

(a) Thrust time history for the baseline and torque-constrained aeroacoustically optimized trimmed HART-II rigid rotor

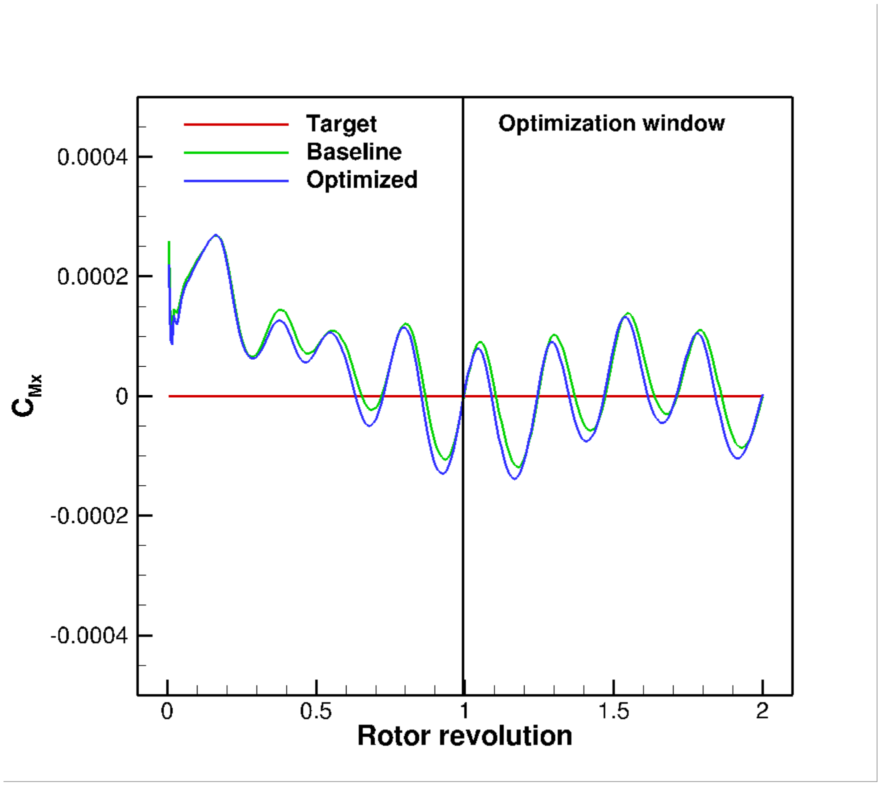

(b) Rolling moment time history for the baseline and the torque-constrained aeroacoustically optimized trimmed HART-II rigid rotor

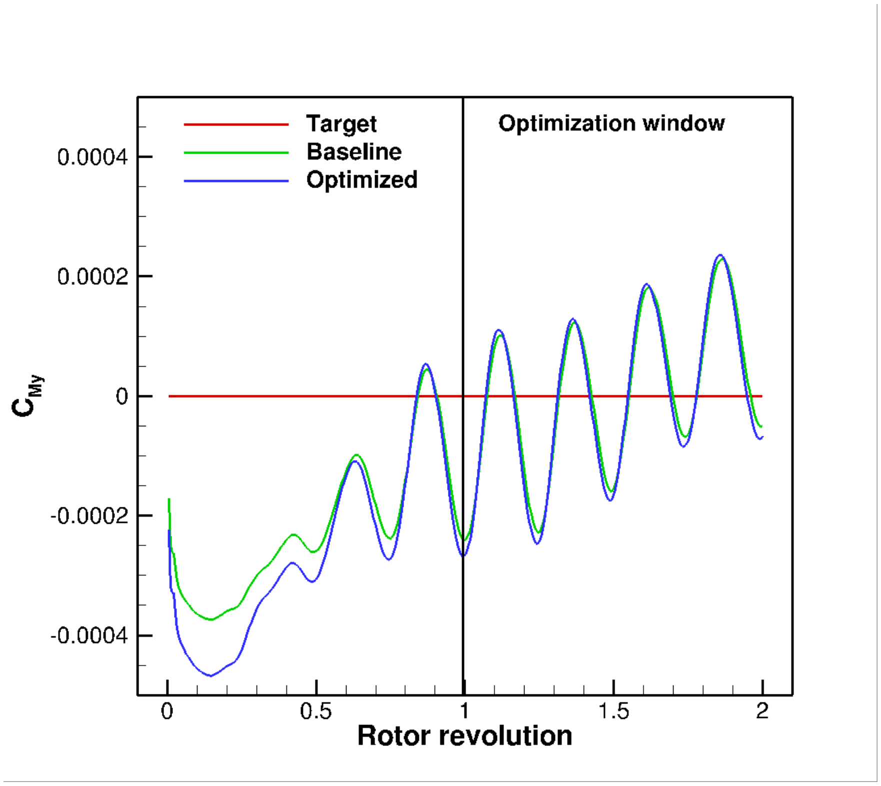

(c) Pitching moment time history for the baseline and the torque-constrained aeroacoustically optimized trimmed HART-II rigid rotor

Figure 4.15: Thrust and moment time histories for baseline and the torque-constrained aeroacoustically optimized trimmed HART-II rigid rotor

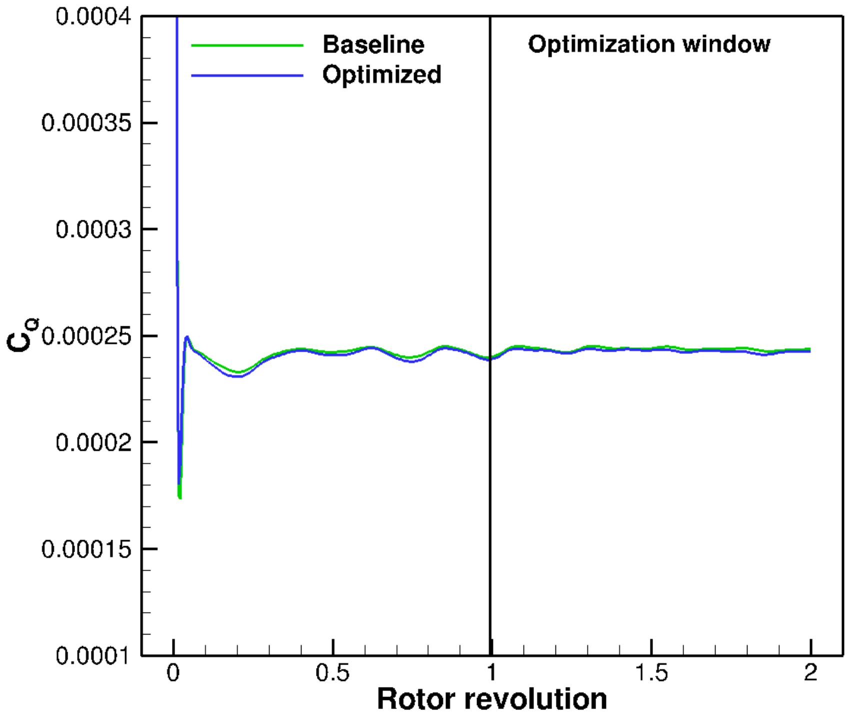

Figure 4.16: Baseline and optimized torque time histories for the torque-constrained aeroacoustically optimized rigid rotor.

torque level for the torque-constrained aeroacoustically optimized rigid rotor is the same as that of the baseline HART-II rigid rotor as shown in Figure 4.16. Thickness, loading and total acoustic pressure time histories at the observer are shown in Figure 4.17. The optimized rotor is 1.7 dB quieter in terms of Overall Sound Pressure Level. A comparison between the baseline and optimized airfoils is shown in Figure 4.18 where it can be seen that, as in the case of the aeroacoustic optimization in the previous section, the optimized shapes tend to be thicker at the inboard stations and thinner at the outboard ones. Twist and pitch control variables are given in Table 4.4.

Previous noise mitigation studies [8] have shown that optimizing for one observer location can result in higher noise levels at different observer locations. A directivity study for the optimized rotor reveals that the current design is capable of reducing noise at in-plane observer locations that have not been targeted by the optimization as shown for two different observers placed at $\psi = 135$ and $\psi = 315$ degrees as shown in Figure 4.19.

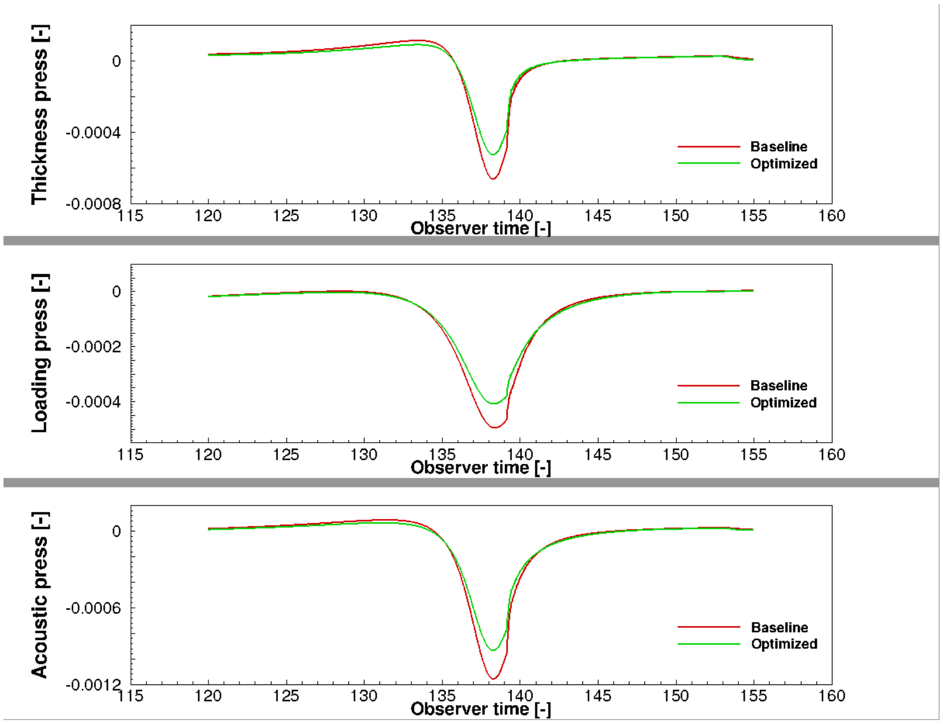

Figure 4.17: Thickness, loading and total acoustic pressures at the observer for the torque - constrained aeroacoustically optimized rigid rotor

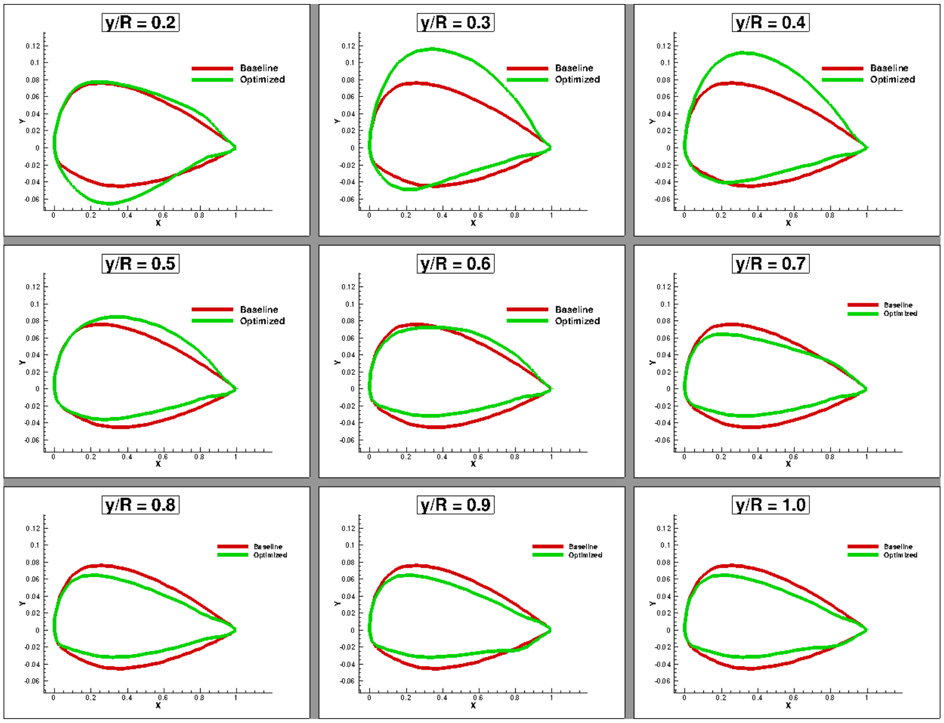

Figure 4.18: Torque-constrained aeroacoustically optimized airfoil shapes

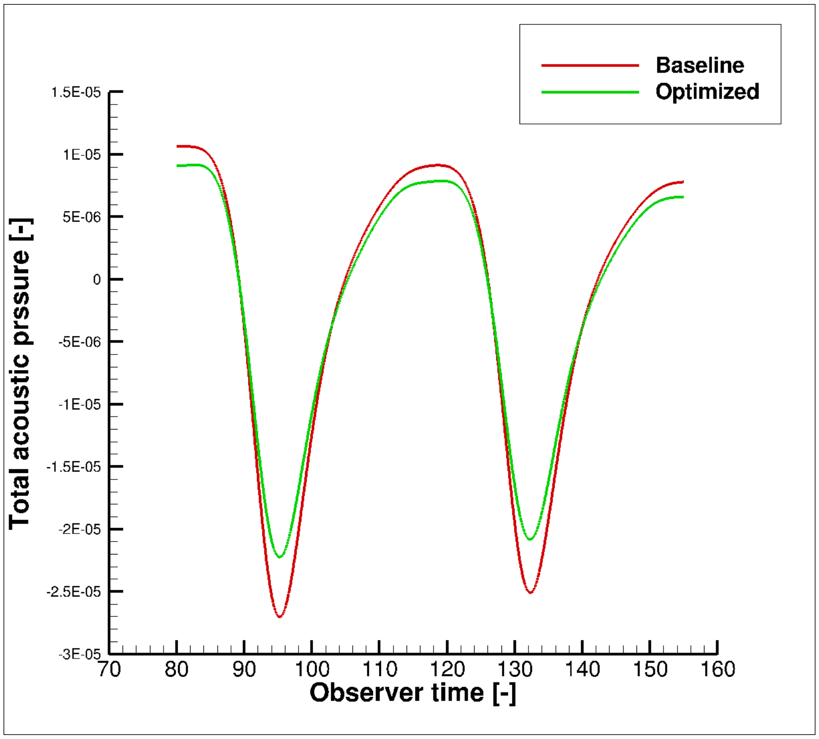

(a) Baseline and optimized total acoustic pressure time history at $\psi = 135$ degrees

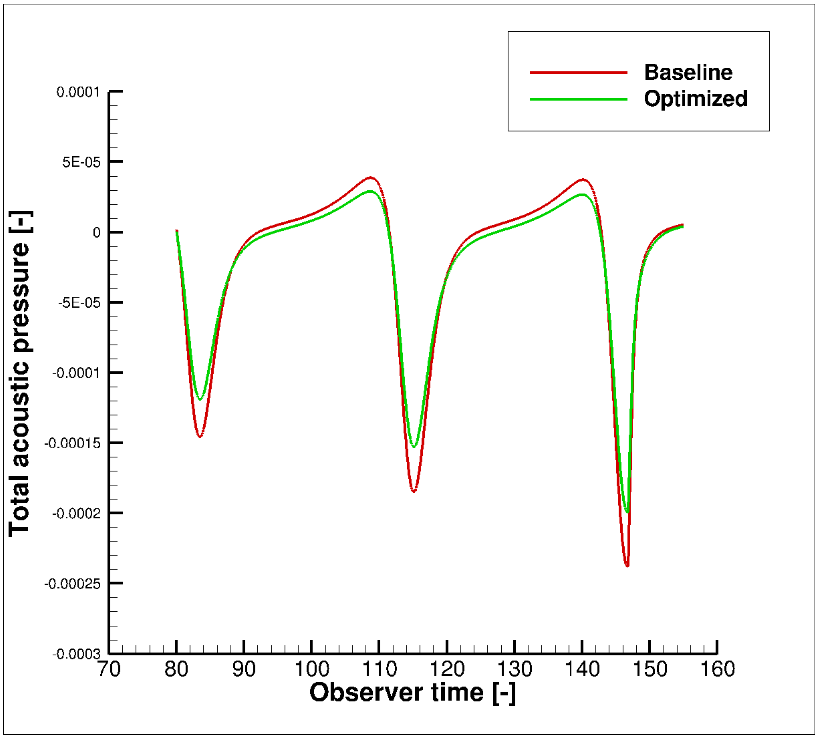

(b) Baseline and optimized total acoustic pressure time history at $\psi = 315$ degrees

Figure 4.19: Directivity study for the baseline and optimized rigid rotor geometries

Table 4.4: Twist, collective and cyclics values for the baseline and the aeroacoustically optimized rigid rotors. All quantities in degrees.

	Baseline (deg)	Aeroacoustic opt. (deg)
Root twist	6.0000	6.0043
Tip twist	-2.0000	-2.1625
Collective θ_0	-0.7769	-0.9337
Cyclic θ_{1c}	0.8954	1.0746
Cyclic θ_{1s}	-1.7161	-1.7310

4.2.2 Flexible HART-II Rotor

The aeroacoustic optimization of the flexible HART-II rotor in trimmed forward flight is presented next to realize the flexible aeroacoustic adjoint capability that represents the unique aspect of the current work.

Trim Results

The trim optimization problem is described by equation (4.5) and the optimization convergence is shown in Figure 4.20. After 15 nonlinear iterations and 22 design cycles the feasibility and optimality of the optimization problem are reduced by approximately 3 orders of magnitude and the baseline flexible HART-II rotor is trimmed as further confirmed by thrust and lateral moments time histories shown in Figure 4.21. The trimmed HART-II rotor will now serve as the initial design for all subsequent flexible aeroacoustic optimizations.

Aeroacoustic Optimization

The current optimization problem is described by equation (4.6) and SNOPT convergence is shown in terms of nonlinear optimization iterations and design cycles in Figure 4.22. After 27 design cycles the optimization produces a geometry that reduces the Overall Sound Pressure Level by 2.6 dB while keeping the rotor trimmed as highlighted by the thrust and lateral moments time histories shown in Figure 4.23. The acoustic pressure time history is shown in Figure 4.24. The main reduction in total acoustic pressure comes from the reduction in thickness noise while the reduction of the loading pressure peak is less significant. The nature of the aeroacoustic problem

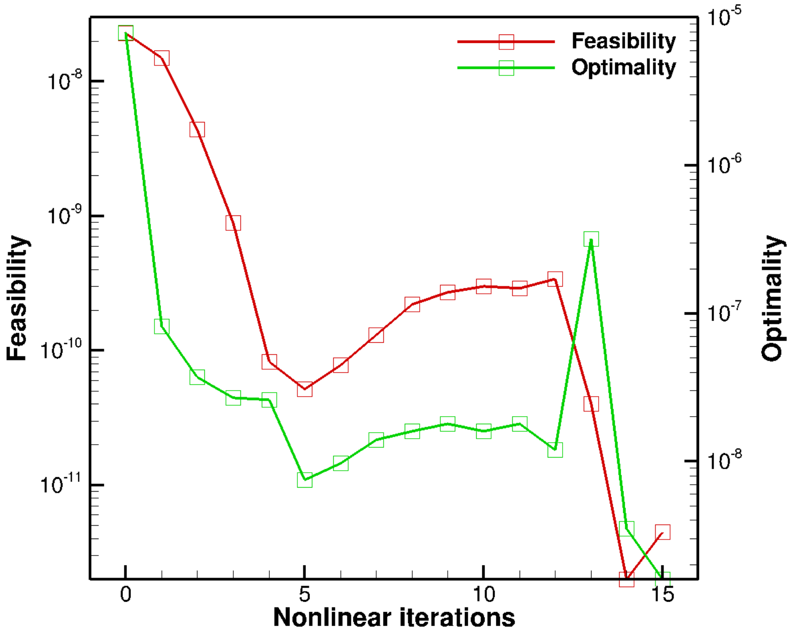

(a) Feasibility and optimality of the trim problem as a function of nonlinear optimization iterations

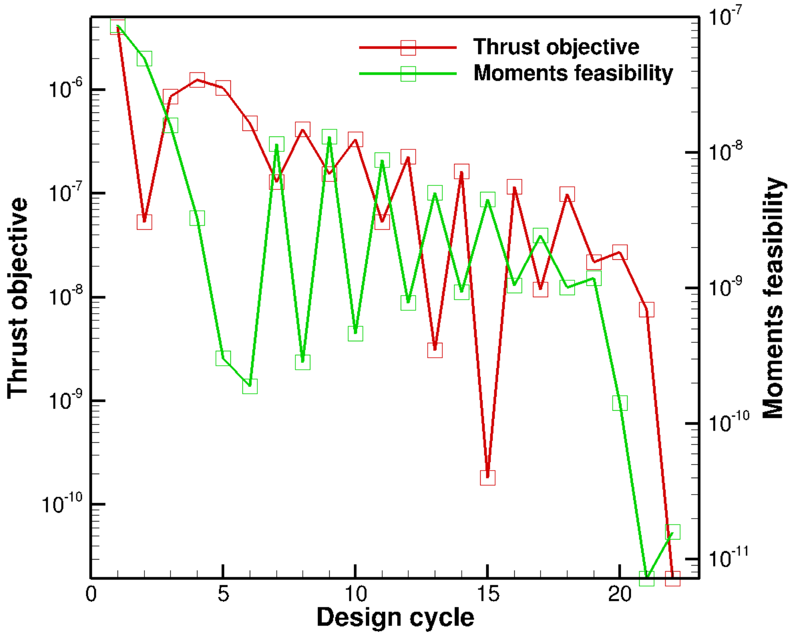

(b) Convergence of the thrust objective function and moment constraint as a function of design cycles.

Figure 4.20: Convergence of the trim optimization problem for the flexible HART-II rotor

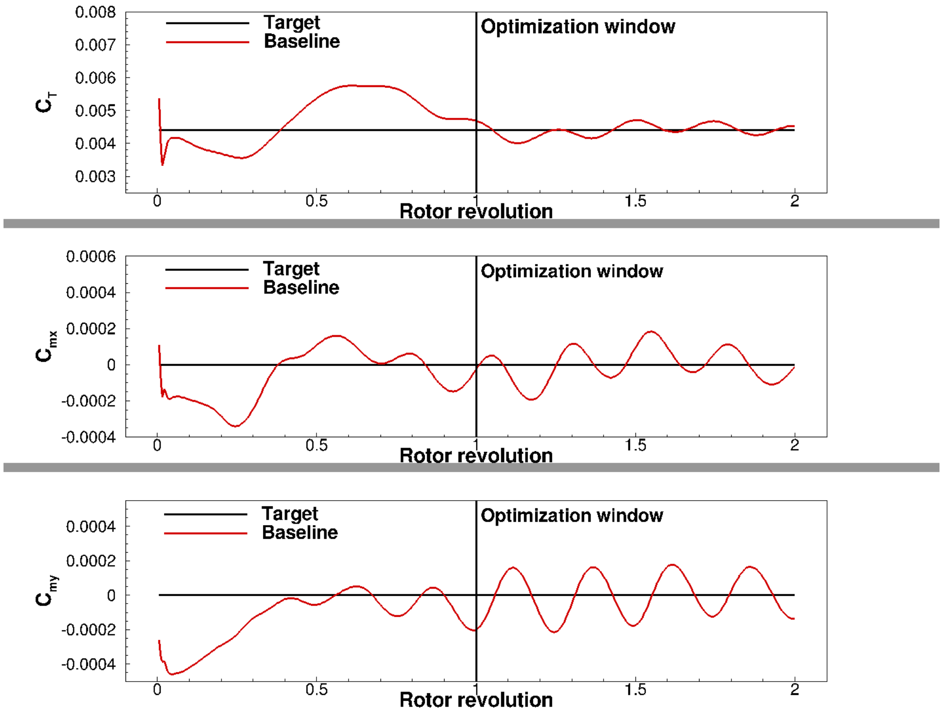

Figure 4.21: Thrust and moments time histories for the baseline HART-II flexible rotor

dictates the optimization behavior: for in-plane noise problems thickness noise is the dominant source of noise [74], hence SNOPT chooses a trimmed geometry that minimizes thickness noise. The noise minimization is achieved with rather thick airfoils especially at the inboard sections, as shown in Figure 4.25. Blade root cap shape considerations dictate the shape of the most inboard airfoil at the first spanwise station: the blade cap is built as a surface of revolution that joins the upper and lower surface of the blade, the design variables for the root airfoil needed to be bounded more than the design variables for the other airfoils to guarantee a reasonable blade root cap, resulting in the first airfoil shown in Figure 4.25. Twist and pitch design variables are shown in Table 4.5. Since rotor torque is not included in the optimization, the noise reduction achieved here, despite representing the maximum noise reduction achievable within the current optimization framework, comes at the expense of rotor performance, as clearly indicated in Figure 4.26.

The optimization described by equation (4.7) and discussed in the next section adresses this issue by minimizing the required torque while constraining the acoustic signature to a lower noise level than the baseline rotor.

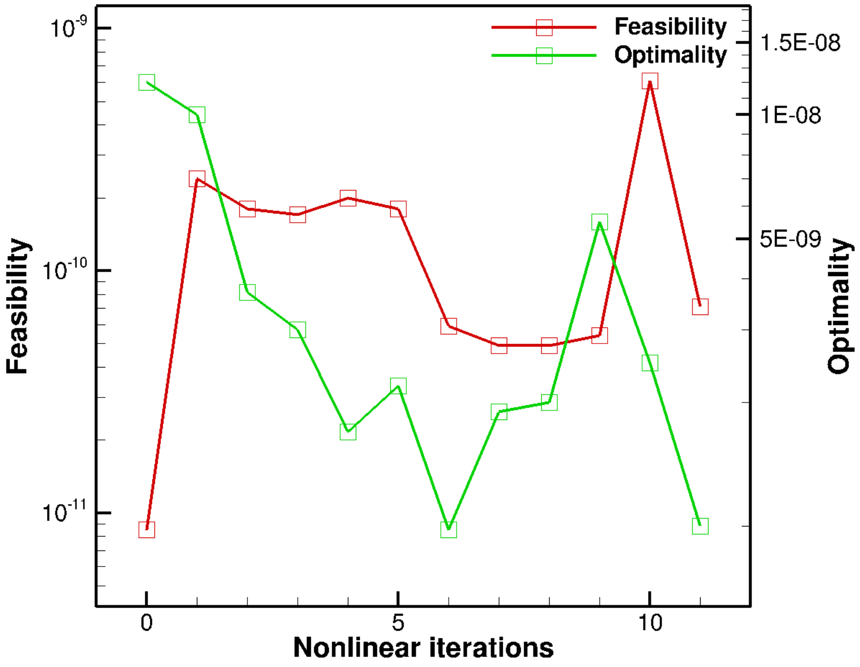

(a) Feasibility and optimality for the aeroacoustic optimization problem as a function of nonlinear iterations

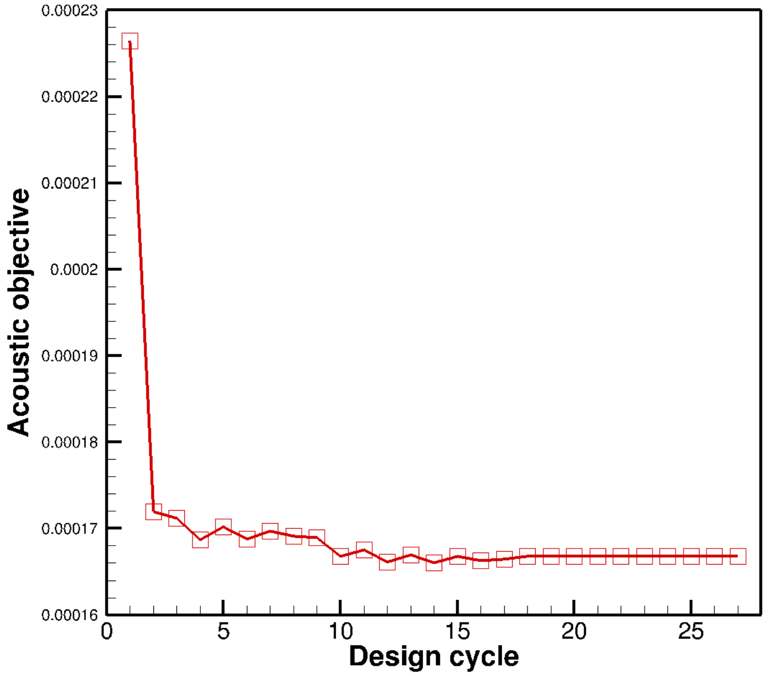

(b) Convergence of the aeroacoustic objective function as a function of design cycles.

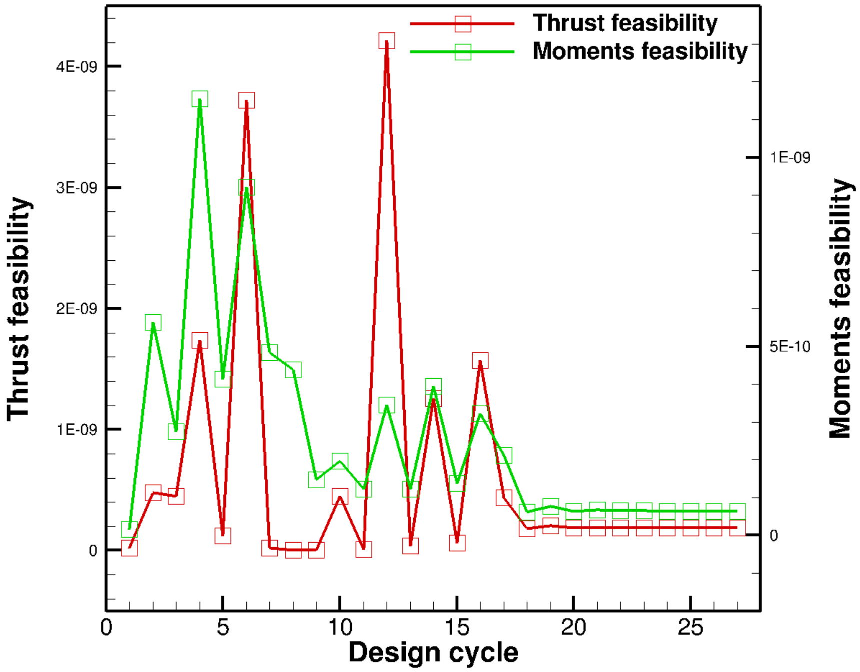

(c) Convergence of the trim constraint as a function of design cycles.

Figure 4.22: Convergence of the flexible aeroacoustic optimization problem

Table 4.5: Twist, collective and cyclics values for the baseline and the aeroacoustically optimized flexible rotors. All quantities in degrees.

	Baseline (deg)	Aeroacoustic opt. (deg)
Root twist	6.0000	6.0947
Tip twist	-2.0000	-2.7574
Collective θ_0	-0.4986	-1.1146
Cyclic θ_{1c}	1.3678	1.5074
Cyclic θ_{1s}	-2.5530	-2.8053

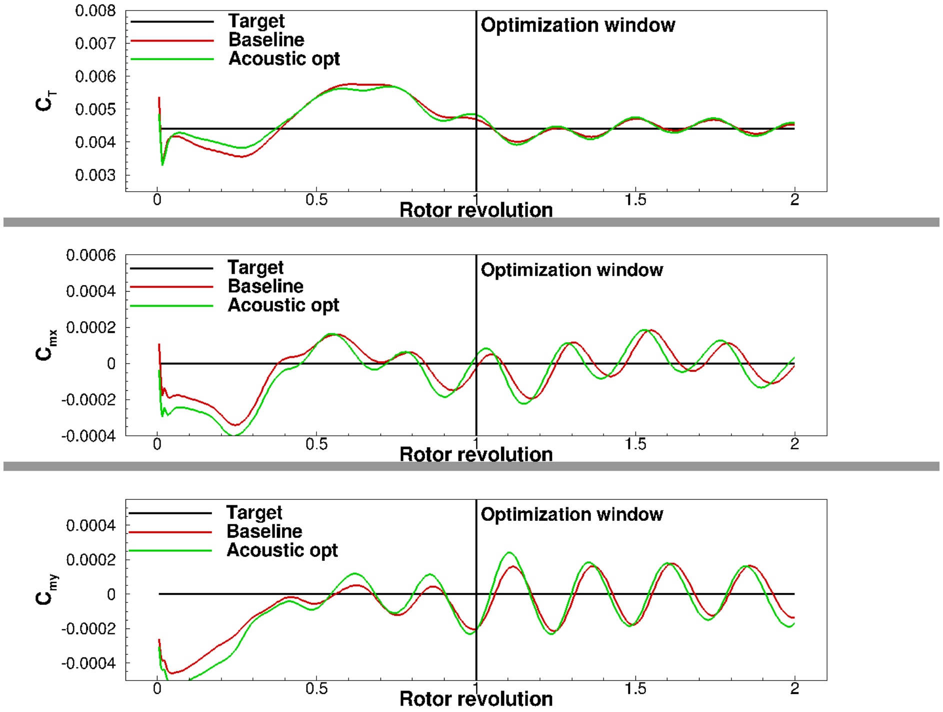

Figure 4.23: Thrust and moments time histories for the baseline and optimized flexible HART-II rotors

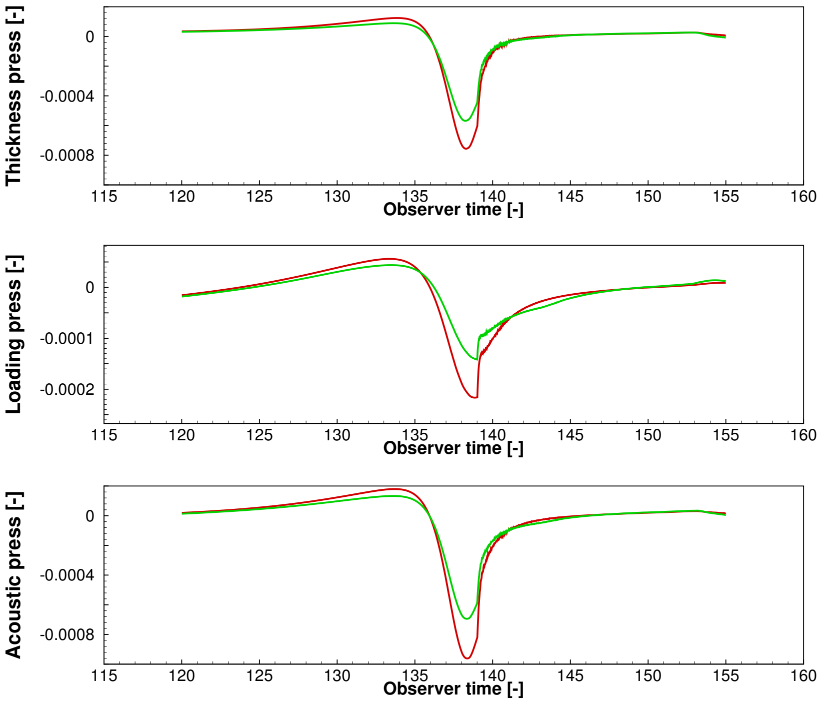

Figure 4.24: Thickness, loading and total acoustic pressures at the observer for the baseline (red) and the aeroacoustically optimized (green) flexible rotors

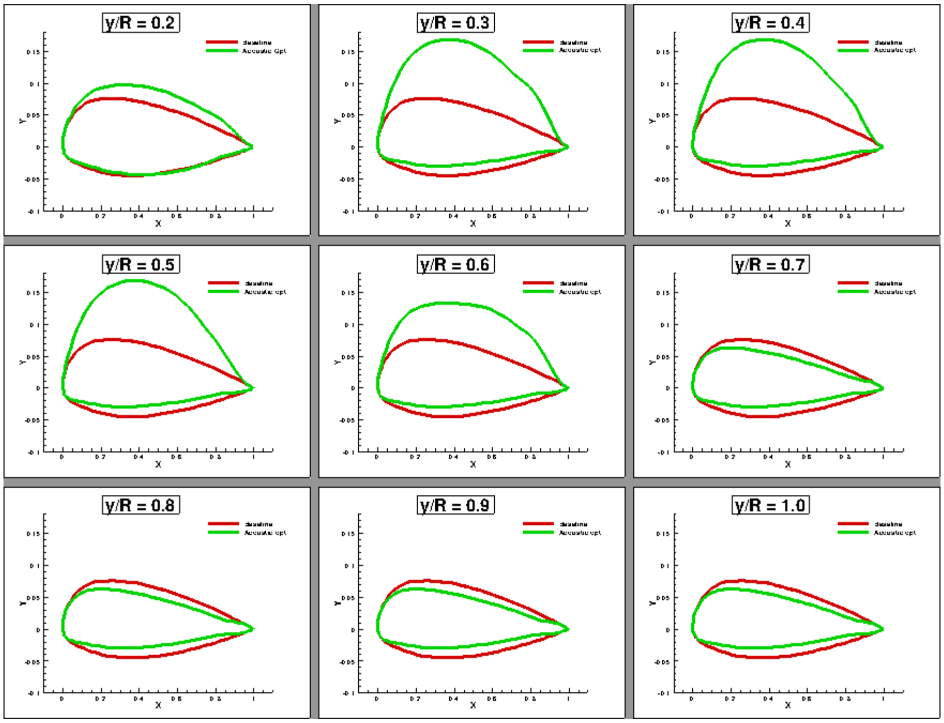

Figure 4.25: Baseline (red) and optimized (green) airfoil shapes for the aeroacoustically optimized flexible rotors

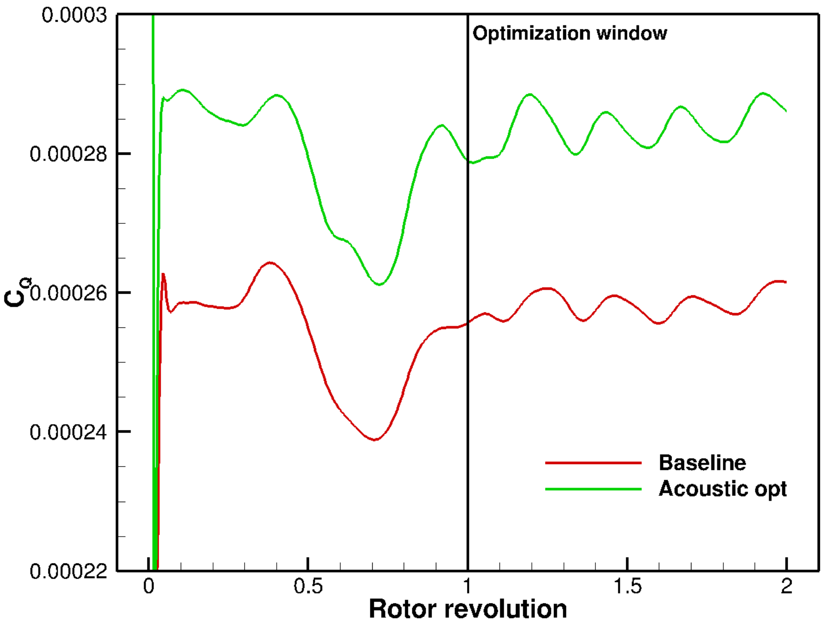

Figure 4.26: Torque time history for the baseline and aeroacoustically optimized flexible rotors showing the performance penalty paid to minimize the acoustic signature.

Table 4.6: Twist, collective and cyclics values for the baseline and the aeroacoustically optimized flexible rotors. All quantities in degrees.

	Baseline (deg)	Aeroacoustic opt. (deg)
Root twist	6.0000	5.9996
Tip twist	-2.0000	-2.0022
Collective θ_0	-0.4986	-0.5028
Cyclic θ_{1c}	1.3678	1.3790
Cyclic θ_{1s}	-2.5530	-2.6021

Acoustically-constrained Torque Minimization

The minimization problem for the optimization presented in this section is described in equation (4.8). In as few as 5 nonlinear iterations feasibility is reduced by more than 2 orders of magnitude while optimality is reduced by approximately 9 orders of magnitude, as shown in Figure 4.27(a). After 10 design cycles the acoustic constraint is satisfied resulting in a rotor with a 2dB OSPL reduction compared to the baseline, while the required torque is reduced by 2.5% as shown in Figure 4.27(b). Satisfaction of the trim constraint is shown in Figure 4.27(c) and confirmed by the thrust and lateral moment time histories shown in Figure 4.28. A comparison of the torque time histories is shown in Figure 4.29 highlighting the 2.5% torque reduction achieved for this optimization. The thickness, loading and total acoustic pressure time histories are shown in Figure 4.30. The thickness acoustic pressure is essentially the same between the current optimization and the one from the previous section, suggesting that the two minimizations exploit the same noise reduction mechanism, while loading pressure reduction for the current optimization is significantly lower. A comparison of the airfoil shapes for the baseline and the two optimized rotors is shown in Figure 4.31 highlighting that the acoustically constrained torque minimization results in more conventional blade shapes at the inboard sections while recovering the same airfoils of the aeroacoustic optimization at the outboard sections. Twist and pitch control parameters for this optimization are shown in Table 4.6.

As for the case of the rigid rotor, a directivity study for the baseline and the optimized flexible rotors is performed and reveals that the current design is capable of reducing noise at in-plane observer

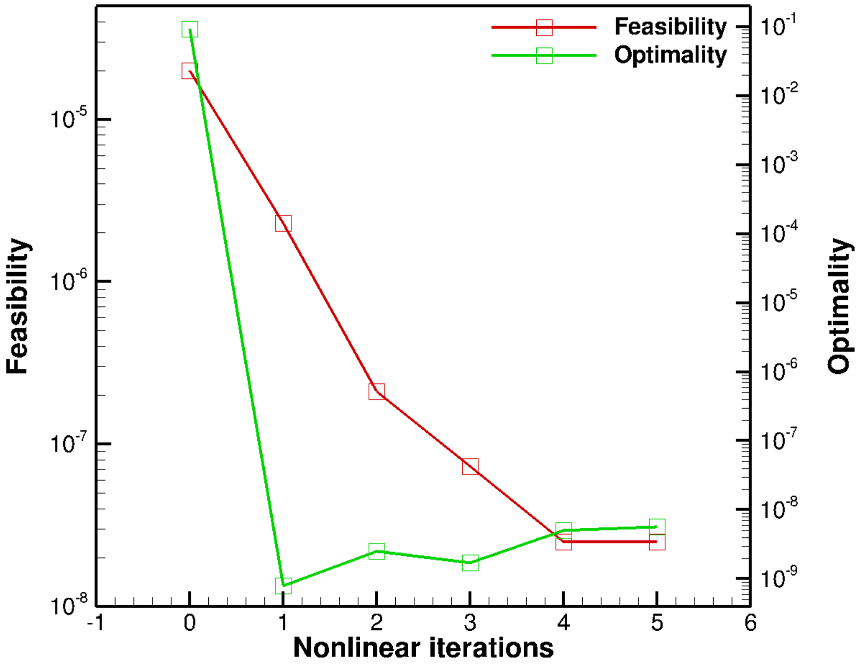

(a) Feasibility and optimality for the torque-constrained aeroacoustic optimization problem as a function of nonlinear iterations

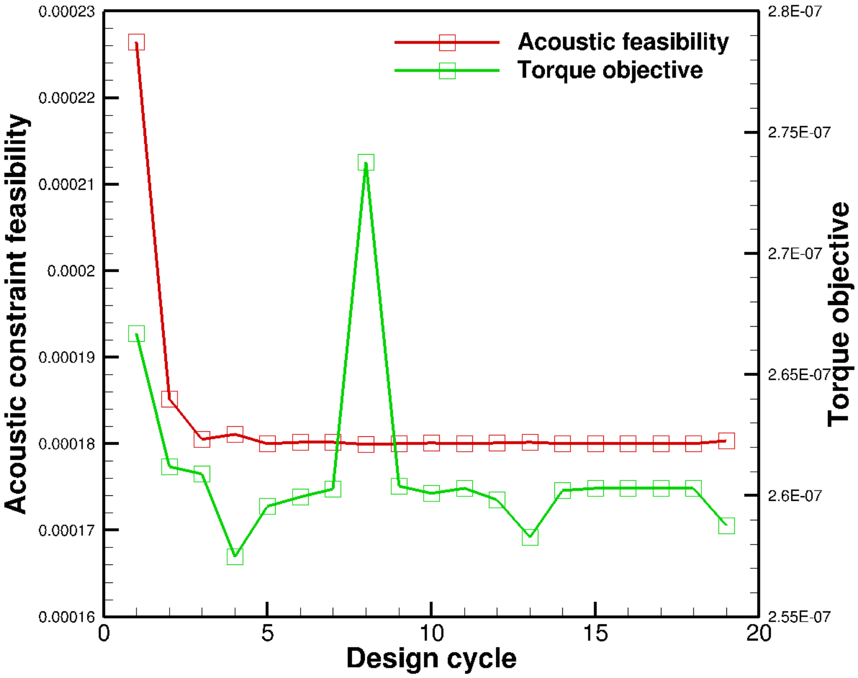

(b) Convergence of the acoustic objective function and the torque constraint as a function of design cycles.

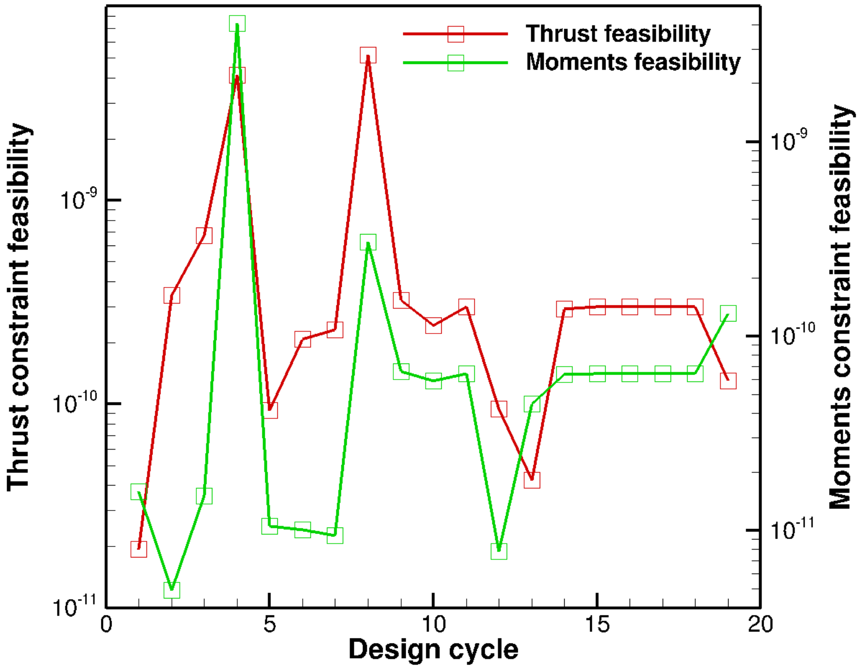

(c) Convergence of the trim feasibility as a function of design cycles.

Figure 4.27: Convergence of the acoustically constrained torque optimization of the flexible HART-II rotor

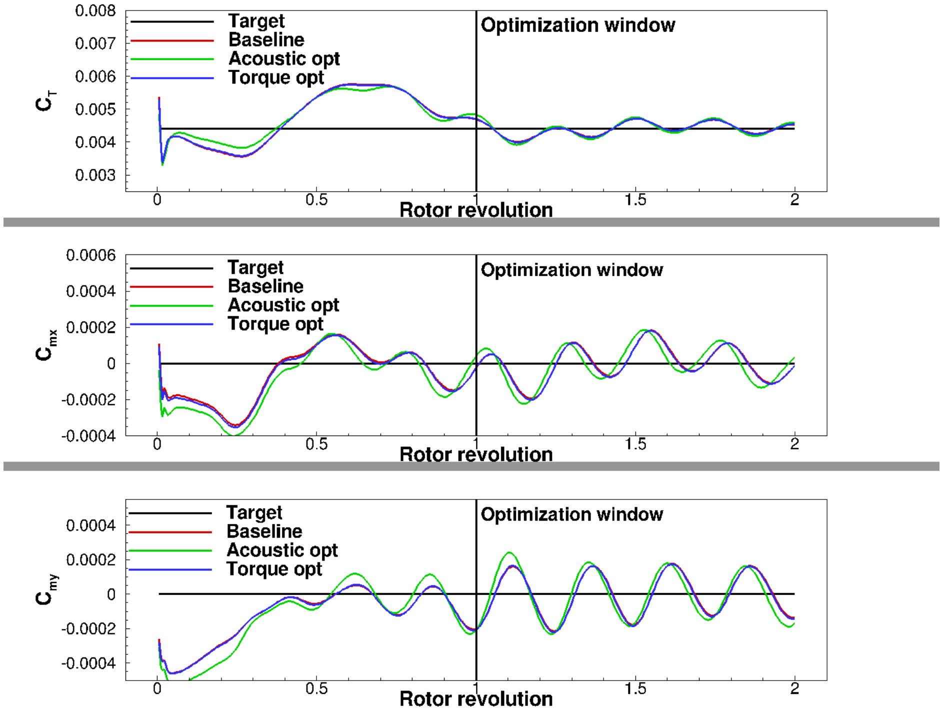

Figure 4.28: Thrust and moments time histories for the baseline, the aeroacoustic optimized and the acoustically constrained torque optimized flexible rotors

locations that have not been targeted by the optimization, as shown in Figures 4.32 and 4.33. Figure 4.32 shows the total acoustic pressure for the baseline and the optimized rotors at the same radial location used during the optimization but for different azimuthal locations, while Figure 4.33 shows the acoustic pressure for the same azimuthal location targeted by the optimization but at different radial distances. In both cases the noise signature for the optimized rotor is smaller than that of the baseline rotor. As mentioned before, thickness acoustic pressure is the dominant source of noise for the current aeroacoustic problem and the solid wall acoustic integration implies that the thickness integral in the FW-H equation (3.12) depends only on geometrical and kinematic parameters of the rotor, hence justifying the results of the current directivity study.

Validation of Optimization Results over Multiple Rotor Revolutions

In this section we investigate the behavior of the baseline and the optimized flexible rotors from the previous sections when their performance is evaluated over multiple rotor revolutions. While the previous computations have been run for only 2 rotor revolutions, the current simulations have

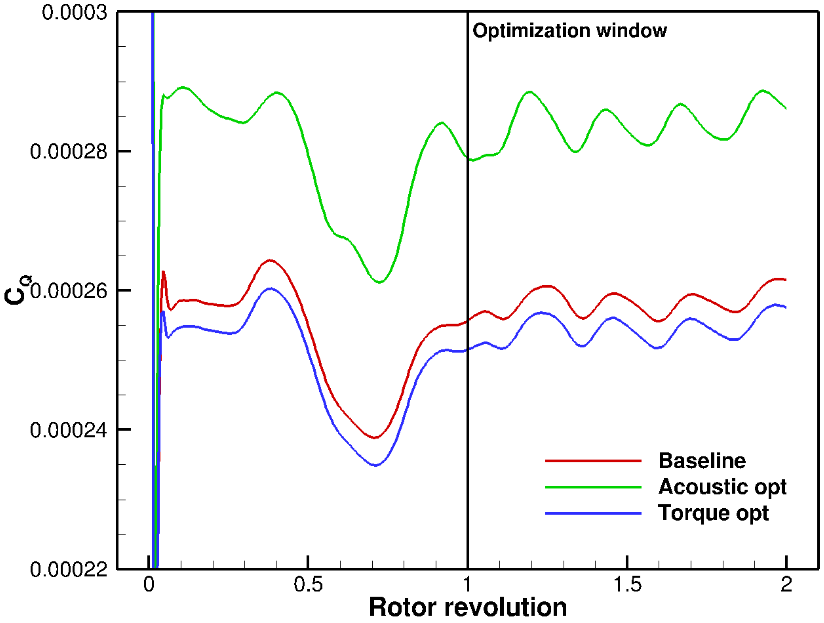

Figure 4.29: Torque time histories for the baseline, the aeroacoustic optimized and the acoustically constrained torque optimized flexible rotors

been run for four rotor revolutions and the aerodynamic objective functions are accumulated over the last 3 revolutions. The acoustic objective function is evaluated over the same observer time window as in the previous sections. The geometry and the control variables are the same as those from the previous sections.

As expected, since the rotor does not achieve a fully periodic state within 2 revolutions, the rotors are now untrimmed for the subsequent revolutions, however the trim constraint is violated by the same amount by the three rotors, as shown in Figure 4.34, allowing for a meaningful comparison of the acoustic signature and of the required torque. The observer acoustic pressure time histories, shown in Figure 4.35, confirm the results from the previous sections: the aeroacoustically optimized rotor yields the most significant noise signature reduction when compared to the baseline rotor with a noise reduction of 2.7 dB OSPL at the observer, however the required torque is significantly increased, as shown in Figure 4.36. The acoustically constrained torque optimized rotor yields 2.9% reduction in required torque with a 1.9 dB OSPL reduction in noise signature.

These results show that even if the optimizations targeted only the second rotor revolution, they

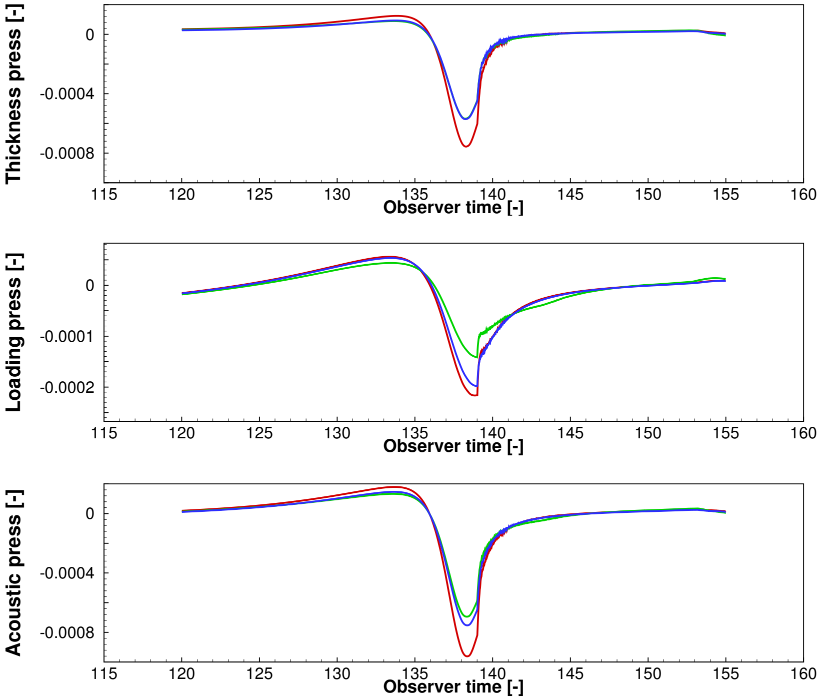

Figure 4.30: Thickness, loading and total acoustic pressures at the observer for the baseline (red), the acoustically optimized (green) and the acoustically constrained torque optimized (blue) flexible rotors.

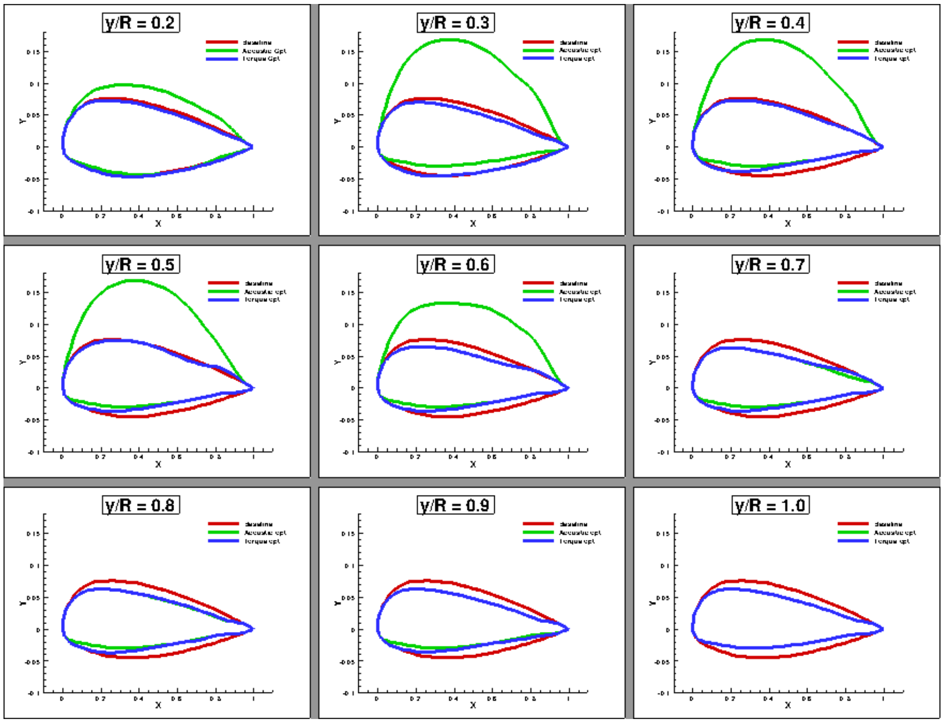

Figure 4.31: Acoustically constrained torque optimized blade shapes

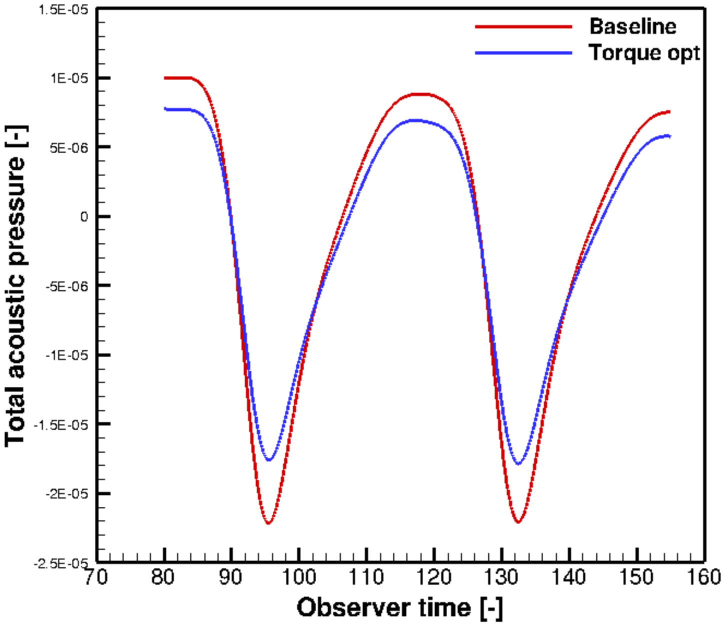

(a) Baseline and optimized total acoustic time history at $\psi = 135$ degrees

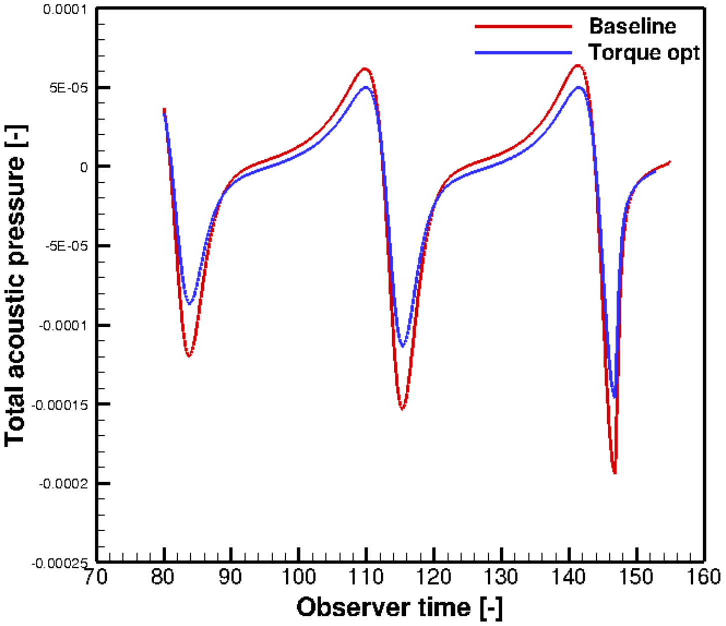

(b) Baseline and optimized total acoustic time history at $\psi = 315$ degrees

Figure 4.32: Directivity study for the baseline and optimized flexible geometries: radial distance $2R$, different azimuthal locations

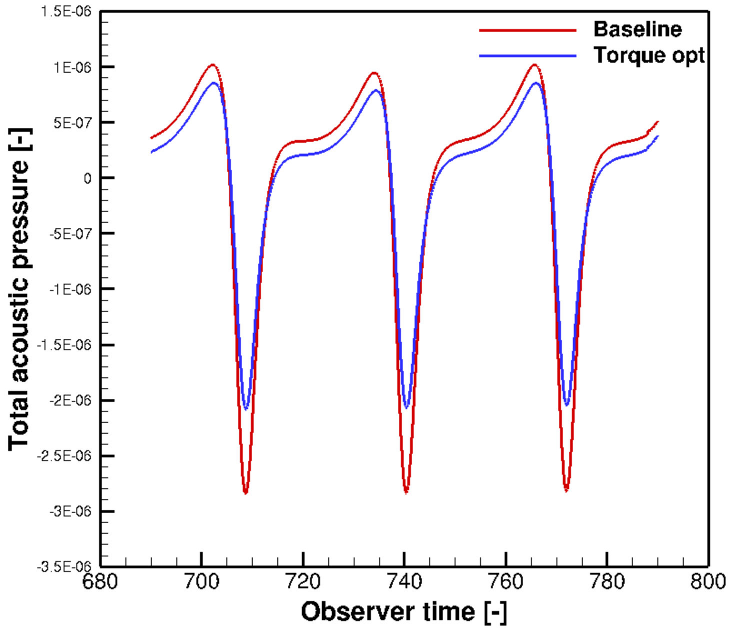

(a) Baseline and optimized total acoustic time history at 50R

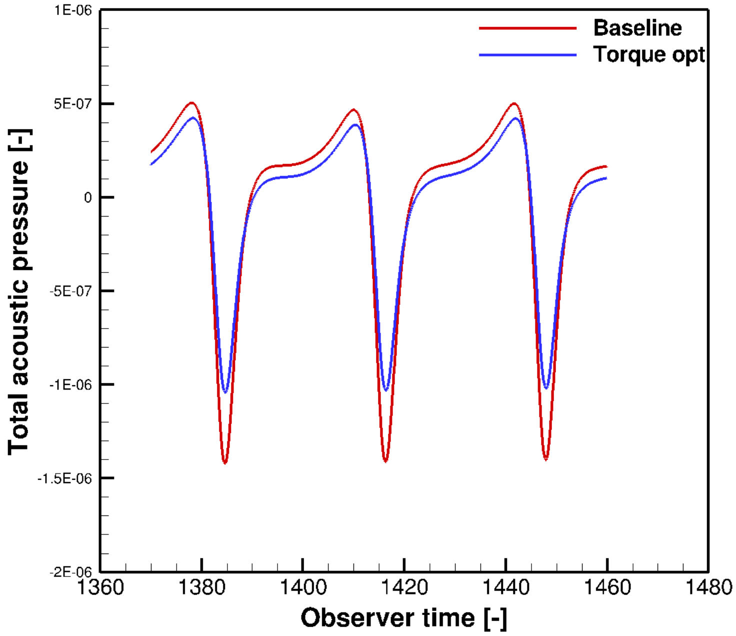

(b) Baseline and optimized total acoustic time history at 100R

Figure 4.33: Directivity study for the baseline and optimized flexible geometries: Azimuth $\psi = 180$ degs, different radial locations

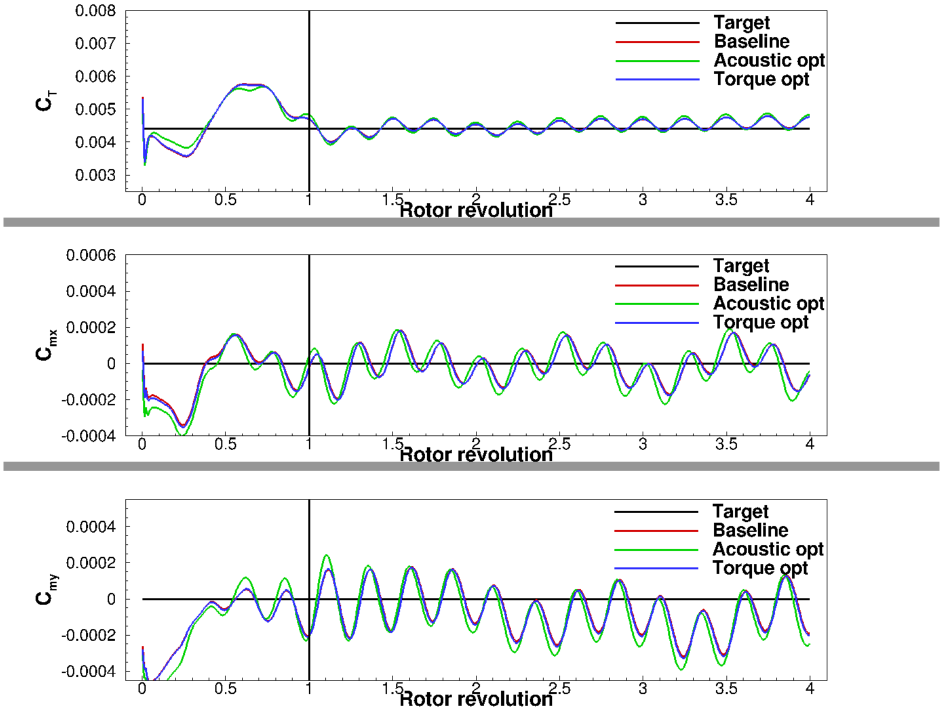

Figure 4.34: Thrust and moments time histories for the baseline, the aeroacoustic optimized and the acoustically constrained torque optimized flexible rotors over 4 rotor revolutions

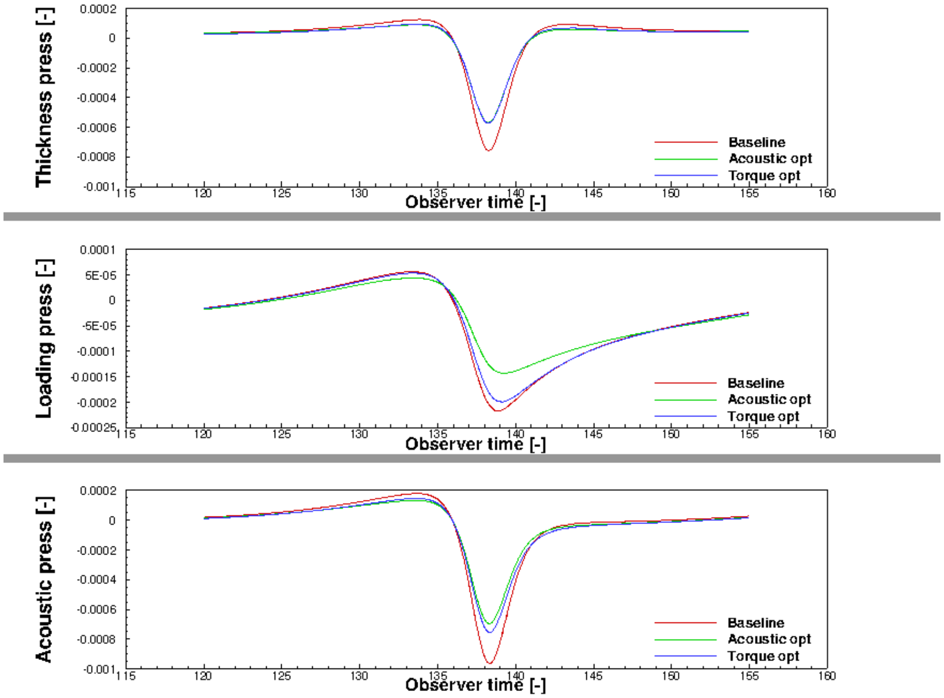

Figure 4.35: Thickness, loading and total acoustic pressures at the observer for the baseline and the two optimized flexible rotors for the multiple revolutions case.

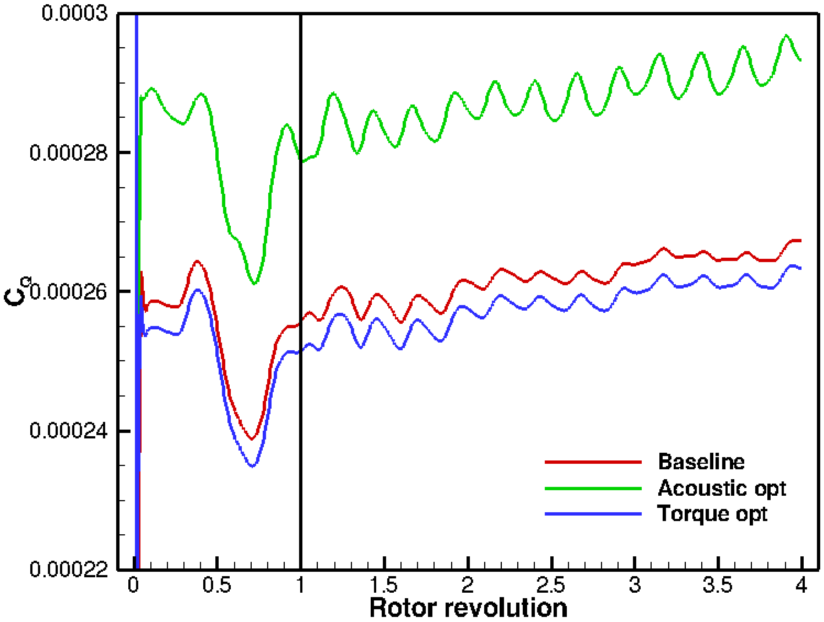

Figure 4.36: Torque time histories for the baseline, the aeroacoustic optimized and the acoustically constrained torque optimized flexible rotors over 4 rotor revolutions

still have been able to improve rotor performance over multiple rotor revolutions. The resulting optimal rotors can be used as intial guesses for more expensive optimizations that target multiple rotor revolutions.

Chapter 5

Conclusions and Future Work

This thesis has presented the development and application of an adjoint-based method for aeroacoustics, with a particular emphasis on rotorcraft design problems. The aeroacoustic adjoint technique has been first developed for two-dimensional applications and it has been applied to the noise minimization of an airfoil in blade-vortex interaction. The two-dimensional formulation has then been extended to include three-dimensional effects. The three-dimensional aeroacoustic adjoint capability has been first applied to the gradient-based noise minimization of a rigid rotor in forward flight. Subsequently, blade flexibility effects have been included in the optimization to realize a unique and unprecedented multidisciplinary adjoint-based optimization capability that encompasses the three disciplines of aerodynamics, structural mechanics and aeroacoustics. By yielding optimal rotors characterized by superior aeroacoustic and aerodynamic performance, these optimizations show that the multidisciplinary adjoint techniques developed in this work can be used to efficiently solve the high-fidelity, large-scale design optimization problems often encountered in rotorcraft design, without the severe design space limitations typical of earlier optimization attempts.

Possible future development for the work presented in this thesis should focus on further advancing the state-of-the-art in both rotorcraft design optimization and adjoint-based optimization techniques. To advance the state-of-the-art in rotorcraft design, future research activities should focus on:

- **Optimization on finer meshes targeting multiple rotor revolutions**: In this thesis no attempt has been made at quantifying the effect of spatial and temporal mesh resolution on the aerodynamic and aeroacoustic performance of the rotor. A systematic investigation of the effect of discretization errors on the predicted performance of the rotor, similar to the grid-convergence studies in [75], will allow to identify the optimal spatial and temporal mesh resolution to be employed in the optimization procedure. Furthermore, in Chapter 4, Section 4.2.2, it has been shown that the forces acting on the rotor have not yet reached a periodic state after two rotor revolutions. To avoid concentrating the optimization efforts on transient flow conditions of little interest to the rotorcraft designer, more rotor revolutions need to be included in the simulation and the optimization objective functionals should be evaluated only after a periodic state has been reached. However, in Chapter 4, Section 4.2.2 it has also been shown that the optimization results presented in this thesis can be used as initial designs for lengthier, more expensive optimizations that target multiple rotor revolutions.

- **Including higher fidelity structural models**: while the Hodges-Dowell beam model employed in this work is in widespread use in the rotorcraft industry, the use of a higher fidelity structural model based on bricks and shell elements will allow for a more accurate description of the geometry and the structural dynamics of the blade. Furthermore, the new structural model will allow to easily update the blade structural properties in response to major changes in the blade shape and to include structural design variables and objectives in the multidisciplinary optimization process.
- **Including nonlinear flow effects in the aeroacoustic prediction**: to allow for the aeroacoustic optimization of rotors characterized by high tip Mach numbers, the quadrupole noise term should be included in the acoustic analogy. The most common approach to account for quadrupole noise in the aeroacoustic prediction is to perform the acoustic integration on an off-body, permeable, integration surface provided that the flowfield between the rotor and the integration surface is sufficiently resolved. Thanks to the choice of the acoustic formulation implemented in this work, the only action required to include quadrupole noise effects in the current optimization framework is the identification of a suitable off-body integration surface.

- **Investigating multiple local minima**: as stated before, gradient-based optimization algorithms seek a saddle point of the Lagrangian function associated with the optimization problem. In the case of a multimodal design space, typical of large-scale problems, gradient-based optimization algorithms can potentially be trapped in a local minimum for the optimization problem. As proposed by Lyu et al. [76], the multimodality of the design space should be investigated by starting the optimization from random initial geometries. If the rotorcraft design space is found to be multimodal, a hybrid optimization strategy that combines the efficiency of gradient based optimization algorithms with the intrinsic global nature of evolutionary methods should be pursued. Previous work [16, 77] in this area has focused on enhancing metamodeling techniques, Kriging or response surface methods, with gradient information computed with the adjoint approach.

- **Investigating multipoint design optimization**: Single point design optimizations such as the ones presented in this work yield optimal geometries for which the performance deteriorate quickly at off design conditions. A more robust approach to rotorcraft design would be to perform a multipoint optimization where different design conditions are targeted simultaneously. In the context of helicopter design it would be natural to target both hover and forward flight to optimize the aerodynamic and the aeroacoustic performance of the vehicle. Furthermore, adopting a higher-fidelity structural model and including structural design variables and objectives in the optimization process could allow the multipoint optimization to also target a maneuver condition realizing a fully automated design optimization process.

Strategies to develop discrete adjoint sensitivities are now fairly well understood and future work on adjoint-based optimizaton should focus on:

- **Evaluating algorithms for the solution of linear systems with multiple right hand sides**: The use of sequential quadratic programming algorithms for the solution of the large-scale design optimization problems treated in this work requires the full sensitivity vector of the objective and the constraint of the optimization problem. The adjoint method presented in this work provides an efficient way of computing sensitivity of one functional with respect to a set of design variables. When multiple functionals are present, the adjoint system needs to be solved multiple times as its right hand side depends on the particular functional being considered, as shown in equation (3.29). Hence, algorithms that allow for the efficient solution of linear systems with multiple right-hand-sides should be considered in the future to improve the performance of the current optimization framework. By accessing the coefficient matrix and performing all the necessary floating point operations only once for all the right hand sides, the solution of linear systems with multiple right hand sides should be well suited for execution on emerging computer architectures. While Jacobi-like iterative schemes can be trivially extended to the simultaneous solution of mulitiple linear systems, the generalization of Krylov-based methods to the multiple right-hand-side case is more involved [78]. Finally, the efficient solution of linear systems with multiple right hand sides could allow for the evaluation of the exact Hessian matrix of the optimization problem, significantly improving the performance of the optimization algorithm employed.

- **Investigating the effect of gradient accuracy on the performance of the optimization algorithms**: since any gradient-based optimization algorithm uses gradient information to identify a local minimum for the objective function, the accuracy of the gradient is expected to significantly affect the performance of the optimization algorithm. Previous studies have investigated the effect that approximations to the adjoint linearization have on the optimization process [79]. The tangent and adjoint linearizations presented in this work are verified to machine precision provided that the nonlinear flow solution is completely converged. For realistic applications converging the nonlinear residuals to zero is unrealistic at best. In a realistic scenario the nonlinear residuals are only partially converged, resulting in inaccurate gradient computations. By slightly modifying the derivation of the adjoint equations presented in this thesis, different strategies can be devised to account for errors resulting from partial convergence of the nonlinear flow problem. These strategies should be thoroughly investigated to understand and address the effect that partial convergence of the flow solution has on the optimization process.

References

[1] W. Johnson, *Rotorcraft Aeromechanics*. Cambridge University Press, 2013.

[2] W. R. Johnson, “Rotorcraft Aerodynamics Models for a Comprehensive Analysis,” in *54th American Helicopter Society Annual Forum and Technology Display, Washington, DC*, May 1998.

[3] A. M. Wissink, J. Sitaraman, V. Sankaran, M. D. J., and P. T. H., “A Multi-Code Python Based Infrastructure for Overset CFD with Adaptive Cartesian Grids,” in *46th AIAA Aerospace Sciences Meeting, Reno, NV*, 2008, AIAA Paper 2008–0927.

[4] M. Costes, T. Renaud, and B. Rodriguez, “Rotorcraft Simulations: a Challenge for CFD,” *International Journal of Computational Fluid Dynamics*, vol. 26, no. 6-8, pp. 383–405, October 2012.

[5] Y. H. Yu, C. Tung, B. van der Wall, H.-J. Pausder, C. Burley, T. Brooks, P. Beaumier, Y. Delrieux, E. Mercker, and K. Pengel, “The HART-II Test: Rotor Wakes and Aeroacoustics with Higher-Harmonic Pitch Control (HHC) Inputs -The Joint German/French/Dutch/US Project-,” in *58th American Helicopter Society Annual Forum, Montreal, Canada*, June 11–13 2002.

[6] B. Edwards and C. Cox, “Revolutionary Concepts for Helicopter Noise Reduction - S.I.L.E.N.T Program,” NASA, Tech. Rep. CR-2002-211650, May 2002.

[7] Y. H. Yu, “Rotor Blade Vortex Interaction Noise,” *Progress in Aerospace Sciences*, vol. 36, pp. 97–115, 2000.

[8] B. W. Sim, R. D. Janakiram, N. L. Barbely, and E. Solis, “Reduced In-Plane, Low Frequency Noise of an Active Flap Rotor,” in *American Helicopter Society 65th Annual Forum*, Grapevine, TX, May 2009.

[9] S. Chae, K. Yee, C. Yang, T. Aoyama, S. Jeong, and S. Obayashi, “Helicopter Rotor Shape Optimization for the Improvement of Aeroacoustic Performance in Hover,” *Journal of Aircraft*, vol. 47, no. 5, pp. 1770–1783, Semptember–October 2010.

[10] B. G. Marinus, M. Roger, V. den Braembussche, and W. Bosschaerts, “Multidisciplinary Optimization of Propeller Blades: Focus on Acoustic Results,” in *47th AIAA/ASME/SAE/ASEE Joint Propulsion Conference and Exhibit*, 2011, AIAA Paper 2011–2801.

[11] J. D. Baeder, "Euler Solutions to Nonlinear Acoustics of Non-Lifting Hovering Rotor Blades," NASA, Tech. Rep. TM-103837, February 1991.

[12] J. Bain, "Computational Comparison Between FW-H and Direct Acoustic Predictions," in *72nd Forum and Technology Display of the American Helicopter Society*, 2016, AHS Paper 2016–185.

[13] F. Farassat and G. P. Succi, "The Prediction of Helicopter Discrete Frequency Noise," *Vertica*, vol. 7-4, pp. 309–320, 1983.

[14] K. S. Brentner and F. Farassat, "Modeling Aerodynamically Generated Sound of Helicopter Rotors," *Progress in aerospace sciences*, vol. 39, pp. 83–120, 2003.

[15] A. J. Keane and B. N. Prasanth, *Computational Approaches for Aerospace Desing*. Wiley, 2005.

[16] A. Forrester, A. Sobester, and A. Keane, *Engineering Design via Surrogate Modelling: A Practical Guide*. Wiley, 2008.

[17] B. R. Jones, C. W. A., and A. S. Lyrintzis, "Aerodynamic and Aeroacoustic Optimization of Rotorcraft Airfoils via a Parallel Genetic Algorithm," *Journal of Aircraft*, vol. 37-6, pp. 1088–1096, 2000.

[18] B. G. Marinus, M. Roger, V. den Braembussche, and W. Bosschaerts, "Multidisciplinary Optimization of Propeller Blades: Focus on Acoustic Results," in *47th AIAA/ASME/SAE/ASEE Joint Propulsion Conference and Exhibit*, 2011, AIAA Paper 2011–2801.

[19] J. C. Vassberg and A. Jameson, "Influence of Shape Parameterization On Aerodynamic Shape Optimization," in *VKI Lecture Series on Aerodynamic Drag Prediction and Reduction, von Karman Institute of Fluid Dynamics, Rhode St Genese, Belgium*, 2014.

[20] J. L. Walsh, G. J. Bingham, and M. F. Riley, "Optimization Method Applied to the Aerodynamic Design of Helicopter Rotor Blades," *Journal of the American Helicopter Society*, vol. 32-4, pp. 39–44, 1987.

[21] J. Zibi, G. Defresen, and M. Costes, "A Numerical Procedure for Aerodynamic Optimization of Helicopter Rotor Blades," in *Proceedings of the 18th European Rotorcraft Forum*, 1992.

[22] N. Jorge and W. S. J., *Numerical Optimization*. Springer, 2006.

[23] A. Jameson and L. Martinelli, "Aerodynamic Shape Optimization Techniques Based on Control Theory," in *Computational Mathematics Driven by Industrial Problems*, ser. Lecture Notes in Mathematics, R. Burkard, A. Jameson, G. Strang, P. Deuflhard, J.-L. Lions, V. Capasso, J. Periaux, and H. Engl, Eds. Springer Berlin Heidelberg, 2000, vol. 1739, pp. 151–221. [Online]. Available: http://dx.doi.org/10.1007/BFb0103920

[24] Z. Lyu, K. W. Kenway, and J. R. R. A. Martins, "Aerodynamic Shape Optimization Investigation of the Common Research Model Wing Benchmark," *AIAA Journal*, vol. 53-4, pp. 968–985, 2015.

[25] E. Nielsen and W. Anderson, "Recent Improvements in Aerodynamic Design Optimization on Unstructured Meshes," *AIAA Journal*, vol. 40, no. 6, pp. 1155–1163, June 2002.

[26] S. Kim, A. J., and A. Jameson, "Multi-Element High-Lift Configuration Design Optimization Using Viscous Continuous Adjoint Method," *Journal of Aircraft*, vol. 41, no. 5, pp. 1082–1097, 2004.

[27] F. Bisson and S. Nadarajah, "Adjoint-Based Aerodynamic Optimization of Benchmark Problems," in *53rd AIAA Aerospace Sciences Meeting, Kissimmee, Fl*, January 2015, AIAA Paper 2015-1948.

[28] C. Lee, K. Telidetzki, H. Buckley, H. Gagnon, and D. W. Zingg, "Aerodynamic Shape Optimization of Benchmark Problems Using Jetstream," in *53rd AIAA Aerospace Sciences Meeting, Kissimmee, Fl*, January 2015, AIAA Paper 2015-0262.

[29] M. Giles, M. Duta, J. Muller, and N. A. Pierce, "Algorithm Developments for Discrete Adjoint Methods," *AIAA Journal*, vol. 41, no. 2, pp. 198–205, February 2003.

[30] A. Jameson and J. Vassberg, "Computational Fluid Dynamics for Aerodynamic Design: Its Current and Future Impact," in *Proceedings of the 39th Aerospace Sciences Meeting and Exhibit, Reno NV*, 2001, AIAA Paper 2001–0538.

[31] A. Jameson, "Aerodynamic Shape Optimization using the Adjoint Method," in *VKI Lecture Series on Aerodynamic Drag Prediction and Reduction, von Karman Institute of Fluid Dynamics, Rhode St Genese, Belgium*, 2003.

[32] D. J. Mavriplis, "Solution of the Unsteady Discrete Adjoint for Three-Dimensional Problems on Dynamically Deforming Unstructured Meshes," in *Proceedings of the 46th Aerospace Sciences Meeting and Exhibit, Reno NV*, 2008, AIAA Paper 2008–0727.

[33] E. Nielsen and B. Diskin, "Discrete Adjoint-Based Design for Unsteady Turbulent Flows on Dynamic Overset Unstructured Grids," in *50th AIAA Aerospace Sciences Meeting and Exhibit, Nashville, TN*, January 9-12 2012, aIAA Paper 2012–0554.

[34] E. Nielsen, B. Diskin, and N. K. Yamaleev, "Discrete Adjoint-Based Design Optimization of Unsteady Turbulent Flows on Dynamic Unstructured Grids," *AIAA Journal*, vol. 48, no. 6, pp. 1195–1206, June 2010.

[35] K. Mani and D. J. Mavriplis, "Unsteady Discrete Adjoint Formulation for Two-Dimensional Flow Problems with Deforming Meshes," *AIAA Journal*, vol. 46, no. 6, pp. 1351–1364, June 2008.

[36] S. W. Lee and O. J. Kwon, "Aerodynamic Shape Optimization of Hovering Rotor Blades in Transonic Flow Using Unstructured Meshes," *AIAA Journal*, vol. 44, no. 8, pp. 1816–1825, August 2006.

[37] J. R. R. A. Martins and A. B. Lambe, "Multidisciplinary Design Optimization: A Survey of Architectures," *AIAA Journal*, vol. 51, pp. 2049–2075, 2013.

[38] A. Mishra, K. Mani, D. J. Mavriplis, and J. Sitaraman, "Helicopter Rotor Design using Adjoint-based Optimization in a Coupled CFD-CSD Framework," in *69th American Helicopter Society Annual Forum, Phoenix, AZ*, May 21–23 2013.

[39] M. Rumpfkeil and D. Zingg, "The Optimal Control of Unsteady Flows With a Discrete Adjoint Method," *Journal of Optimization and Engineering*, vol. 11, no. 1, pp. 5–22, 2010.

[40] T. D. Economon, F. Palacios, and J. J. Alonso, "A Coupled-Adjoint Method for Aerodynamic and Aeroacoustic Optimization," in *14th AIAA/ISSM Multidisciplinary Analysis and Optimization Conference*, 2012, AIAA Paper 2012–5598.

[41] D. J. Mavriplis, "Unstructured-Mesh Discretizations and Solvers for Computational Aerodynamics," *AIAA Journal*, vol. 46-6, pp. 1281–1298, June 2008.

[42] A. Jameson, "Time Dependent Calculations Using Multigrid, with Applications to Unsteady Flows Past Airfoils and Wings," in *Proceedings of the 10th Computational Aerodynamics Conference, Honolulu HI*, 1991, AIAA Paper 1991–1596.

[43] Y. Saad, *Iterative Methods for Sparse Linear Systems*. SIAM, 2003, 2nd edition.

[44] B. M. Kulfan, "Universal Parametric Geometry Representation Method," *Journal of Aircraft*, vol. 45-1, pp. 142–158, 2008.

[45] H. C. Yee, N. D. Sandham, and M. J. Djomehri, "Low-Dissipative High-Order Shock-Capturing Methods Using Characteristic-Based Filters," *Journal of Computational Physics*, vol. 150, pp. 199–238, 1999.

[46] J. E. Ffowcs Williams and D. L. Hawkings, "Sound Generation by Turbulence and Surfaces in Arbitrary Motion," *Philosophical Transactions of the Royal Society of London. Series A, Mathematical and Physical Sciences*, vol. 264-1151, pp. 321–342, May 1969.

[47] P. di Francescantonio, "A New Boundary Integral Formulation for the Prediction of Sound Radiation," *Vertica*, vol. 7-4, pp. 309–320, 1983.

[48] D. P. Lockard, "An Efficient Two-Dimensional Implementation of the Ffowcs Williams and Hawkings Equation," *Journal of Sound and Vibration*, vol. 224-4, pp. 897–911, 2000.

[49] W. H. Press, S. A. Teukolsky, W. T. Vetterling, and B. P. Flannery, *Numerical Recipes in FORTRAN*. Cambridge University Press, 1992.

[50] D. G. Crighton, A. P. Dowling, and J. E. Ffowcs Willliams, *Modern Methods in Analytical Acoustics*. Springer-Verlag, 1992.

[51] M. Rumpfkeil, "Airfoil Optimization for Unsteady Flows With Application to High-Lift Noise Reduction," Ph.D. dissertation, University of Toronto, 2008.

[52] J. N. Lyness and C. B. Moler, "Numerical Differentiation of Analytic Function," *SIAM Journal of Numerical Analysis*, vol. 4-2, pp. 202–210, 1967.

[53] J. R. R. A. S. P. Martins and J. J. Alonso, "The Complex-Step Derivative Approximation," *ACM Transactions on Mathematical Software*, vol. 29-3, pp. 245–262, 2003.

[54] D. J. Mavriplis, "Discrete Adjoint-Based Approach for Optimization Problems on Three-Dimensional Unstructured Meshes," *AIAA Journal*, vol. 45-4, pp. 741–750, April 2007.

[55] D. J. Mavriplis and K. Mani, "Unstructured Mesh Solution Technique Using the NSU3D Solver," in *Proceedings of the 52nd AIAA Aerospace Sciences Conference, National Harbor, MD*, 2014, AIAA Paper 2014–0081.

[56] K. Mani and D. J. Mavriplis, "Geometry Optimization in Three-Dimensional Unsteady Flow Problems using the Discrete Adjoint," in *51st AIAA Aerospace Sciences Meeting, Grapevine, TX*, January 2013, AIAA Paper 2013-0662.

[57] P. R. Spalart and S. R. Allmaras, "A One-equation Turbulence Model for Aerodynamic Flows," *La Recherche Aérospatiale*, vol. 1, pp. 5–21, 1994.

[58] D. J. Mavriplis, "Multigrid Strategies for Viscous Flow Solvers on Anisotropic Unstructured Meshes," *Journal of Computational Physics*, vol. 145, no. 1, pp. 141–165, Sep. 1998.

[59] D. H. Hodges and E. H. Dowell, "Nonlinear Equations Of Motion For The Elastic Bending And Torsion of Twisted Nonuniform Rotor Blades," NASA, Tech. Rep. TN-D-7818, December 1974.

[60] D. J. Mavriplis, Z. Yang, and M. Long, "Results using NSU3D for the first Aeroelastic Prediction Workshop," in *Proceedings of the 51st Aerospace Sciences Meeting and Exhibit, Grapevine TX*, 2013, AIAA Paper 2013–0786.

[61] D. M. Schuster, P. Chwalowski, J. Heeg, and C. D. Wieseman, "Summary of Data and Findings from the First Aeroelastic Prediction Workshop," in *Seventh International Conference on Computational Fluid Dynamics (ICCFD7).* Big Island, HI: ICCFD, July 9-13 2012.

[62] A. Mishra, K. Mani, D. J. Mavriplis, and J. Sitaraman, "Time-dependent Adjoint-based Aerodynamic Shape Optimization Applied to Helicopter Rotors," *Journal of Computational Physics*, vol. 292, no. 1, pp. 253–271, 2015, doi:10.1016/j.jcp.2015.03.010.

[63] I. Chopra and G. Bir, "University of Maryland Advanced Rotor Code: UMARC," in *American Helicopter Society Aeromechanics Specialists Conference*, San Franscisco, CA, January 1994.

[64] Heckmann, M. A. Otter, S. Dietz, and J. D. Lopez, "The DLR FlexibleBodies Library to Model Large Motions of Beams and of Flexible Bodies Exported from Finite Element Programs," in *Modelica*, September 4–5 2006.

[65] A. A. Kumar, S. R. Vishwamurthy, and R. Ganguli, "Correlation of Helicopter Rotor Aeroelastic Response with HART-II Wind Tunnel Test Data," *Aircraft Engineering and Aerospace Technology: An International Journal*, vol. 82, no. 4, pp. 237–248, 2010.

[66] Z. Yang and D. J. Mavriplis, “A Mesh Deformation Strategy Optimized by the Adjoint Method on Unstructured Meshes,” *AIAA Journal*, vol. 45, no. 12, pp. 2885–2896, 2007.

[67] K. S. Brentner and F. Farassat, “An Analytical Comparison of The Acoustic Analogy And Kirchoff Formulation For Moving Surfaces,” *AIAA Journal*, vol. 36-8, pp. 1379–1386, 1998.

[68] G. A. Bres, K. S. Brentner, G. Perez, and H. E. Jones, “Maneuvering Rotorcraft Noise Prediciton,” *Journal of sound and vibration*, vol. 275, pp. 719–738, 2004.

[69] M. H. Dunn and F. Farassat, “High-Speed Propeller Noise Prediction - A Multidisciplinary Approach,” *AIAA Journal*, vol. 30-7, pp. 1716–1723, 1992.

[70] C. Zhu, R. H. Byrd, P. Lu, and J. Nocedal, “L-BFGS-B - FORTRAN Subroutines for Large-scale Bound Constrained Optimization,” Department of Electrical Engineering and Computer Science, Tech. Rep., December 31 1994.

[71] “http://www.scipy.org/.”

[72] P. E. Gill, W. Murray, and M. A. Saunders, “SNOPT: An SQP Algorithm for Large-Scale Constrained Optimization,” *SIAM review*, vol. 47-1, pp. 99–131, 2005.

[73] R. Hicks and P. Henne, “Wing Design by Numerical Optimization,” *Journal of Aircraft*, vol. 15-7, pp. 407–412, 1978.

[74] F. H. Schmitz and Y. H. Yu, “Helicopter Impulsive Noise: Theoretical and Experimental Status,” NASA, Tech. Rep. TM-84390, November 1983.

[75] E. N. Tinoco, O. P. Brodersen, S. Keye, K. R. Laflin, E. Feltrop, J. C. Vassberg, M. Mani, B. Rider, R. A. Wahls, J. H. Morrison, D. Hue, M. Gariepy, C. J. Roy, D. J. Mavriplis, and M. Murayama, “Summary of Data from the Sixth AIAA CFD Drag Prediction Workshop: CRM Cases 2 and 5,” in *55th AIAA Aerospace Sciences Meeting*, January 2017, AIAA Paper 2017–1208.

[76] Z. Lyu, G. K. W. Kenway, and J. R. R. A. Martins, “RANS-based Aerodynamic Shape Optimization Investigations of the Common Research Model Wing,” in *52nd Aerospace Sciences Meeting*, January 13–17 2014, AIAA Paper 2014–0567.

[77] W. Yamazaki and D. J. Mavriplis, “Design Optimization Utilizing Gradient/Hessian Enhanced Surrogate Model,” in *40th Fluid Dynamic Conference and Exhibit*, June 2010, AIAA Paper 2010–4363.

[78] K. G. Prasad, D. E. Keyes, and J. H. Kane, “GMRES for sequentially multiple nearby systems,” Tech. Rep., 1995.

[79] R. P. Dwight and J. Brezillon, “Effect of Various Approximations of the Discrete Adjoint on Gradient-Based Optimization,” in *44th Aerospace Sciences Meeting*, January 9–12 2006, AIAA Paper 2006–0690.